



DEGREE PROJECT IN MECHANICAL ENGINEERING,
SECOND CYCLE, 30 CREDITS
STOCKHOLM, SWEDEN 2016

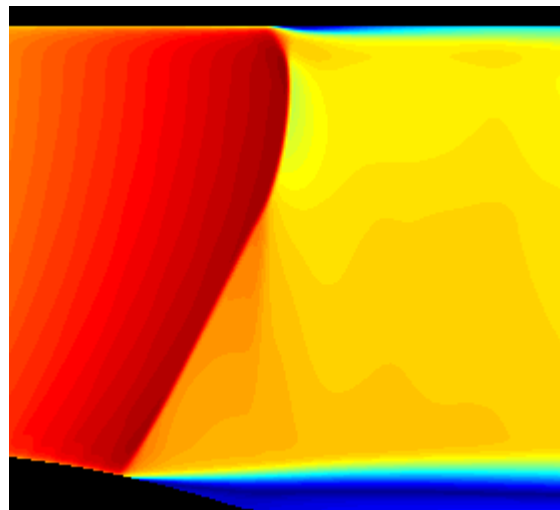
ON SIMULATING COMPRESSIBLE FLOWS WITH A DENSITY BASED SOLVER

SATHYANARAYANAN CHANDRAMOULI

KTH ROYAL INSTITUTE OF TECHNOLOGY
SCHOOL OF ENGINEERING SCIENCES

ON SIMULATING COMPRESSIBLE FLOWS WITH A DENSITY BASED SOLVER

SATHYANARAYANAN CHANDRAMOULI



Master of Science Thesis, September 2016
KTH DEPARTMENT OF MECHANICS
FLUID MECHANICS
SE-100 44 STOCKHOLM



Examensarbete September 2016

On simulating compressible flows with a density based solver

SATHYANARAYANAN CHANDRAMOULI

Godkänt 2016-09-05	Examinator Mihai Mihaescu	Handledare Romain Gojon
	Uppdragsgivare	Kontaktperson

Sammanfattning

En kopplad densitets baserad losare I foam-extend används för att simulera transoniska flöden. Lösaren grundar sig på en explicit och tids-specifik algoritm och är kopplad till ett kompressibelt URANS (Unsteady Reynolds-Averaged Navier-Stokes) och en LES (Large Eddy Simulation) modul. Lösaren är validerad i kanoniska, kompressibla flödes fall så som 1-D stötvågsrör och transoniska flöden genom en 2-D kanal. Sedan görs en 2-D URANS simulering av flödet inom passagen av ett HPT-NGV (High Pressure Turbine Nozzle Guide Vane) och jämförs mot experimentell data. Till sist presenteras resultatet av en 3-D LES utförd på en förenklad geometri av HPT-NGV. Till framtiden kommer denna numeriska uppställning att användas för att studera indirekta förbränningars ljud i flygplans motorer.

NYCKELORD: Kopplad densitets baserad losare, High Pressure Turbine Nozzle Guide Vane, Large Eddy Simulations, Unsteady Reynolds Averaged Navier-Stokes, transonisk flöde, indirekta förbränningars ljud



KTH DEPARTMENT OF
MECHANICS

Master of Science Thesis September 2016

Numerical characterization of compressible flow

SATHYANARAYANAN CHANDRAMOULI

Approved 2016-09-05	Examiner Mihai Mihaescu	Supervisor Romain Gojon
	Commissioner	Contact person

Abstract

A coupled density based solver in the framework of *foam-extend* is used to perform simulations of transonic flows. The solver is based on an explicit and time-accurate algorithm and is coupled to a compressible Unsteady Reynolds-Averaged Navier-Stokes (URANS) and a Large Eddy Simulation (LES) module. The solver is first attested on canonical compressible flow scenarios such as a 1-D shock tube and the transonic flow through a 2-D channel. Following this, a 2-D URANS simulation of the flow within the passages of a High Pressure Turbine Nozzle Guide Vane (HPT-NGV) is performed and compared against experimental data. Finally, preliminary results of a 3-D LES on a simplified geometry of the HPT-NGV are presented. In the future, this numerical setup will be used to study indirect combustion noise in aircraft engines.

KEYWORDS: Coupled density based solver, High Pressure Turbine Nozzle Guide Vane, combustion noise, Large Eddy Simulations, Unsteady Reynolds Averaged Navier-Stokes, transonic flow, indirect combustion noise

FOREWORD

There are a number of people who I feel particularly grateful for their support and encouragement in my scientific endeavours. I would start with expressing sincere thanks to supervisor Dr.Romain Gojon and examiner Dr.Mihai Mihaescu for their enduring support, both scientific and technical during the course of the Master thesis.

I would like to thank Dr.Jens Fridh for sharing proprietary data conducted at KTH Department of Industrial technology and management. Besides, I would like to thank him for his scientific advise.

I would like to express my gratitude to all my colleagues at the department for the scientific discussions and leisure. I am especially grateful to my colleagues Asuka Gabriele for performing the CAD work for generating the linear cascade of nozzle guide vanes and Varuna Dharmadasa for helping with the swedish translation of the abstract.

I would like to thank PDC, KTH and KTH Mechanics for allowing me to use the systems for running the simulations. I am especially grateful to Jing Gong, PDC, for his prompt replies to querries on running simulations on Beskow.

I would like to express my gratitude to Professor Henrik Alfredsson, who has been responsible for inspiring my passion in fluid mechanics. Last, but not least, I express thanks to my family for their support during all my years.

Sathyaranarayanan

Stockholm, September 2016

DECLARATION

The author would like to thank master student and colleague Asuka Gabriele Pietroniro for performing the CAD work leading to the generation of the linear cascade of nozzle guide vanes from the annular sector cascade provided.

The rest of the work including the following were carried out by the author, with inputs and guidance from supervisors Dr. Romain Gojon and Dr. Mihai Mihaescu. Inputs were received from Dr. Jens Fridh for setting up the NGV case. Jing Gong from PDC shared expertise on running parallel simulations on Beskow.

- Solver installation and setup on KTH Mechanics systems and on Beskow
- Domain and mesh generation for the ONERA S8 channel
- Domain and mesh generation for the linear cascade of nozzle guide vanes
- Simulation setup for all the cases
- Post-processing and analysis of the obtained results
- Methodology for future investigations of combustion noise

TABLE OF CONTENTS

SAMMANFATTNING (SWEDISH)	4
ABSTRACT	6
FOREWORD	7
DECLARATION	8
TABLE OF CONTENTS	9
1 INTRODUCTION	11
1.1 Simulation of compressible flows	11
1.2 Coupled density based solvers	12
1.3 Open source software foam-extend	12
1.4 Selection of test cases	13
1.5 Objectives of the thesis	13
2 THEORY AND METHODOLOGY	14
2.1 Governing equations	14
2.2 The Shock tube	15
2.3 ONERA S8 Transonic channel	19
2.4 Linear cascade of nozzle guide vanes (NGV)	25
3 SIMULATION OF TURBULENCE AND NUMERICAL SETUP	39
3.1 Turbulence	39
3.2 A review of approaches used to simulate turbulent flow	41
3.3 Compressible Unsteady Reynolds averaged Navier-Stokes (URANS) simulations	41

3.4	The solver	44
3.5	The finite volume method in OpenFOAM	45
3.6	Features of <i>dbnsTurbFoam</i>	46
3.7	Code architecture and flow chart	48
3.8	Equation representation in <i>foam-extend-3.2</i>	49
3.9	Spatial Discretization	49
3.10	Temporal Discretization	52
4	RESULTS & DISCUSSIONS	53
4.1	Sod's shock tube	53
4.2	ONERA S8 Transonic channel	55
4.3	Linear cascade of Nozzle Guide Vanes	63
5	CONCLUSIONS, RECOMMENDATIONS AND FUTURE WORK	71
5.1	Conclusions	71
5.2	ONERA S8 channel	71
5.3	Compressible LES module in <i>foam-extend</i>	72
5.4	LES results obtained for the HPT-NGV case	73
5.5	Aeroacoustic simulations to characterize indirect combustion noise	73
6	REFERENCES	75
	APPENDICES:	78
A	Governing equation representation in <i>foam-extend</i>	78
B	Instructions for installing <i>foam-extend</i>	79

CHAPTER 1

INTRODUCTION

1.1. Simulation of compressible flows

Compressible flow phenomena are encountered in applications with significant density variations in the flow field. Among others, compressible flow effects are of importance in the following areas:

- Aeronautics: The high speed flow field around large aircraft and the flows within turbo-machinery blade passages.
- Combustion: Combustion processes in vehicles (aircraft and automotive engines)



Figure 1.1. Droplet condensation around a supersonic aircraft near the sound barrier due to supersonic expansion at the trailing surfaces
Source: www.ibntimes.co.uk

Given their occurrence, the recreation of compressible flow phenomena are important for design and control processes of the load bearing components of the aircraft, in controlling combustion processes in aircraft engines to within permissible limits and for vehicle noise control and reduction. Experimental studies of compressible flow phenomena are expensive, and therefore pushed to the final stages of the design process. Alternate approaches to investigate compressible flow phenomena involve analytical formulations and numerical simulations. Closed form analytical expressions describing compressible flow phenomena exist for a few specialized cases. In order to investigate these phenomena from a more general framework, numerical approaches are adopted for simulation on a discretized domain. With the advent of high fidelity Computational Fluid Dynamics (CFD) codes, numerical simulations are gaining importance in the early stages of the product design and development.

1.2. Coupled density based solvers

Despite their relative advantages over other methods in investigations, simulation of high speed compressible flow presents several challenges:

- **Shock capturing:** Anderson (2004) has demarcated different flow regimes based on the relative dominance of compressibility effects. Notably, at mach numbers greater than 0.8, large flow gradients begin to manifest in the flow field, due to the presence of shock waves. A shock wave is a disturbance propagating in a fluid at speeds greater than the local speed of sound. Due to their large propagation speeds, it can be argued that the flow properties across a shock change discontinuously. This presents problems in their numerical representation, due to the occurrence of spurious Gibb's oscillations [2].
- **Wave propagation in different directions:** Compressible flow phenomena are dominated by non-linear wave propagation in different directions, which are difficult to capture numerically. It is reported that several schemes for advective flux discretization often require certain fixes in order to represent all the wave motions in the flow domain.
- **Complex flow field interactions:** Transition to turbulence is implicit at the large Reynolds numbers that are characteristic of compressible flow. Complex flow field interactions between the prevailing turbulence and shocks in the flow vastly alter the nature of the flow.

In this context, coupled density based solvers represent the cutting edge in capturing high speed compressible flow phenomena. Coupled density based solvers respect the strong interdependence of flow variables. This is done by updating these variables simultaneously at each time iteration. Therefore, this results in a robust and accurate solution as compared to methods that solve the governing equations in a segregated manner. This provided the motivation for the selection of a coupled density based solver for the problems of interest of the thesis.

1.3. Open source software *foam-extend*

In order to simulate the flow scenarios of interest, the open source software *foam-extend* was selected. *foam-extend* is an extension of the OpenFOAM project with the aim to include community contributed extensions in OpenFOAM [<http://www.extend-project.de/>]. The solver has incorporated several additional solvers and utilities over the standard OpenFOAM software. The main advantage of OpenFOAM is that new solvers and utilities can be created with some pre-requisite knowledge of the underlying method, physics and the programming techniques involved. OpenFOAM is an abbreviation for “Open Source Field Operation and Manipulation”. “Field” in the abbreviation refers to generic tensor fields, and therefore, OpenFOAM provides a convenient platform for the creation and operation of tensor fields.

The problem of interest for the thesis is to simulate high speed compressible flows requiring the resolution of shocks and other critical compressibility effects. Bearing in mind the inherent advantages of a coupled density based solver, the recently developed coupled density based solvers *dbnsFoam* and *dbnsTurbFoam* (Jasak et al., 2014) were chosen to simulate the flow field of interest. *dbnsFoam* is an inviscid flow solver, while *dbnsTurbFoam* is a viscous flow solver. There is a possibility to couple various 2-equation eddy viscosity models and a compressible LES module to *dbnsTurbFoam*.

1.4. Selection of test cases

Upon selection of the solver, it was important to validate it against canonical compressible flow scenarios. The validated solver would then be used to perform aeroacoustic simulations to characterize indirect combustion noise occurring in aircraft engines. Keeping in mind the final aim, the following test cases were chosen:

- **1-D Shock tube:** High speed compressible flows entail the presence of shocks and other non-linear wave propagation in different directions. The 1-D shock tube is a representative, simple test for which an analytical solution exists. It was therefore chosen to attest the solver against capturing the mentioned flow features.
- **2-D ONERA S8 channel:** In order to capture the complex interaction processes in turbulent, high speed compressible flows the 2-D ONERA S8 channel was chosen. Experiments were conducted by Déler et al. (1978) to investigate the shock wave-turbulent boundary layer interactions observed. Shock wave boundary layer interactions are a dynamic 2-way process involving an impinging shock wave interacting with a turbulent boundary layer developing on a solid surface [30]. Abbreviated as SBLI, these interaction processes occur over a wide range of transonic, supersonic & hypersonic flow applications. Examples include internal flows such as flows within turbo-machinery cascades, scramjet intakes and supersonic nozzles and external flows over wings of aircraft in transonic flight and over launch vehicles. Shock wave boundary layer interactions are triggered either by an external impinging shock wave on a boundary layer, or when a supersonic flow faced with a sharp flow restriction leads to the formation of a shock wave originating within the boundary layer. The two kinds of interactions are labeled as type-A and type-B interactions, for the sake of convenience. Type-B interactions are prevalent in transonic flows within turbo-machinery passages, and hence are the focus of the work. High viscous dissipation and flow unsteadiness are inevitable as a result of these interactions, thus negatively affecting the aerodynamic efficiency and resulting in dynamic structural instabilities [30].
- **High pressure turbine Nozzle guide vane (HPT-NGV) cascade:** 2-D simulations to capture the high speed compressible flow and associated flow unsteadiness in the domain. The results obtained from simulations would then be compared with experimental data acquired for an annular sector cascade. The test case is particularly relevant for attesting the solver against realistic turbo-machinery flow scenarios.

1.5. Objectives of the thesis

The objectives of the thesis are:

- To acquire a suitable open source density based solver, easily customizable to user needs. Upon acquiring the tool, it is required to attest it on standard compressible flow scenarios described in Section 1.4.
- Demonstrate the suitability of the solver to simulate the high speed flow within turbo-machinery passages.
- Demonstrate the suitability of the solver towards performing aeroacoustics simulations to characterize combustion noise occurring in aircraft engines.

2 THEORY AND METHODOLOGY

2.1 Governing equations of compressible fluid dynamics

Compressibility of a fluid is defined as the relative volume change of a fluid element in response to an imposed pressure force. In other words, a compressible flow would involve significant density variations and gradients upon an imposed pressure force. In order to understand the relative importance of compressibility in fluid flows, it is useful to divide the fluid flow regimes in terms of the Mach number. The Mach number M is defined as the ratio of the local flow velocity U to the local speed of sound, c .

$$M = \frac{U}{c} \quad (2.1)$$

The isentropic flow relation relating the ratio of local static density ρ to the local stagnation density ρ_0 with the Mach number thus written:

$$\frac{\rho}{\rho_0} = (1 + \frac{\gamma - 1}{2} M^2)^{\frac{-1}{\gamma - 1}} \quad (2.2)$$

γ in the Equation (2.2) is the ratio of the specific heat of the gas at constant pressure c_p to its specific heat at constant volume c_v . It can be shown that for Mach numbers below 0.3, this ratio is about 5 % [1]. Thus, for an initial estimate of fluid flow quantities density variations can be ignored in this regime. Density variations in fluid flow are more pronounced at higher Mach numbers, between 0.3 and 0.8. Here, effects of compressibility can no longer be ignored.

The fluid flow problems of the thesis correspond to mach numbers in excess of 0.8, with the occurrence of locally supersonic flows and the appearance of flow phenomena known as shock waves. The presence of shock waves is felt as a discontinuous change of flow quantities such as density, and the effects of compressibility must be taken into account to describe the flow quantities.

In this context, the 3-D compressible Navier-Stokes (N-S) equations are introduced in the conservative, differential form. They govern the conservation of mass, momentum and energy of a compressible fluid flow. The equations are presented in the tensor notation, following Einstein's convention. The various quantities used in the equations are U , which represents any cartesian component of the local fluid velocity, ρ represents the local fluid density, σ represents the local viscous stress tensor, F represents a component of the body force experienced by a fluid element, p represents the pressure force experienced by a fluid element, q represents a cartesian component of the heat flux vector, and E represents the total specific energy (internal energy+kinetic energy) of the fluid element.

$$\left\{ \begin{array}{l} \frac{\partial \rho}{\partial t} + \frac{\partial (\rho U_i)}{\partial x_i} = 0 \\ \frac{\partial (\rho U_i)}{\partial t} + \frac{\partial (\rho U_i U_j)}{\partial x_i} = \frac{\partial p}{\partial x_i} + \frac{\partial \sigma_{ij}}{\partial x_j} + F_i \\ \frac{\partial (\rho E)}{\partial t} + \frac{\partial (\rho U_i U_j)}{\partial x_j} = -\frac{\partial p U_j}{\partial x_j} + \frac{\partial (\sigma_{ij} U_j)}{\partial x_j} + \partial \frac{q_i}{\partial x_j} + F_i U_i \end{array} \right. \quad (2.3)$$

In order to close the set of 5 partial differential equations, 3 common assumptions about the thermodynamic and kinetic nature of the gas are used, corresponding to the ideal gas assumption, the calorically perfect gas assumption and the Newtonian fluid assumption respectively. The first two assumptions are represented by Equation (2.4).

$$\begin{cases} p = \rho R T \\ h = c_p T \end{cases} \quad (2.4)$$

where, R is the gas constant of air, h is the specific enthalpy of air and c_p is the specific heat of air at constant pressure.

The Newtonian fluid assumption describes a linear relationship between the viscous shear stresses and shear strain rates/local fluid velocity gradients. The tensorial relationship following the Einstein's convention is presented in Equation 2.8. The newtonian assumption is a reasonable model for air.

$$\sigma_{ij} = \mu (2S_{ij} - \frac{2}{3} S_{kk} \delta_{ij}) \quad (2.5)$$

Where, the quantity μ represents the dynamic viscosity of air, S_{ij} represents the strain rate tensor of the fluid at a point and δ_{ij} represents the Kronecker delta function.

Besides, compressible flows involve large variations in temperature, and therefore the empirical Sutherland's viscosity model is used to take into account the variations of dynamic viscosity with temperature. The model is widely used in several compressible flow CFD solvers. The constants and reference values, part of the model, are presented in Equation (2.6).

$$\begin{cases} \mu = \mu_{ref} \frac{T_{ref} + T_{sutherland}}{T + T_{sutherland}} \left(\frac{T}{T_{ref}} \right)^{\frac{3}{2}} \\ \mu_{ref} = 1.716 \cdot 10^{-5} \text{ kg m}^{-1} \text{s}^{-1} \\ T_{ref} = 273.15 \text{ K} \\ T_{sutherland} = 110.4 \text{ K} \end{cases} \quad (2.6)$$

Lastly, the modeling of the heat flux term is to be discussed. The heat flux is calculated by considering the Fourier's law, expressed in Equation (2.7).

$$q_j = -\alpha \frac{\partial T}{\partial x_j} = -c_p \frac{\mu}{Pr} \frac{\partial T}{\partial x_j} \quad (2.7)$$

In Equation (2.7), α is the thermal conductivity of the fluid and Pr is the Prandtl number defined for laminar flows.

The present work aims at simulating the high speed compressible flows within turbo-machinery passages based on a numerical solution to the system of governing N-S equations. A step by step approach, moving from a 1-D test case to the problem of interest is adopted. The section 2.2 discusses the numerical simulation of the flow within the Sod's shock tube, before proceeding to the problems of interest of the thesis.

2.2 The Shock tube

2.2.1 Theory

The shock tube is an instrument that generates and directs shock waves at a model under study. A shock wave is a propagating wave in a fluid medium, traveling faster than the local speed of sound in the fluid. Shock waves are characterized by discontinuous changes in fluid properties

like pressure, density, temperature and velocity across their stream-wise extent. As stated in section 2.1, shock waves are frequently encountered in flows where the mach numbers exceed 0.8. In order to study their effects experimentally, a shock tube can be used. In construction, a shock tube is a tube closed at both ends, and consists of a diaphragm separating a gas of high pressure and high density, from a gas at lower pressure and lower density. The high pressure gas is called the driver gas and the low pressure gas is called the driven gas. Upon the sudden removal of the diaphragm, unsteady wave motion is set-up within the shock tube, in order to equalize the pressures in the two sections. A family of compression waves coalesce into a shock wave and travel towards the driven gas increasing its pressure. Correspondingly, a family of rarefaction waves traveling towards the driver section appear, reducing the pressure of the driver gas. Meanwhile, the driver and driven gases are separated by a surface called the contact discontinuity. Across the surface, while the pressure and velocity remain constant, the density changes discontinuously. The unsteady wave motion that is setup takes a while to equalize the pressure across the shock tube, developing into multiple reflections of the traveling waves across the closed ends of the shock tube.

The present study computationally simulates the traveling waves before they reach the ends of the shock tube. The computational results are then compared with the analytical results elaborated in [1].

The analytical considerations are divided into 2 subsections, namely, *Analysis for the shock wave and the contact discontinuity* and *Analysis for the family for spreading rarefaction waves*. The first sub-section characterizes the pressure, temperature, particle velocity and density across the shock wave and the contact discontinuity. The second sub-section characterizes the pressure, temperature, particle velocity and density across the family of rarefaction waves. The Figure 2.1 illustrates the distinct stations in the shock tube to be used in the next sub-section

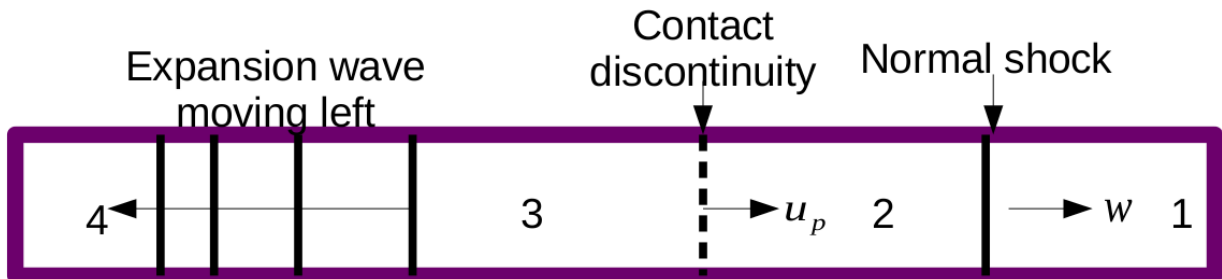


Figure 2.1 Stations in a shock tube after the diaphragm is removed

2.2.2 Analysis of the shock wave and the contact discontinuity

The characterization of the shock wave and contact discontinuity speeds, along with the fluid states before and after the surfaces are discussed. The continuity, momentum and energy conservation equations are written in a frame of reference attached to the moving normal shock. Across the moving normal shock, the conservation equations yield,

$$\begin{cases} \rho_1 w = \rho_2 (w - u_p) \\ p_1 + \rho_1 w^2 = p_2 + \rho_2 (w - u_p)^2 \\ h_1 + \frac{w^2}{2} = h_2 + \frac{(w - u_p)^2}{2} \end{cases} \quad (2.8)$$

In Equation 2.8, the speed of the shock wave is represented as w and the fluid particle speed, and therefore the speed of the contact discontinuity as u_p . The subscripts for the fluid properties in the Equation 2.8 indicate the values of the fluid properties at the various stations depicted in Figure 2.1.

For the case of a calorically perfect gas, the Equation 2.8 yield the following relations (2.17)-(2.20) required to calculate the required flow variables across the normal shock wave.

$$\frac{T_2}{T_1} = \frac{p_2}{p_1} \frac{\frac{\gamma+1}{\gamma-1} + \frac{p_2}{p_1}}{1 + \frac{\gamma+1}{\gamma-1} \frac{p_2}{p_1}} \quad (2.9)$$

$$\frac{\rho_2}{\rho_1} = \frac{1 + \frac{\gamma+1}{\gamma-1} \frac{p_2}{p_1}}{\frac{\gamma+1}{\gamma-1} + \frac{p_2}{p_1}} \quad (2.10)$$

Assuming a calorically perfect gas, we have the shock speed given by Equation (2.11).

$$\left\{ \begin{array}{l} M_{sh} = \frac{w}{c_1} \\ \frac{p_2}{p_1} = \frac{\rho_2 T_2}{\rho_1 T_1} = 1 + \frac{2\gamma}{\gamma-1} (M_{sh}^2 - 1) \\ w = c_1 \sqrt{\frac{\gamma+1}{2\gamma} \left(\frac{p_2}{p_1} - 1 \right) + 1} \end{array} \right. \quad (2.11)$$

In order to obtain the speed of the contact discontinuity, the Equation (2.12) is used, derived from the continuity equation of Equation (2.8).

$$u_p = \left(\frac{\rho_1}{\rho_2} - 1 \right) w \quad (2.12)$$

2.2.3 Analysis of the family of spreading rarefaction waves

An analysis for the unsteady rarefaction wave motion in a shock tube requires an understanding of the propagation of non-linear waves. In contrast to linear waves, non-linear wave propagation causes large pressure and density perturbations from the ambient conditions. For such non-linear waves, it can be shown that different parts of the wave propagate at different speeds relative to a rest frame of reference[1], yielding a rarefaction wave spreading and distorting as it propagates. In order to characterize the rarefaction wave motion, it is essential to study the phenomenon with the non-linear equations. The rarefaction waves do not change the entropy of the fluid as they pass through.

$$\frac{\partial u}{\partial t} + (u+a) \frac{\partial u}{\partial x} + \frac{1}{\rho a} \left(\frac{\partial p}{\partial t} + (u+a) \frac{\partial p}{\partial x} \right) = 0 \quad (2.13)$$

$$\frac{\partial u}{\partial t} + (u+a) \frac{\partial u}{\partial x} - \frac{1}{\rho a} \left(\frac{\partial p}{\partial t} + (u+a) \frac{\partial p}{\partial x} \right) = 0 \quad (2.14)$$

The Equations (2.13) and (2.14) have been obtained from the 1-D Euler equations for momentum and modified version of the continuity equation described by Equations (2.15) and (2.16).

$$\frac{1}{c^2} \frac{d p}{d t} + \rho (\nabla \cdot \vec{U}) = 0 \quad (2.15)$$

$$\rho \frac{d \vec{U}}{d t} + \vec{\nabla} p = 0 \quad (2.16)$$

The compatibility equations (2.17) and (2.18) describe the relations between flow variables along two of the characteristic curves of the governing Euler equations. These characteristic lines

correspond to the left and right propagating sound waves in the fluid. The quantity c used in the formulations is the local speed of sound for the gas.

$$du + \frac{dp}{\rho c} = 0 \quad (2.17)$$

$$du - \frac{dp}{\rho c} = 0 \quad (2.18)$$

Equations (2.17) and (2.18) are further integrated along the characteristic curves, yielding the Riemann invariants represented in Equations (2.19) and (2.20).

$$J_+ = u + \frac{2c}{\gamma-1} = C_1 \quad (2.19)$$

$$J_- = u - \frac{2c}{\gamma-1} = C_2 \quad (2.20)$$

Here, C_1 and C_2 are arbitrary constants. For a family of simple waves, it can be demonstrated that at least one family of characteristic curves are straight lines[1]. For a left propagating expansion fan, the characteristic curves corresponding to J_- can be shown to be straight lines. Since the family of rarefaction waves prior to their contact with the left wall of the shock tube are studied, they can be considered to be a family of simple waves. Given that one family of characteristics are straight lines, it can further be demonstrated that J_+ is constant through the expansion fan.

$$u + \frac{2c}{\gamma-1} = C \quad (2.21)$$

C in the equation is a constant across the expansion fan. The J_+ Riemann invariant is used at the station 4 in figure 2.1 to compute the undetermined constant C_1 . The equations (2.22)-(2.26) are then used to determine the distribution of fluid properties across the expansion fan.

$$u_4 + \frac{2c_4}{\gamma-1} = 0 + \frac{2c_4}{\gamma-1} \quad (2.22)$$

$$\frac{c}{c_4} = 1 - \frac{(\gamma-1)}{2} \left(\frac{u}{c_4} \right) \quad (2.23)$$

$$\frac{T}{T_4} = \left[1 - \frac{(\gamma-1)}{2} \left(\frac{u}{c_4} \right) \right]^2 \quad (2.24)$$

$$\frac{p}{p_4} = \left[1 - \frac{(\gamma-1)}{2} \left(\frac{u}{c_4} \right) \right]^{\frac{2\gamma}{\gamma-1}} \quad (2.25)$$

$$\frac{\rho}{\rho_4} = \left[1 - \frac{(\gamma-1)}{2} \left(\frac{u}{c_4} \right) \right]^{\frac{2}{\gamma-1}} \quad (2.26)$$

The last piece of information required to characterize the expansion fan corresponds to obtaining the fluid particle velocity as a function of time, which is obtained from the family of characteristics corresponding to straight lines.

$$\frac{dx}{dt} = (u - c) \quad (2.27)$$

$$x = (u - c)t + C_3 \quad (2.28)$$

$$x = (u - c_4 + \frac{\gamma-1}{2}u)t + C_3 \quad (2.29)$$

The constant C_3 is then determined from the initial position of the diaphragm.

2.2.4 The Sod's shock tube

The shock tube is a canonical case for testing compressible flow solvers for two reasons:

- Simple setup and computationally inexpensive- Since the lateral dimensions of the tube are much smaller compared to the longitudinal dimensions, it is sufficient to solve the 1-

D N-S equations. A further simplification is introduced from disregarding the effects of viscosity at the walls on the shock speed. Thus, the 1-D Euler equations are solved across the flow domain.

- Despite the relatively inexpensive setup and computational rigor required to solve for the flow field variables within the domain, the shock tube provides crucial insights into the resolution of shocks by compressible flow solvers.

For the reasons mentioned above, the Sod's shock tube was chosen as a 1-D validation case.

The governing 1-D Euler equations are

$$\left\{ \begin{array}{l} \frac{\partial \rho}{\partial t} + \frac{\partial (\rho U)}{\partial x} = 0 \\ \frac{\partial (\rho U)}{\partial t} + \frac{\partial (\rho U^2)}{\partial x} = -\frac{\partial p}{\partial x} \\ \frac{\partial (\rho E)}{\partial t} + \frac{\partial (\rho U E)}{\partial x} = -\frac{\partial (pU)}{\partial x} \\ E = e + \frac{1}{2} U^2 \end{array} \right. \quad (2.30)$$

In order to make the problem well-posed, appropriate boundary and initial conditions are to be specified.

Inviscid slip boundary conditions are applied at all the bounding surfaces of the shock tube domain. Inviscid slip boundaries enforce zero penetration into the bounding walls, and zero thermal and pressure gradients in a direction normal to the surfaces. The initial conditions imposed correspond to the Sod's shock tube [37], wherein normalized values of pressure, temperature and velocity given by the equations are imposed.

$$[\rho, U, p] = [1, 0, 0] \text{ for } x < 0.5 \quad (2.31)$$

$$[\rho, U, p] = [0.125, 0, 0.1] \text{ for } x \geq 0.5 \quad (2.32)$$

The computational domain is discretized into 800 divisions for a domain extending along the x-axis, $0 \leq x \leq 1$. The time step is chosen as $\Delta t = 0.25 \Delta x$.

The numerical schemes used for discretizing the various terms of the Euler equations are presented in Chapter 3.

2.3 ONERA S8 Transonic channel

As introduced in Chapter 1, type-B SBLI are of importance in transonic flows within turbomachinery passages. The ONERA report presents experiments conducted to study the phenomenon of shock induced separation in the S8 transonic wind tunnel situated at ONERA. The report presents extensive mean field data, gathered specifically to validate 2-D Navier Stokes codes simulating turbulent flow. It was therefore chosen as the second validation case.

A comprehensive description of the mechanisms of several SBLI's can be found in [15]. Below, a brief description of the type-B interaction is provided. The impinging normal shock wave of type-B interactions assert a large adverse pressure gradient on the boundary layer, causing the boundary layer to thicken, and eventually separate [15]. The mechanism for the boundary layer thickening results from the upstream influence of the pressure rise across the shock, which is transmitted through the subsonic layer. The effect is evident in Figure 2.2. A normal shock wave of sufficient strength is able to induce flow separation in the presence of any geometrical restriction. The induced flow separation displaces the flow streamlines further upwards. The thickening of the boundary layer in turn acts as a "ramp", resulting in the formation of compression waves, which coalesce to the oblique leg C_1 of the shock wave [15]. Downstream to the oblique leg, the flow is still supersonic, and the pressure at states 2 and 3 is

not the same. The second oblique leg C_2 is formed as a consequence leading to compatibility in pressure at the states 3 and 4. The various stations are depicted in the figure .

The consequent “smearing” of the normal shock structure to the lambda shock structure is thus a result of the interaction process. An appropriate choice of turbulence modelling is thus necessary to capture the point of separation, the start of the interaction process, and thus the lambda shock structure at the right position.

As mentioned in section 1.4, a secondary consequence of the interaction process is that the flow field is characterized by large scale unsteadiness, with low frequency motions of the shock and “breathing” of the separated bubble. Some aspects of the interaction-dynamics will be elaborated in Chapter 4 .

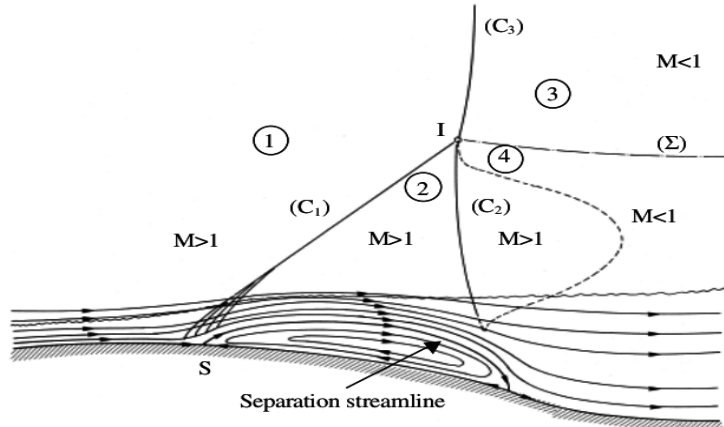


Figure 2.2 Close-up view of the interaction process

Source: *Shock wave boundary layer interactions*, Holger Babinsky & John K. Harvey, Page.6

2.3.1 Computational model

The experimental setup of the ONERA transonic S8 wind tunnel is depicted in the Figure 2.3. The setup consists of an upstream stagnation chamber that supplies air at a total temperature of 300 K and total pressure of 0.95 Bar. There exists the possibility of placing two inter-changeable bumps at the test section. A series of experiments were reported involving the placement of either a single bump or both the bumps. The case corresponding to the use of a single bump placed at the bottom of the channel was chosen to study the phenomenon of shock induced separation. The mass flow rate in the channel, and the subsequent placement of the “lambda” shock was controlled by the use of the adjustable second throat.

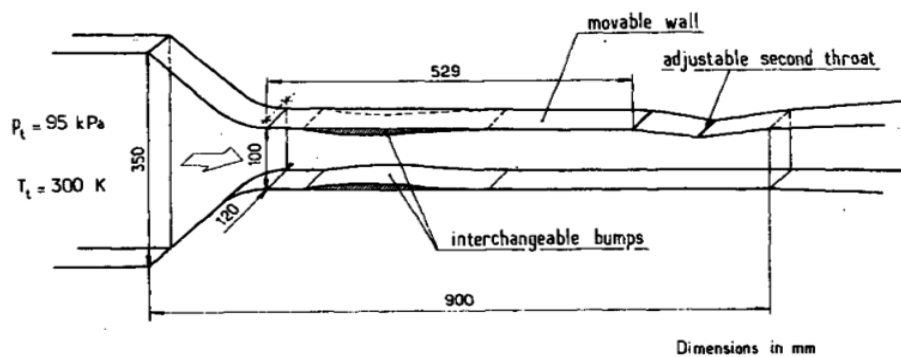


Figure 2.3 Experimental setup at ONERA

Source: *Experimental Investigation of Turbulence properties in Transonic Shock/Boundary layer interactions*

The governing equations used for the particular test case are the compressible 2-D Navier-Stokes equations. The problem was solved in 2 separate stages, as presented.

- The 2-D compressible Euler equations were solved to obtain the inviscid flow field. The solution comprised of a normal shock placed downstream to the throat of the wind tunnel.
- The 2-D compressible viscous, laminar NS equations were solved in the flow domain. A normal shock placed downstream to the throat of the wind tunnel was obtained. The normal shock was characterized by low frequency motion.

2.3.2 Geometry

- The 2-D compressible NS equations coupled to the $k-\omega SST$ turbulence model were employed to obtain the unsteady flow field in the domain. A justification for the choice of the turbulence model is provided in Chapter 3. The lambda shock structure executing low frequency motion was obtained.

The overall geometry of the ONERA S8 wind tunnel is described in the Figure 2.4. For a precise definition of the bump, the reader is referred to the ONERA report [8]. The geometry was constructed in ANSYS design modeler. Once the geometry was constructed, the block-structured approach was adopted to generate the computational meshes in ANSYS ICEM. A justification for constructing block structured grids is provided in Chapter 3. The structure of the blocks is presented in Figure 2.5

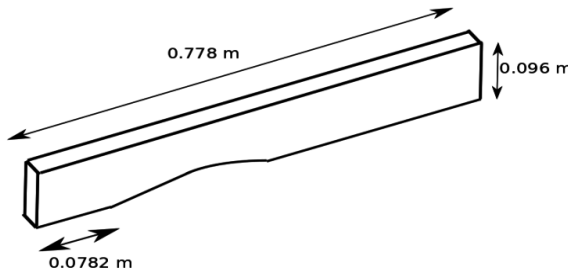


Figure 2.4 Isometric view of the flow domain

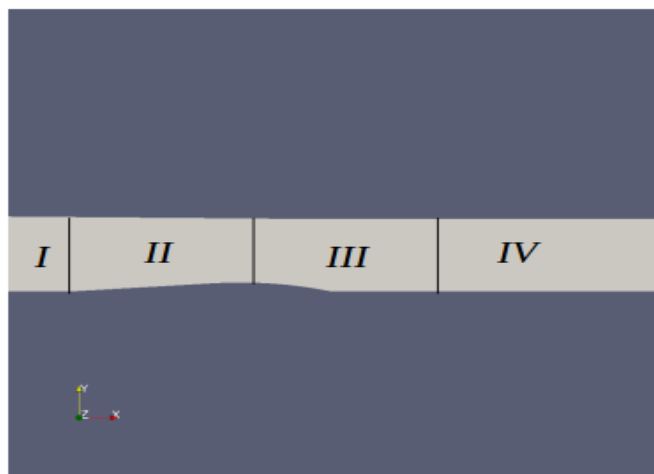


Figure 2.5 Structure of the blocks

As common in CFD studies, it is important to demonstrate the spatial convergence of the flow fields. For this purpose, 3 different computational grids were chosen in increasing order of number of cells.

Grids	Number of finite volume cells	Δy_{wall} (m)	Minimum Δx_{wall} (m)	Maximum Δx_{wall} (m)
coarse	331890	3×10^{-5}	3×10^{-4}	3×10^{-3}
medium	825845	2.14×10^{-5}	2.14×10^{-4}	2.14×10^{-3}
fine	1606302	1.5×10^{-5}	1.5×10^{-4}	1.5×10^{-3}

Table 2.1 Computational mesh details

Specific details of the chosen grids are provided in the Table 2.1. The grids were chosen keeping the computational cost in mind, thus restricting the maximum allowable cell count in the medium grid to within a million. In all the grids, the cell growth ratios were restricted to 5 %, and the maximum allowed cell aspect ratios in the boundary layer of the blocks II and IV was restricted to 50. Higher aspect ratio cells were allowed in blocks I and IV .

The sponge zone (Block IV) features an increasing 5 % growth ratio towards the outlet. The purpose of the grid stretching in the streamwise direction is to minimize the reflection of the outgoing pressure waves at the boundary. Such reflections often interfere with and contaminate the solution within the flow domain. Semlitsch (2014) describes the increased numerical dissipation generated in a coarse mesh. The progressively increasing numerical dissipation introduced from grid stretching results in increasingly poor resolution of the outgoing pressure waves, ultimately leading to their dissipation.

The grid resolution was kept high in block III, with maximum allowed cell aspect ratios in the boundary layer of 10. The discretization along the coordinate directions was specified, based on the Taylor micro-scale. The specification of the Taylor micro-scale is important for numerical turbulent flow computations. The Taylor micro-scale is defined in terms of the two-point correlation in literature. In order to understand the relevance of the Taylor micro-scale for turbulent flow computations, the turbulence kinetic energy spectrum for homogeneous turbulence is presented in Figure 2.6.

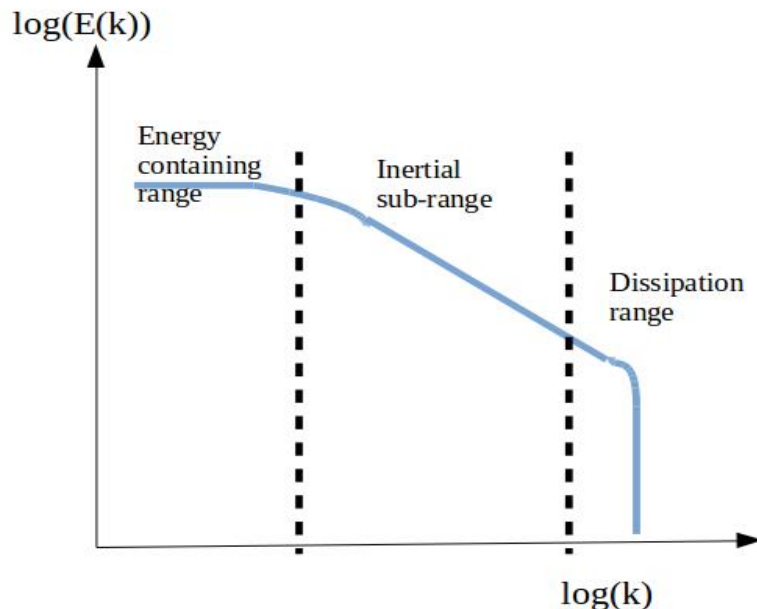


Figure 2.6 Turbulence kinetic energy spectra for homogeneous turbulence

The logarithm of the turbulence kinetic energy is plotted against the logarithm of the wave number of turbulent flow structures in Figure 2.6. As seen from the plot, the inertial sub-range forms a bridging transition from the energy containing range of the turbulent structures to the dissipation range of turbulence structures. The inertial sub-range is characterized by a -5/3 slope in the plot, indicating a decay of the turbulent kinetic energy with increasing wave number of the turbulent flow structures. The energy transfer in this range takes place statistically from the large flow structures to the smaller flow structures [31]. The Taylor micro-scale lies at the transition between the inertial subrange and the dissipation range. At and below this scale, fluid viscosity begins to affect the dynamics of the turbulent structures significantly. The turbulent structure motion at these length scales are statistically universal and are uniquely governed by the fluid viscosity and the dissipation rate, as stated by Kolmogorov's first hypothesis. Therefore, the computational cell size is chosen in such a way that it is capable of spatially resolving at least the Taylor micro-scale limit.

The estimation of the Taylor micro-scale was done based on the formulation presented in equation [31] for homogeneous turbulence. The formulation was based on the assumption that at these scales, the rate of production of the eddies is in balance with the dissipation of the eddies.

$$P = 15 \nu \frac{u'^2}{\lambda^2} \quad (2.33)$$

$$\epsilon = \frac{u'^3}{l} \quad (2.34)$$

P and ϵ in the Equations (2.33) and (2.34) are the rates of production and dissipation of the turbulent flow structures. ν represents the kinematic viscosity of the fluid, u' represents the local root mean square of the velocity fluctuations, λ represents the Taylor micro-scale and l represents the length scale of the large energy containing turbulent flow structures. The large energy containing turbulent flow structures l are estimated as a few percent of the geometrical restriction, in this case, the channel height H of the wind tunnel. The value specified in Equation 2.35 was obtained from Walin (2015) [39].

$$l = 0.07 H \quad (2.35)$$

Equating the rate of production with the dissipation, the Taylor micro-scale is given by Equation (2.36) .

$$\lambda = \sqrt{\frac{15 \nu l}{u'}} \quad (2.36)$$

The near wall distance for the first grid line was set based on a non-dimensional near wall distance (y^+) at block III. The formulations given by Equations (2.37)-(2.55) were used to determine the near wall distance Δy .

$$\mathfrak{R}_x = \frac{xU}{\nu} \quad (2.37)$$

$$C_f = 2 * 0.0296 \mathfrak{R}_x^{-1/5} \quad (2.38)$$

$$u_\tau = U \sqrt{\frac{1}{2} C_f} \quad (2.39)$$

$$\Delta y = \frac{y^+ \nu}{u_\tau} \quad (2.40)$$

\Re_x represents the Reynolds number at a streamwise station x , U is the local fluid speed, ν is the local kinematic viscosity, C_f is the non-dimensional turbulent friction coefficient, and u_t is the local friction velocity.

2.3.3 Boundary conditions

The inlet boundary conditions for the problem were setup based on the experimental values of inlet stagnation pressure & temperature. Experimental values for the air at stagnation conditions were 0.95 Bar and 300 K. Besides, the outlet static pressure of 0.61 Bar was specified in order to model the effect of the second adjustable throat, and fix the mean position of the lambda shock to the appropriate experimental location. The maximum mach number in the experimental flow domain of 1.42 was used to adjust the position of the lambda shock.

Moreover, the velocity at the inlet was modeled to enter perpendicular to the inlet cross section, which is a fair assumption, given the symmetry of the upstream converging nozzle in figure. The corresponding velocity boundary condition at the inlet, utilized for the purpose is able to handle instances of reversed flow that occur during the first few iterations of the computation.

Since the flow at the outlet is subsonic, the a single physical boundary condition is to be specified. The other variables, including temperature and velocity were extrapolated from the interior. No-slip boundary conditions were specified at the walls, which enforce zero velocity at the walls coupled with zero gradients of scalar variables normal to the wall.

For the turbulent flow simulations, the $k-\omega$ SST turbulence model solves two additional transport equations for the turbulent kinetic energy k and the turbulence frequency ω , in order to compute the eddy viscosity. Further, the eddy viscosity is introduced in the NS equations in order to compute the effective viscosity, described in Chapter 3. Boundary conditions at the inlet for these transport equations are specified via a turbulence intensity of 10 %. Equations (2.41)-(2.46) were further used to set the values of the turbulent kinetic energy and the turbulence frequency from the specified turbulence intensity.

$$l=0.07 H \quad (2.41)$$

$$u'=\sqrt{u_x'^2+u_y'^2+u_z'^2} \quad (2.42)$$

$$U=\sqrt{U_x^2+U_y^2+U_z^2} \quad (2.43)$$

$$u'=IU \quad (2.44)$$

$$k=\frac{3}{2} u'^2 \quad (2.45)$$

$$\omega=\frac{k^{0.5}}{C_\mu^{0.25} l} \quad (2.46)$$

Where I is the turbulence intensity, k the turbulent kinetic energy, ω the turbulence dissipation rate, and C_μ is a model coefficient for the turbulence model used.

The inlet speed U based on the value obtained from the inviscid flow simulation was used for the computations in Equations (2.41)-(2.46). Based on the restriction on number of computational cells within the flow domain, the near wall grid distance was set at $y^+ \sim 20$ for the medium grid. Therefore, the transport equations could not be integrated into the viscous sub-layer, right up to the wall. Boundary conditions at the walls for the transport equations were therefore, specified through standard compressible wall functions in *foam-extend-3.2* presented in Chapter 3. At the outlet, the values for the turbulence kinetic energy and turbulence frequency were extrapolated from the interior.

The initial velocity in the domain was set at 200 ms^{-1} , static pressure to 0.60 Bar and temperature to 300 K.

2.4. Linear cascade of nozzle guide vanes (NGV)

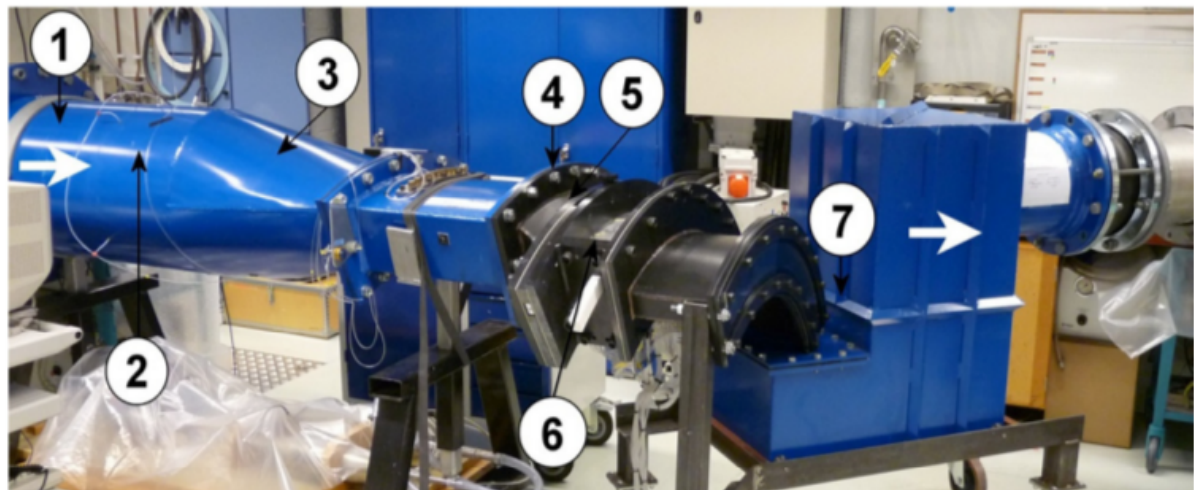
2.4.1 Methodology

A systematic 3 step process was employed in order to simulate the flow through the linear cascade of nozzle guide vanes introduced in Chapter 1, with a view to characterize the combustion noise.

- The 2-D compressible Navier-Stokes equations coupled with the $k-\omega SST$ turbulence model are used to obtain the unsteady flow field.
- The flow solution from step 1 was used to initialize all the span-wise planes of an extruded 3D domain. The 3-D compressible Navier-Stokes equations coupled with a compressible LES module was used to resolve the flow within the blade passages. The results from the computation are to be attested against the experimental results.
- A low frequency, sinusoidal temperature signal is to be introduced to the inlet of the flow domain, modeling the entropy waves from the combustion chamber. Work of Papadogiannis et al. (2014) introduces entropy spots at the inlet of the computational domain of frequency 2 kHz, as sinusoidal fluctuations over a reference total temperature.

2.4.2 Experimental setup

Experiments to investigate the loss mechanism of a High pressure NGV cascade were carried out at the Department of Energy Technology, KTH by Yasa Tolga and Jens Fridh[38]. The experimental study aimed at quantifying the aerodynamic kinetic energy loss, due to the presence of secondary flow structures within the blade passages. Besides, flow measurements were carried out to characterize flow unsteadiness, like vortex shedding downstream to the nozzle guide vanes. A view of the annular sector cascade test facility is provided in Figures 2.7, while Figure 2.8 illustrates a view of the NGV blade passages.



(1) Inflow, (2) Settling chamber, (3) First radial contraction, (4) Turbulence grid, (5) Second radial contraction, (6) Test sector with NGVs, and (7) Outflow

Figure 2.7 Far view of the Annular sector cascade testing facility

Source: Aerodynamic investigation of leading edge contouring and external cooling on a Transonic turbine vane,
Ranjan Saha

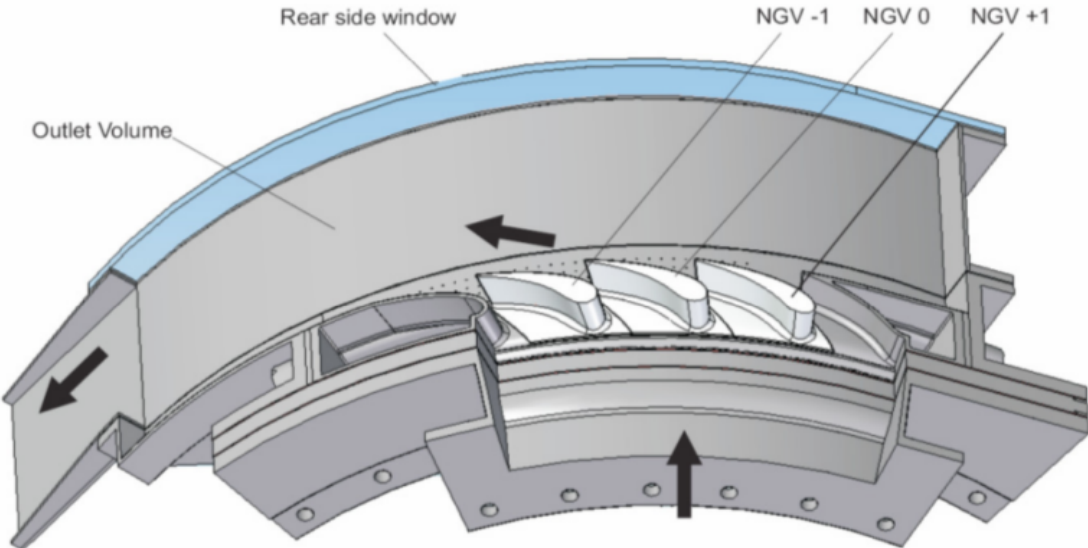


Figure 2.8 Annular sector cascade, Part 6 of experimental test facility

Source: Aerodynamic investigation of leading edge contouring and external cooling on a Transonic turbine vane,
Ranjan Saha

Some of the geometrical parameters of the NGV cascade at the hub are depicted in Figure 2.9.

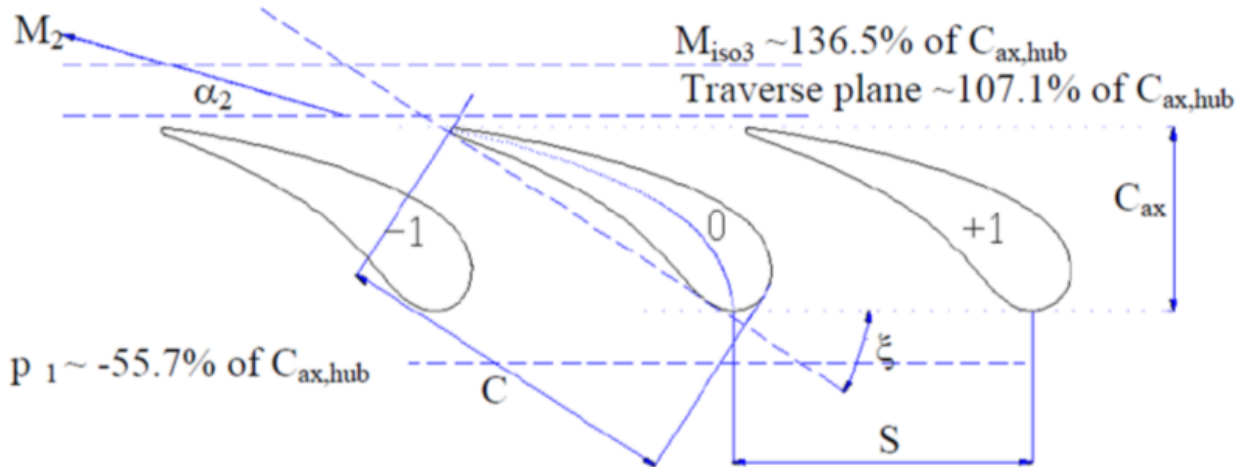


Figure 2.9 Geometrical parameters and important stations in the annular sector

Source: Aerodynamic investigation of leading edge contouring and external cooling on a Transonic turbine vane,
Ranjan Saha

Important parameters described in the Figure 2.9 include the the axial chord C_{ax} and the location of the inlet plane, where the total pressure measurements have been carried out [38]. The inlet plane is located around 55 % C_{ax} upstream to the nozzle guide vane cascade.

There is some 3-dimensionality to each of the nozzle guide vanes, apparent in the small radial variation of the axial chord from the hub to the tip of the NGV cascade. Besides, there is a small axial variation in the height of a vane, from the leading edge to the trailing edge, which is visible

in the meridional view of the vane in Figure 2.10. The definition of the coordinate system followed for the annular sector cascade available in [34] has been followed.

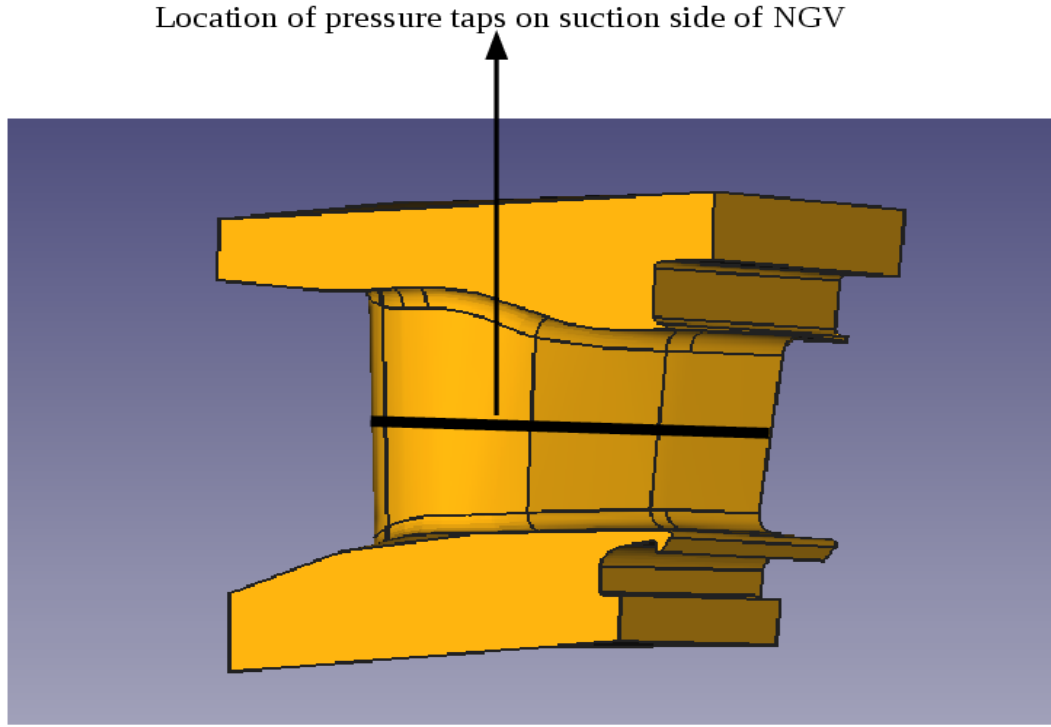


Figure 2.10 Meridional view of a single vane

2.4.3 The experiment

Operating conditions for the annular sector cascade have been set by specifying the static pressure at the outlet plane of the cascade, for specific stagnation conditions at the upstream plane (Figure 2.9).

The study was carried out across 6 different outlet pressures, the outlet being situated at the distance of an axial chord away from the leading edge of a nozzle guide vane. By fixing the outlet pressures at six different values, an investigation of the flow field in the cascade across the subsonic, transonic and supersonic regimes has been carried out. The outlet pressures have been expressed in terms of isentropic outlet Mach numbers, as depicted in Figure 2.11. The outlet plane is situated at a distance of an axial chord away from the leading edge of a nozzle guide vane. The following experimental results gathered were used for the validation of the solver:

- **NGV loading** Pressure taps situated at mid-height, on the pressure and suction sides of the NGV surface record static pressure. The curves representing the axial variation of the pressure on the suction and pressure sides have been marked separately in Figure 2.11. The location of the pressure taps on the suction side of a single vane can be seen in Figure 2.10. The pressure readings have been expressed in terms of the isentropic Mach number in Figure 2.11, assuming isentropic expansion from stagnation conditions reported at the inlet. Equation (2.47) provides the formulation for the same.

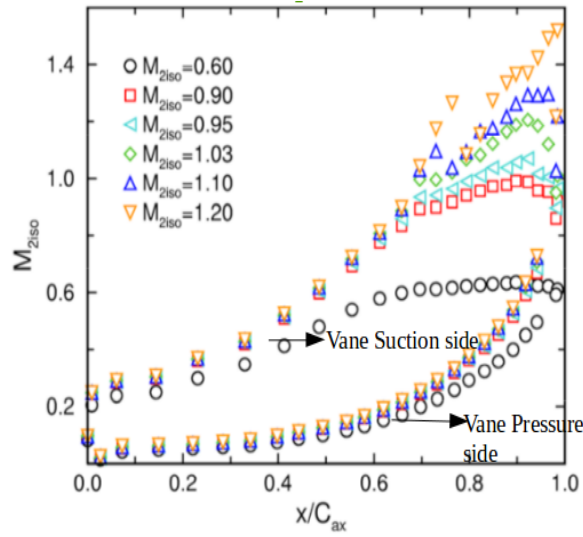


Figure 2.11 Axial distribution of isentropic Mach number along the surfaces of a vane

Source: *Investigation of the Loss Mechanism of a HP NGV [KTH Internal Report]*

$$\frac{p_0}{p_2} = \left(1 + \frac{\gamma - 1}{2} M_{2\text{iso}}^2\right)^{\frac{\gamma}{\gamma - 1}} \quad (2.47)$$

In Equation (2.47), p_0 is the stagnation pressure reported upstream to the nozzle guide vane cascade, p_2 is the pressure measured along the axial extent of the vane and $M_{2\text{iso}}$ is the axial isentropic Mach number distribution. The results for the axial, isentropic Mach number distribution constitute the first step in the validation of the solver.

- **Circumferential isentropic Mach number distribution at a distance of 40 % C_{ax} downstream to the hub of the cascade**

Experimental data were acquired for the isentropic Mach number distribution at the hub of the NGV cascade, along the circumferential direction/vane phase. The isentropic Mach number distribution was recorded for the six different outlet pressures, characterizing the subsonic, transonic and supersonic regimes of the fluid flow in the cascade. The Figure 2.12 represents the variation of the non-dimensionalized pressure against the vane phase for different outlet pressures/isentropic outlet Mach numbers.

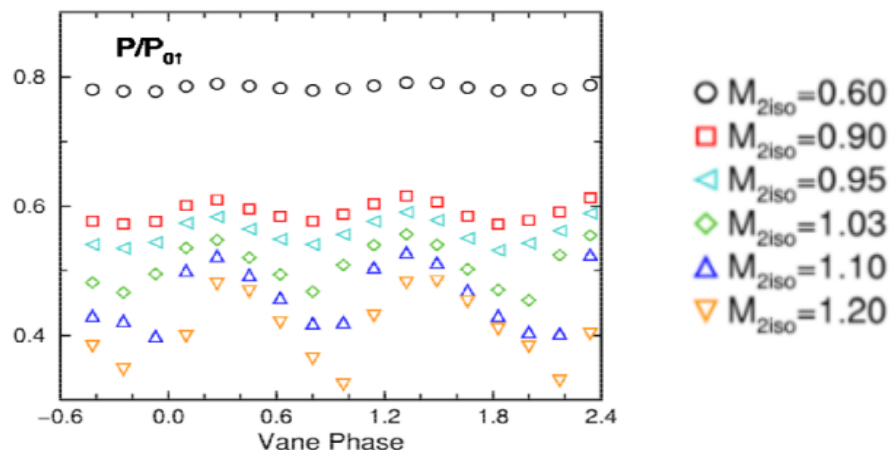


Figure 2.12 Isentropic Mach number distribution along the vane phase

Source: *Investigation of the Loss Mechanism of a HP NGV [KTH Internal Report]*

These experimental results constitute the second step for the validation of the solver.

- **Nozzle guide vane wake measurements at 4 planes downstream to the NGV cascade**

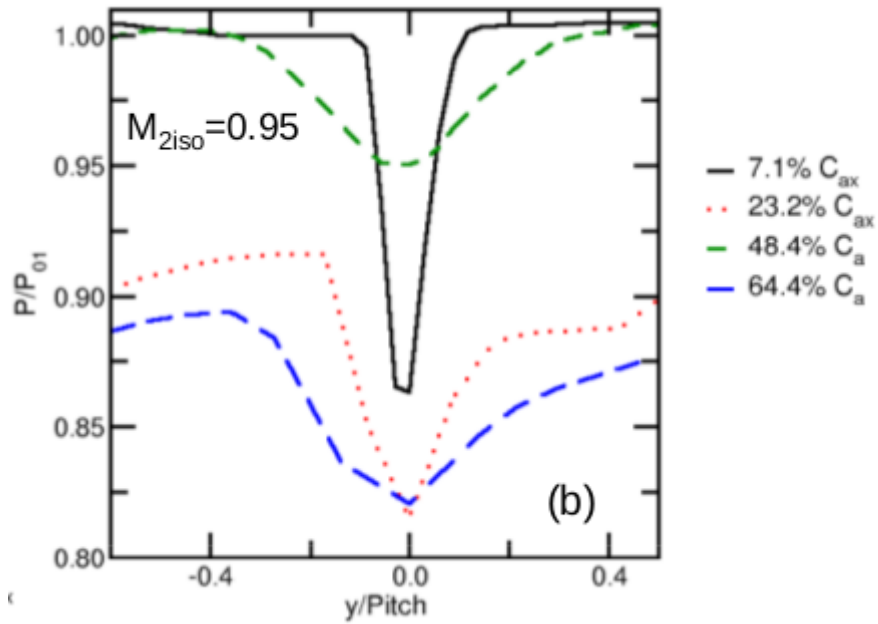


Figure 2.13 Downstream normalized total pressure distribution

Source: Investigation of the Loss Mechanism of a HP NGV [KTH Internal Report]

Experimental data was acquired for the total pressure measurements at the wakes of the NGV cascade. Calibrated data at two downstream planes at a distance of 7.1% C_{ax} and 48.4% C_{ax} to the cascade at mid-span were chosen for the validation [38]. These experimental results constitute the third step for the validation of the solver. The data at the two other downstream planes were not considered for validation due to improper calibration of the utilized probes.

- **Unsteady flow measurements at a plane downstream to the NGV cascade**

Experimental data was acquired for the unsteady flow measurements downstream to the cascade to characterize the vortex shedding frequency. The data at a downstream plane at a distance of 23.2% C_{ax} to the cascade were used for the same. These experimental results constitute the fourth step in the validation of the solver.

2.4.4 Computational model of the cascade

The annular sector cascade consists of 6 nozzle guide vanes arranged in a circular fashion. Special efforts were made to maintain flow periodicity along the circumferential direction [30]. Figure 2.12 illustrates the point made above, with flow periodicity maintained in the circumferential direction at isentropic outlet mach numbers less than 1. (denoted as vane phase in the figure).

A first computational approximation of the cascade model would then involve constructing a computational flow domain enclosing one or two of the central vanes in the cascade, with the sides being modeled by periodic boundary conditions [21]. Such computations have been carried out by Tolga et al. (2010) [38]. These CFD calculations are computationally expensive, and therefore, a further simplification was sought to construct the flow domain. Literature [14] reports a further approximation in the design of the computational domain. A 2-D linear cascade

approximation to the 3-D annular sector cascade is suggested in case the height of the annulus enclosing the guide vanes is small compared to the inner radius of the cascade. The ratio of the leading edge height of a vane to the inner radius of the annulus for the cascade under consideration is ~ 0.1 . This provided the justification to unwrapping the 3-D sectoral cascade to the 2-D linear cascade. Despite the three-dimensional character of the vanes mentioned in a prior section, the linear cascade approximation was deemed appropriate in order to gain a first insight into the flow within the blade passages. In order to simulate the turbulent eddies within the passages, the 2-D linear cascade of the NGV was extruded in the third direction to a thickness of the trailing edge height of a nozzle guide vane. Further, in order to simulate entropy noise, which is generated due to acceleration of entropy blobs through the confined cascade passages, at least one entire passage around a central vane was to be included in the computational domain.

Specific details of the construction of the computational domain are presented in the sub-section describing geometry and CAD modeling.

Geometry and CAD modeling

The aim of the performing the CAD modeling was to obtain the linear cascade of nozzle guide vanes, from the annular sector cascade geometry provided. The corresponding CAD modeling was carried out in **Siemens-NX**. The following steps were employed for the same:

1. Three of the nozzle guide vanes were assembled side-by-side, as depicted in the Figures 2.14 and 2.15.

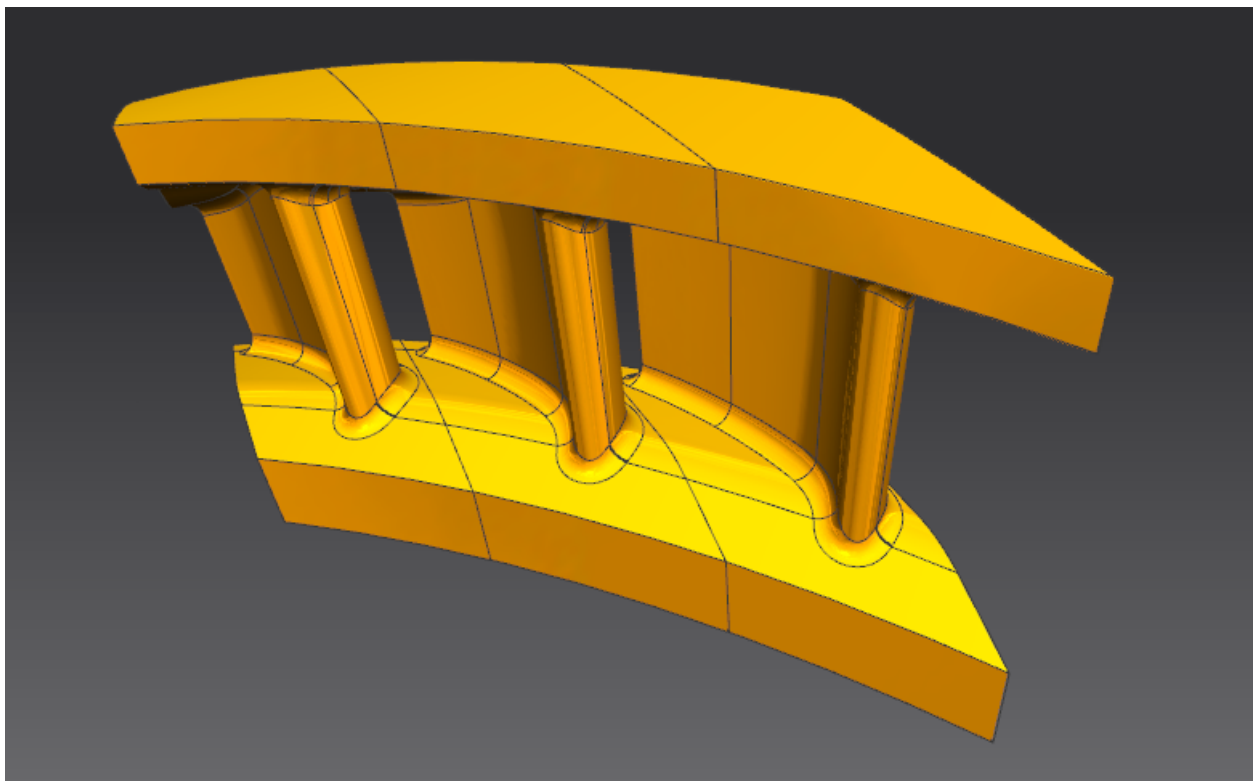


Figure 2.14 Assembly of the nozzle guide vanes

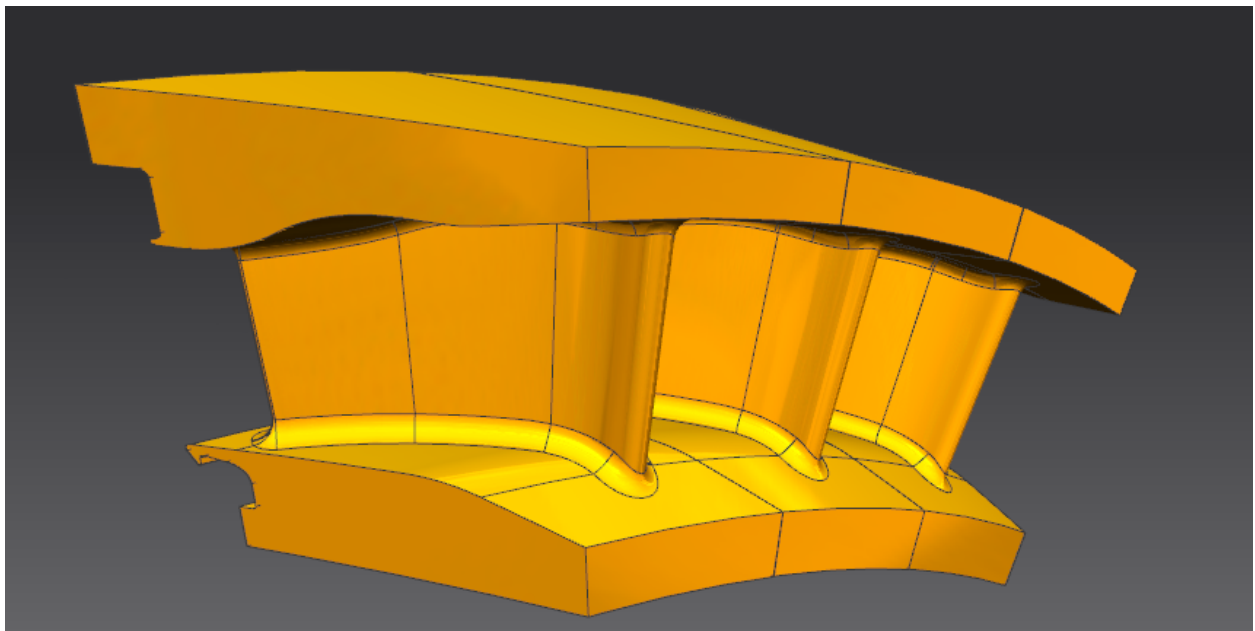


Figure 2.15 Side view of the annular sector assembly

2. The center of curvature of the arrangement was determined, as depicted in Figure 2.16.

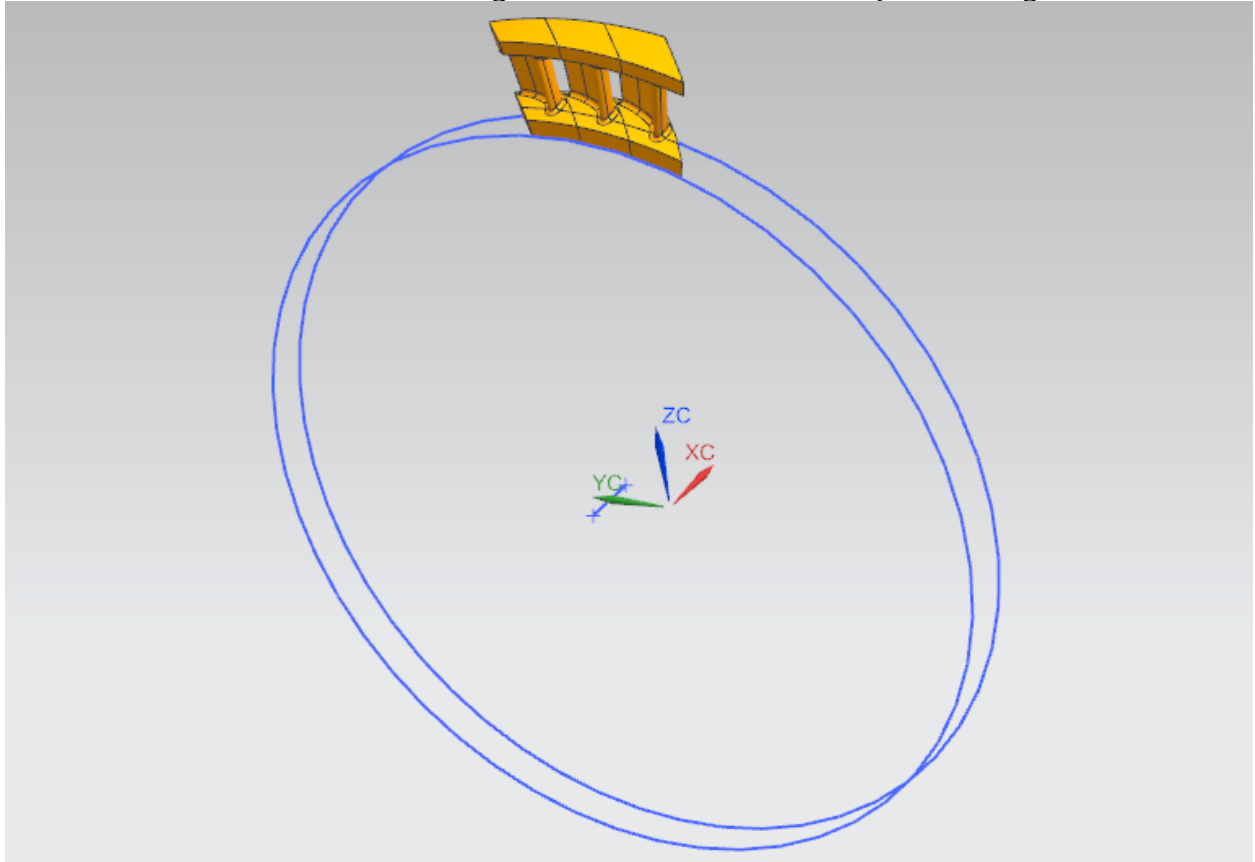


Figure 2.16 Determination of the center of curvature of the annular sector cascade

3. A sectioning plane was determined, passing through the mid-point of the trailing edge of a vane, and sectioning it along an equal radius from the center of curvature as depicted in Figures 2.17 and 2.18.

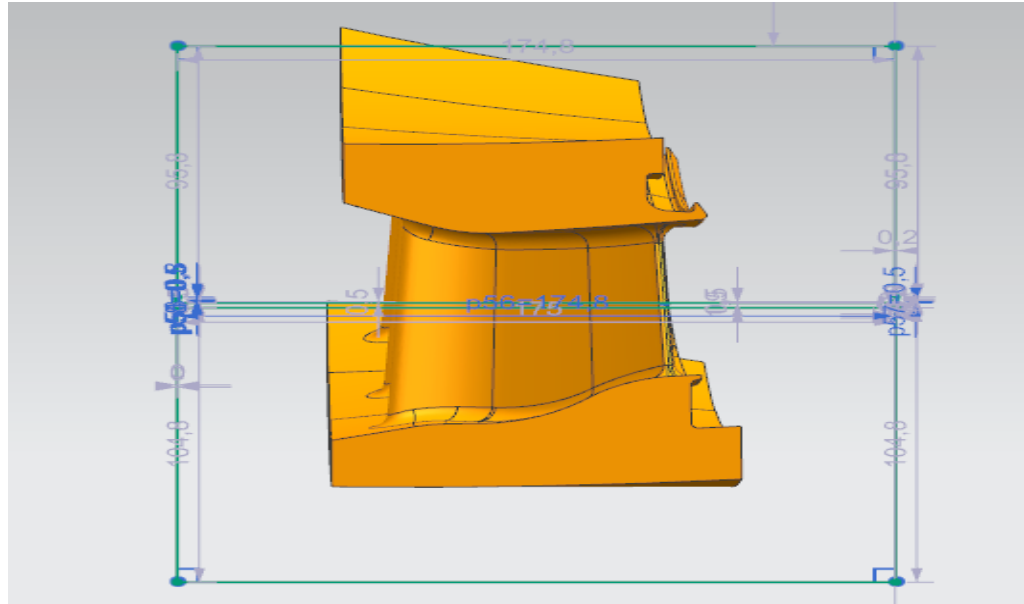


Figure 2.17 Sectioning plane through a single vane

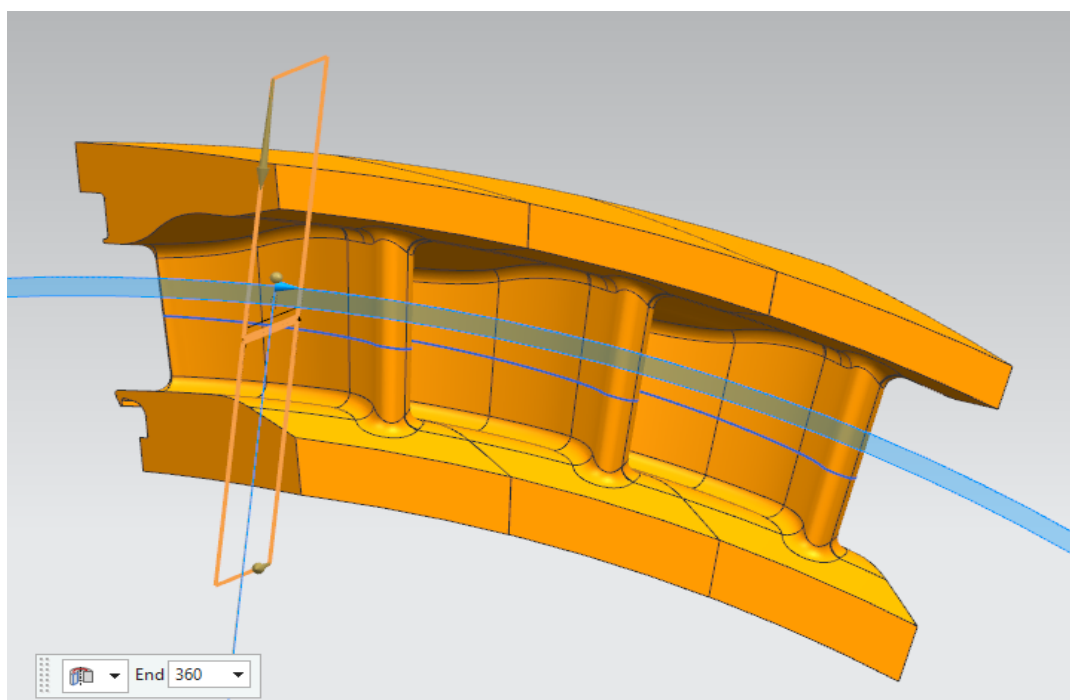


Figure 2.18 Sectioning plane swept across the three vanes in the cascade

4. The sectioning plane was swept across all three nozzle guide vanes, thus generating a mid-section profile of the nozzle guide vane arrangement. The result is depicted in Figures 2.19.

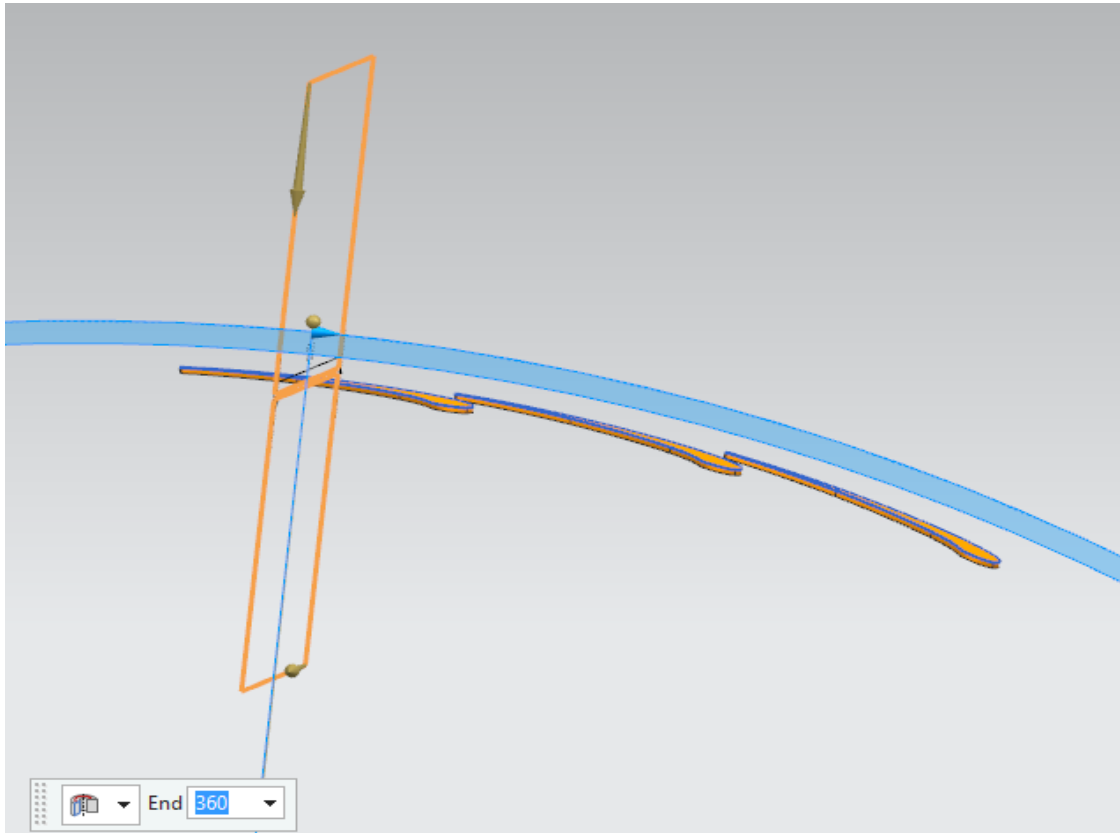


Figure 2.19 Mid-section of the annular sector cascade

5. Unwrapping the mid section profile of the nozzle guide vane arrangement along a plane. As depicted in figure 2.20, the plane was tangential to the surface of a nozzle guide vane. A linear cascade of the Nozzle guide vane arrangement was obtained upon unwrapping, as depicted in Figure 2.20.

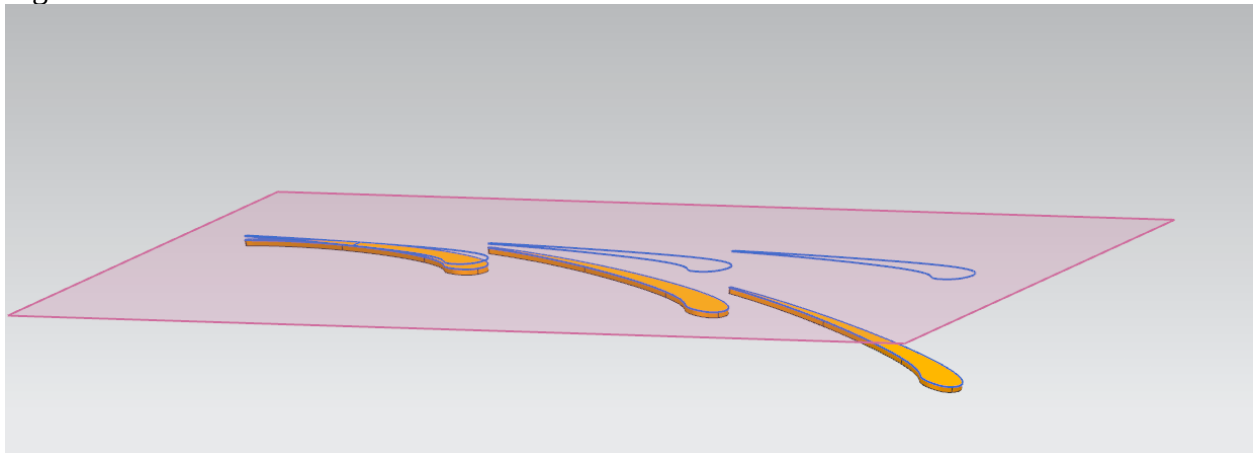


Figure 2.20 Unwrapping the mid-section of the annular sector cascade along a tangential plane

6. Constructing the domain in ICEM CFD

The unwrapped 2-D sections of the linear cascade of nozzle guide vanes were enclosed in a domain in ANSYS ICEM, as depicted in Figure 2.21. The sides of the domain were constructed to within a tolerance of 10^{-8} , for applying the periodic boundary conditions effectively, as described in the section on boundary conditions.

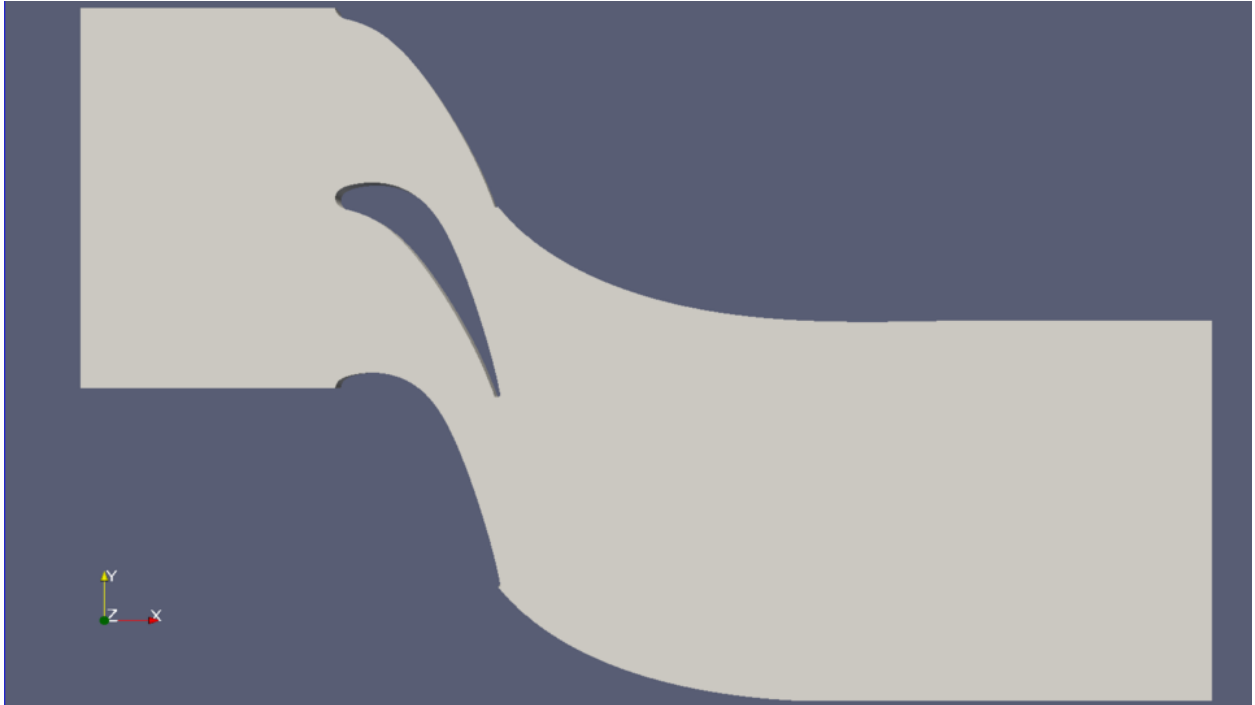


Figure 2.21. Front view of the domain in ParaView

2.4.6 Block structured meshing in ICEMCFD

Constructing block structured grids are the most appropriate for Finite volume computations since they can be aligned along the flow, and capture the flow gradients the most accurately. Figure 2.22 illustrates an overall view of the block structure in the flow domain. Around the vanes, it is important to resolve the boundary layer accurately. In this context, it is important to satisfy the mesh orthogonality with the vane walls. This would ensure that the grid is wrapped around the vane surface, and therefore the computational cell faces would be aligned along the flow direction. This would lead to a better resolution of the flow gradients by the computational mesh. In order to ensure mesh orthogonality with the vane walls, the O-grid topology was used to mesh the regions around the vanes, as depicted in Figure 2.22. Everywhere else in the domain, the H-grid topology was used.

The blocks were constructed in a manner to keep the mesh orthogonality throughout the computational domain within acceptable limits set by the solver. A continuum of computational cell sizes across all the blocks was enforced. The computational cell count was kept to within 536000, based on computational costs. A near wall distance was set based on a non-dimensional near wall distance of $y^+ \sim 20$. The Equations (2.52)-(2.55) were used to estimate the near wall distance Δy from the non-dimensional near wall distance. The cell aspect ratios at the wall were kept to within 35.

Figures 2.23-2.24 shows some views of the mesh.

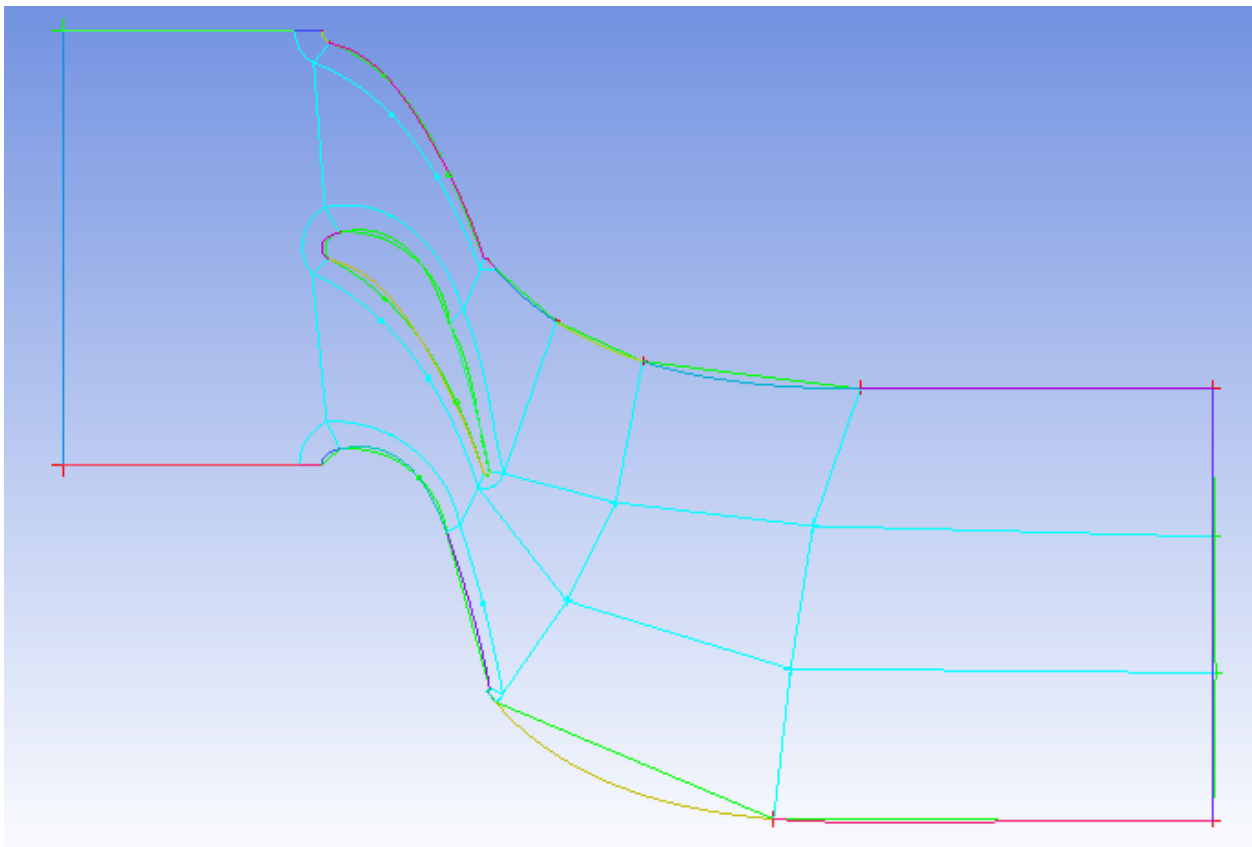


Figure 2.22 Front view of the domain in ICEMCFD

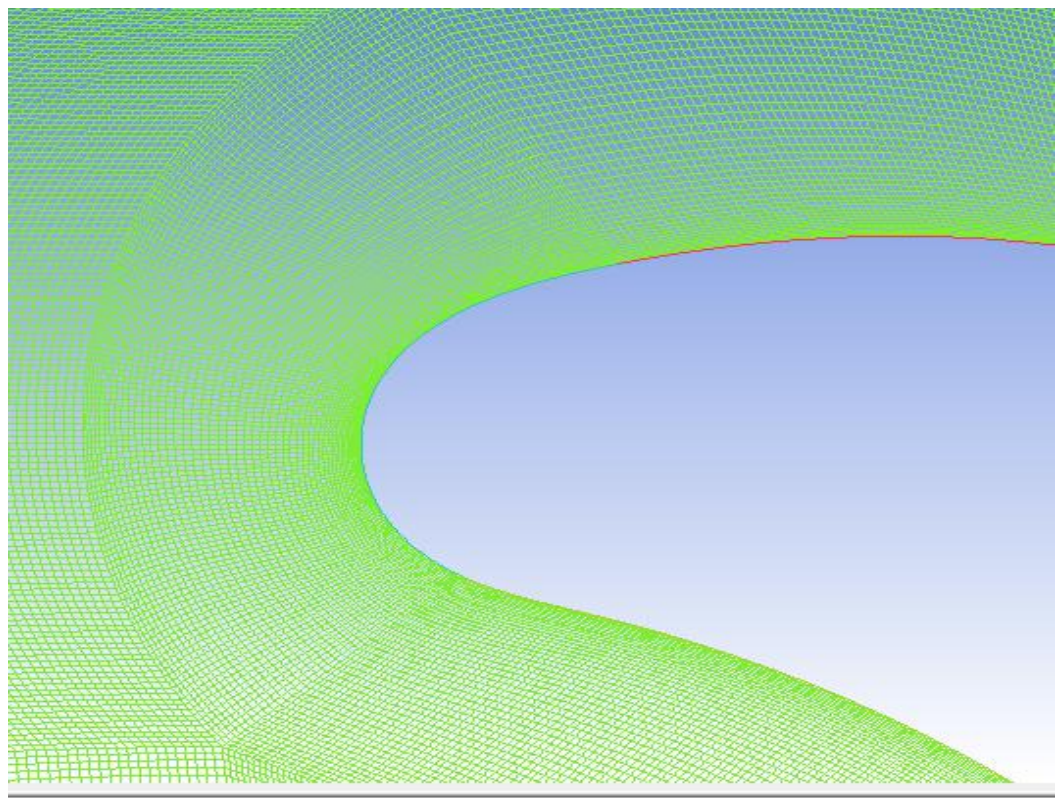


Figure 2.23 View of the O-grid mesh around the central vane leading edge

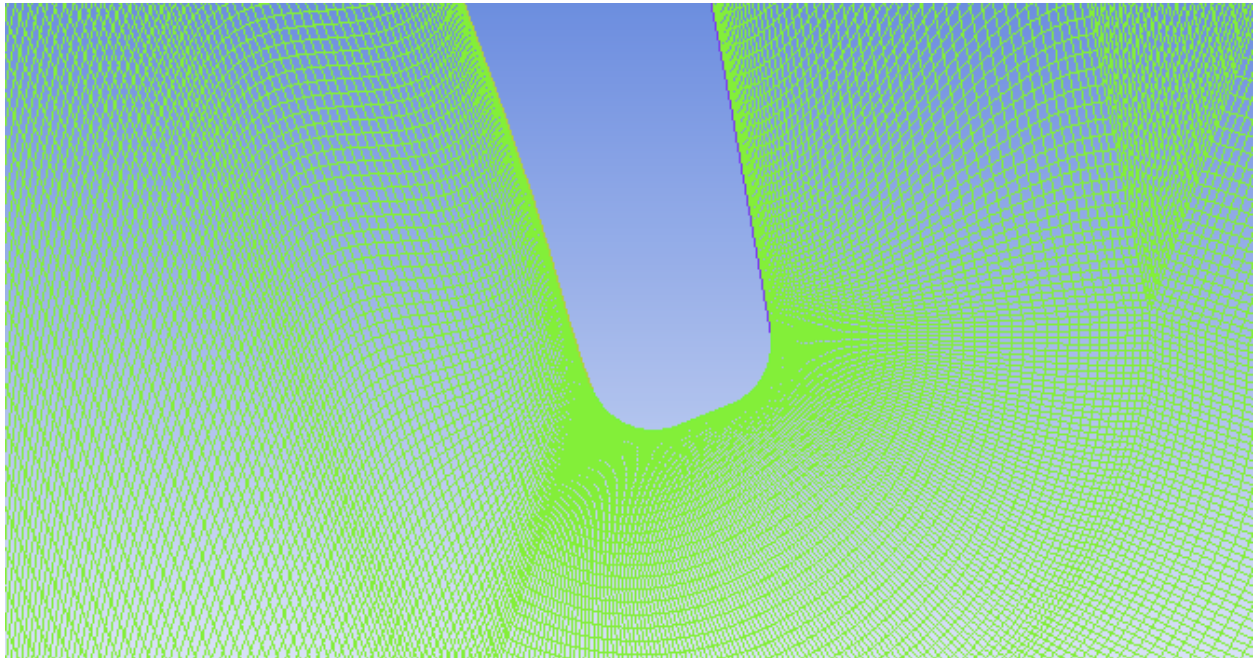


Figure 2.24 View of the O-grid mesh around the central vane trailing edge

2.4.7 Boundary conditions

Figure 2.25 illustrates the various bounding surfaces of the geometry. The inlet boundary conditions for the problem were setup based on the experimental values of inlet stagnation pressure and temperature. Experimental values for the air at stagnation conditions of 1.871 Bar were set at the inlet. Besides, a static temperature of 303.15 K was specified at the inlet of the cascade.

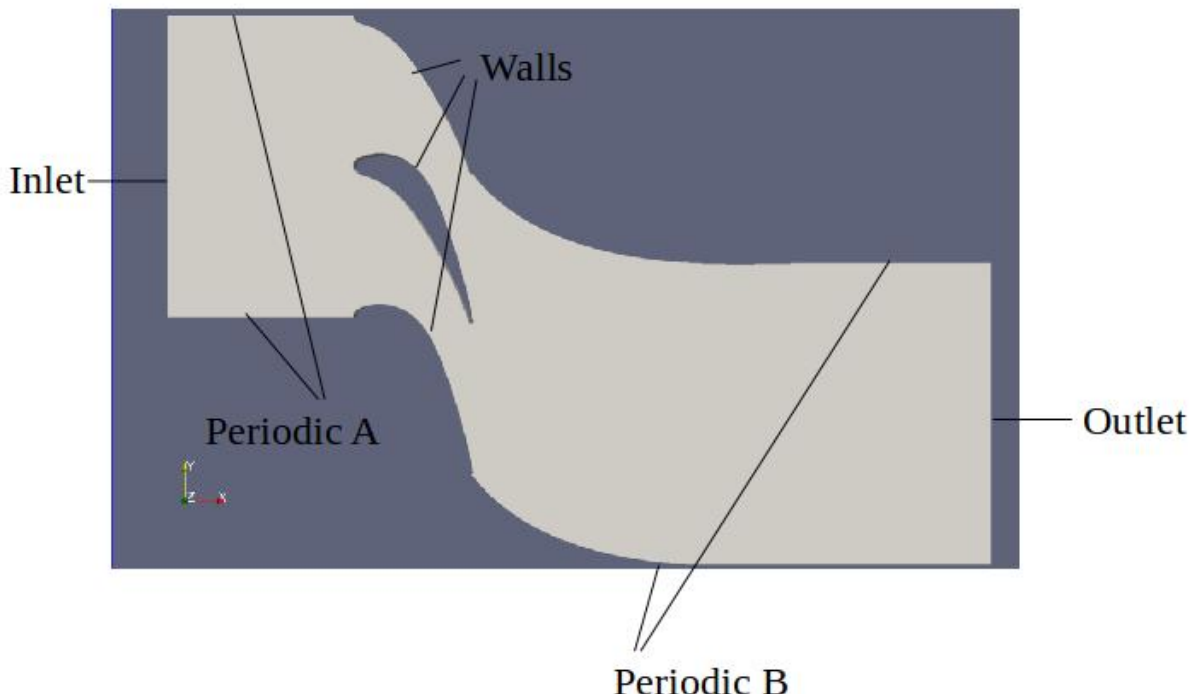


Figure 2.25 Different boundary surfaces of the geometry

Hirsch (2007) [13] recommends the specification of total temperature conditions at the inlets for compressible flow calculations, based on the theory of characteristics. Therefore, from the application of the isentropic flow relations at the inlet of the cascade, the stagnation temperature was estimated based on an inlet Mach number of 0.15, specified in Figure 2.11. Equation (2.62) was used for the computing the inlet stagnation temperature T_0 from the static temperature T at the inlet and the inlet Mach number to the cascade.

$$\frac{T_0}{T} = 1 + \frac{(\gamma - 1)}{2} M_{in}^2 \quad (2.62)$$

To set the mass flow rate of air through the domain, the face averaged static pressure of 1.04370 Bar was prescribed at the outlet of the flow domain, corresponding to the experimental values maintained. This “weak” formulation for the outlet static pressure is used for turbo-machinery applications since the values for the static pressure across the entire outlet are not precisely monitored and controlled during experimental trials. Thus, specifying the face averaged static pressure is consistent with the real physical conditions present in the experimental cascade.

The velocity at the inlet was calculated based on the volumetric flux φ , and was enforced to enter perpendicular to the inlet section. The boundary condition *pressureInletOutletVelocity* was used for the purpose. The boundary condition takes into account the occurrence of reversed flow, in which case the *zeroGradient* (extrapolation from interior) boundary condition is applied. The no-slip boundary conditions are imposed on the surface of the vanes, corresponding to zero flow velocity and zero gradients of other flow variables in a direction normal to the wall. At the outlet, employing the *zeroGradient* boundary condition all quantities excluding the pressure are extrapolated from the interior. Periodic boundary conditions are applied at the sides of the domain based on the periodicity of the flow observed experimentally. A detailed description of the periodic boundary condition can be found in Malasekara & Versteeg.H [21]. Essentially, the periodic boundary condition enforces the outflow across a boundary as the inflow across its corresponding specified pair, thus enforcing periodicity in the flow along specified directions.

In order for the cyclic boundary condition to work successfully, the pairs of periodic boundaries must be of the exact same length and each pair of connecting discretized faces are required to have their areas matching within a certain tolerance [<http://openfoam.org/release/2-0-0/meshing/>, *cyclic boundary condition*]. Given the requirements on the quality of the mesh, such a mesh was difficult to construct, for the particular flow domain and therefore, inevitably, different discretizations were imposed across the pairs of the periodic boundaries designated as ‘periodic B’ in Figure 2.25. Therefore, a new boundary condition *cyclicGgi* (*Cyclic generalized-grid interface*) implemented into the *foam-extend-3.2* was employed to apply the periodic boundary conditions at the sides of the domain [6]. The generalized grid interface is able to couple two non-conformal mesh regions at the matrix level of the solver. This is achieved by the evaluation of suitable weighting factors to be multiplied with the fluxes through the opposing set of overlapping computational cell facets, thus distributing the flux appropriately across the pair of non-conformal meshes. Figure 2.26 illustrates the concept of facets. Here, it is seen that the patch through which the flux is computed is termed the ‘master’ patch, while the corresponding pair is called the “slave” patch. In order for the flux transfer to work, the algorithm translates the slave patch by a user specified distance to the master patch. Further, the algorithm evaluates suitable weighting factors to be multiplied with the fluxes through the overlapping facets.

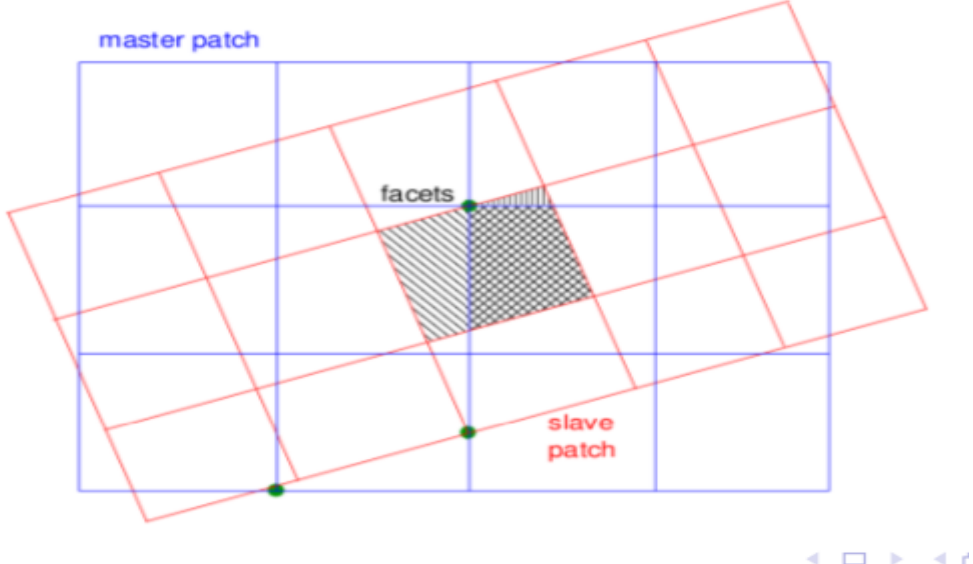


Figure 2.26 Concepts involved in the cyclicGgi boundary condition

Source: OpenFOAM training workshop

For the turbulent flow simulations, the $k-\omega$ SST turbulence model solves two additional transport equations for the turbulent kinetic energy k and the turbulence frequency ω , in order to compute the eddy viscosity. Boundary conditions at the inlet for these transport equations are specified via a turbulence intensity of 1 %, corresponding to experimentally determined values. Equations (2.41)-(2.46) were further used to set the values of the turbulent kinetic energy and the turbulence frequency from the specified turbulence intensity.

The speed U applied at the inlet was obtained from an inviscid flow computation of the flow through the domain. This was used for the computations in Equations (2.41)-(2.46) to estimate the turbulent kinetic energy and turbulence frequency at the inlet. Based on the restriction on number of computational cells within the flow domain, the near wall grid distance was set at $y^+ \sim 20$ for the computational mesh. Therefore, the transport equations could not be integrated into the viscous sub-layer, right up to the wall. Boundary conditions at the walls for the transport equations were therefore specified through standard compressible wall functions in *foam-extend* presented in Menter et al.[25]. At the outlet, the values for the turbulence kinetic energy and turbulence frequency were extrapolated from the interior.

Initial conditions

The initial velocity in the domain was set at 80 m s^{-1} , static pressure to 1.04370 Bar and temperature to 304 K. These initial conditions were chosen in order to reduce the simulation time.

3 SIMULATION OF TURBULENCE AND NUMERICAL SETUP

3.1 Turbulence

Turbulence is a phenomenon encountered in several flows existing in nature. Notably, it inevitably influences industrial processes as well. A turbulent flow is characterized by irregularities in fluid properties tending to chaotic fluctuations in flow properties and the existence of regions of rotational flow motion called eddies. Depending on a specific scenario, turbulence can either be desirable or undesirable. The three-dimensional, irregular and chaotic behavior of turbulence are essential in mixing processes, such as in the air-fuel mixing in Internal combustion engines. It can be demonstrated that the mixing generated by turbulence is orders of magnitude higher than the mixing generated by molecular mixing [19]. Nevertheless, the property of enhanced mixing associated with turbulence is also responsible for the enhanced drag forces generated at the bounding walls of a fluid domain. For instance, in aircraft, the skin friction drag force exerted by a turbulent boundary layer is several times higher than that exerted by a laminar boundary layer. Efforts are therefore made in order to delay the location of the transition from laminar to turbulent flow on aircraft wings to reduce the enhanced drag forces.

A non-dimensional quantity, the free-stream Reynolds number is used to distinguish the different flow regimes associated with laminar flow, transitional and turbulent flows. The Reynolds number defined for this purpose is represented by Equation (3.1).

$$\mathcal{R} = \frac{\rho U L}{\mu} \quad (3.1)$$

Where, U is the characteristic velocity scale of the flow, L is the characteristic length scale of the flow, μ is the dynamic viscosity of the fluid and ρ is the fluid density. Physically, the Reynolds number is the ratio of inertial forces to the viscous forces in a fluid. A turbulent flow is generally characterized by a large free-stream Reynolds number and therefore a predominance of inertial forces over viscous forces.

There is a continuum of fluctuation scales in a turbulent flow from the largest so called integral scales to the smallest Kolmogorov scales. The concept of the continuum of fluctuation scales in a turbulent flow is described concisely with the aid of the Figure 3.1. Figure 3.1 illustrates the time history of a turbulent signal $u(t)$ at a point, depicting the wide range in fluctuation scales. Upon closer inspection of the turbulent time signal with a higher magnification, self-similar irregularities are observed [23]. At the highest possible magnification, when one approaches the fluctuation scales associated with the Kolmogorov scales, one can finally observe a smooth variation in the time history, with no further irregularities apparent in the signal. A similar observation about the existence of a continuum in length scales right up to the Kolmogorov scale for a turbulent flow can be made.

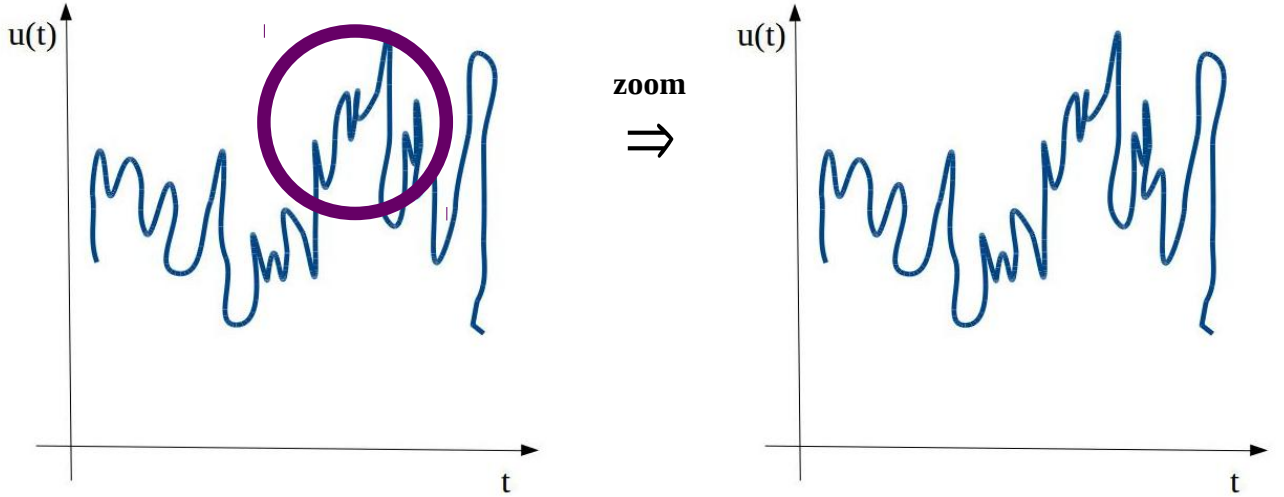


Figure 3.1 Inspecting the time history of a turbulent signal over a smaller time interval

With increasing free-stream Reynolds numbers, turbulent flows are characterized by the existence of an increasing span of temporal and spatial fluctuation scales. Johansson and Walin (2014) describe the two scenarios responsible for this widening span of fluctuation scales with increasing Reynolds numbers.

Moreover, it can be shown that the computational time associated with simulating a turbulent flow is directly related to the range of the associated fluctuation scales. The non-dimensional Reynolds number based on the size of the largest fluctuation scales, \mathfrak{R}_Λ provides a direct measure for the ratio of the largest to the smallest fluctuation scales for a turbulent flow in quasi-equilibrium [19].

$$\mathfrak{R}_\Lambda = \frac{\Lambda \bar{u}'}{v} \quad (3.2)$$

$$\frac{\Lambda}{\eta} = \mathfrak{R}_\Lambda^{\frac{3}{4}} \quad (3.3)$$

In the Equation (3.2), Λ is the integral length scale, or the length scale associated with the largest fluctuation scale, \bar{u}' is the velocity scale associated with these fluctuation scales and v is the kinematic viscosity of the fluid. The size of the smallest fluctuation length scale η is inversely related to the dissipation rate ϵ occurring at these scales, and therefore, decreases with the increase in the range for fluctuation scales to be simulated.

$$\epsilon \sim \frac{(\bar{u}')^3}{\Lambda} \quad (3.4)$$

$$\eta \sim v^{\frac{3}{4}} \epsilon^{\frac{-1}{4}} \quad (3.5)$$

Since the computational cell is required to resolve the smallest fluctuation scale, one realizes that the number of cells in the domain should increase with increasing Reynolds number. The argument is complete when one considers that the computational effort and time are directly

proportional to the number of grid points. The considerations provided so far summarize the difficulty in the Direct Numerical Simulation (DNS) of a turbulent flow at the high Reynolds numbers encountered in practice. A brief description of alternative approaches are provided in the section 3.2.

3.2 A review of approaches used to simulate turbulent flow

Direct Numerical Simulations (DNS) involve a complete resolution of all the fluctuation scales in the flow. Since the span of fluctuation scales grows with increasing Reynolds numbers, it is seen that the computational cost associated with a DNS increases with an increase in the free-stream Reynolds number. Under the view point of computational costs, DNS is currently feasible only for simulating the flow over simple geometries at moderately high Reynolds numbers. DNS is therefore restricted to academic research aiming at understanding fundamental physical phenomena requiring a high spatial and temporal resolution.

Large Eddy Simulations (LES) can involve a considerable reduction in computational costs over a DNS. Often, LES resolve the fluctuation scales in the energy containing range and most of the scales in the inertial sub-range. The fluctuation scales in the dissipation range are modeled. The present work has tested a compressible LES solver with a one equation transport equation to model the eddies in the dissipation range. Despite the reduction in computational effort associated with a LES relative to a DNS, a LES demands a high grid resolution which is particularly pronounced in flows with compressibility effects such as shock waves.

The Unsteady Reynolds-Averaged Navier-Stokes (URANS) approach involves a further reduction in computational cost. The use of a sufficiently small global time step across all cells in the computational domain, to advance the averaged compressible fluid flow equations can lead to the resolution of large scale flow unsteadiness inherent in the flow. The URANS method resolves the fluctuation scales only in the energy containing range depicted in Figure 2.6. The fluctuation scales in the inertial sub-range and the dissipation range are modeled instead, relaxing the requirements on the grid. Therefore URANS simulations can be performed on coarse grids, and several parameter studies are possible to be carried out in a relatively short time. The current project has utilized the $k-\omega$ SST two-equation turbulence model for reasons stated in section 3.10. Specific details of the URANS approach and LES approach are explored in the next sections.

3.3 Compressible Unsteady Reynolds averaged Navier-Stokes (URANS) simulations

3.3.1 Methods for averaging a turbulent flow quantity

Based on the characteristics of the turbulent flow, three methods for the averaging of the turbulent flow quantities are reported by Jasak [18] (1996):

- Ensemble averaging

An ensemble average of a randomly fluctuating flow quantity can be defined as the average of the flow quantity over a large number of flow realizations starting from the same initial conditions. For example, the ensemble average $\bar{U}(\mathbf{x}, t)$ for the velocity $U(\mathbf{x}, t)$ along a coordinate direction is computed from Equation (3.7).

$$\bar{U}(\mathbf{x}, t) = \lim_{N \rightarrow \infty} \frac{1}{N} \sum_i U^{(i)}(\mathbf{x}, t) \quad (3.7)$$

In Equation (3.7), N represents a series of identical experiments conducted to study the evolution of a turbulent flow field having the same initial conditions. The ensemble averaging represents the most general form of averaging.

- Time averaging

For the case of flows where the time scale for changes in the mean flow field is several times larger than the time scale for changes in the fluctuation scale, the ensemble average reduces to the time average. Equation (3.8) represents the mathematical definition of the time averaged cartesian component of the velocity $\bar{U}(x)$.

$$\bar{U}(x) = \lim_{T \rightarrow \infty} \frac{1}{T} \int_{t_0}^{t_0+T} U(x, t') dt \quad (3.8)$$

In Equation (3.8), T represents the experimental time over which the turbulent flow field is allowed to develop from its initial state at time t_0 . The URANS simulations performed in this work are based on solving the time-averaged NS equations.

- Spatial averaging

For the case of homogeneous turbulence, the fluctuations in turbulent flow quantities are independent of the spatial location in the flow domain. In such case, the ensemble averaging reduces to spatial averaging.

For each of the methods of averaging presented, there are two versions of averaging, corresponding to the relative importance of density fluctuations in the turbulent flow field. The first version employed in case of negligible density fluctuations, is known as Reynolds-averaging. For the case of large density fluctuations about the mean density, a density weighted averaging technique known as Favre-averaging is employed instead.

3.3.2 Reynolds decomposition

In order to deal with the vast span of fluctuation scales in a turbulent flow, Reynolds adopted a method involving the statistical splitting of the turbulent flow quantity such as pressure p , density ρ or a cartesian component of the fluid velocity U into a mean component and the fluctuation component around the mean. This process of splitting the flow quantity U into it's mean \bar{U} and fluctuating parts u' is also known as Reynolds decomposition, as represented by Equation (3.6).

$$U(x, t) = \bar{U}(x, t) + u'(x, t) \quad (3.6)$$

The aim of the Reynolds decomposition is then to quantify the first order effects of the turbulent fluctuations on the mean fields, without fully resolving the fluctuation scales. This is achieved by deriving the equations for the mean flow quantities.

3.3.3 The Favre decomposition and averaging operation for large density variations

Large density fluctuations are implicit to flows with large compressibility effects. For example, the fluctuating heat release rates associated with turbulent combustion in a jet engine could result in large fluctuations of the fluid density at the inlet of the first stage of the turbine stator. Therefore, it becomes important to take these density fluctuations into account while determining the time-averaged mean flow quantities. Considering a Reynolds decomposition of pressure, density and flow velocity in order to construct the time-averaged NS equations introduces several correlation terms [3]. In order to reduce the number of correlation terms to be modeled, Favre introduced a method of computing the averages of the flow quantities based on density

weighting. The operator developed by Favre is expressed mathematically in Equation (3.9), for the time average of U .

$$\tilde{U}(x) = \frac{\rho \bar{U}}{\bar{\rho}} \quad (3.9)$$

The turbulent flow quantity U is further decomposed into its Favre average and non-centred fluctuation [3].

$$U = \tilde{U} + u'' \quad (3.10)$$

The properties of the Favre decomposition are expressed in Equations (3.11)-(3.12) for U .

$$(\rho u'') = 0 \quad (3.11)$$

$$\bar{u}' = 0 \quad (3.12)$$

3.3.4. Favre-Averaged Navier-Stokes Equations

Upon introducing the Favre decomposition to the governing Equations (2.3)-(2.5), in the absence of body forces, the Favre-Averaged Navier-Stokes Equations presented in Equations (3.13)-(3.15) are obtained. The Favre decomposition is applied to all flow variables except for flow density and pressure [3]. Further simplifications have been introduced in order to obtain the Equations (3.13)-(3.15), involving dropping some additional correlation terms. These simplifications are reported to be reasonable for flow regimes below the hypersonic limit.

$$\frac{\partial \bar{\rho}}{\partial t} + \frac{\partial (\bar{\rho} \tilde{U}_i)}{\partial x_i} = 0 \quad (3.13)$$

$$\frac{\partial (\bar{\rho} \tilde{U}_i)}{\partial t} + \frac{\partial (\bar{\rho} \tilde{U}_i \tilde{U}_j)}{\partial x_j} = -\frac{\partial \bar{p}}{\partial x_i} + \frac{\partial (\sigma_{ij} + \tau_{ij})}{\partial x_j} \quad (3.14)$$

$$\frac{\partial (\bar{\rho} \tilde{E})}{\partial t} + \frac{\partial (\bar{\rho} U_j E)}{\partial x_j} = -\frac{\partial (\bar{p} \tilde{U}_j)}{\partial x_j} + \frac{\partial ((\sigma_{ij} + \tau_{ij}) U_i)}{\partial x_j} - \frac{\partial q_j^{\text{total}}}{\partial x_j} \quad (3.15)$$

Newly introduced terms include the Reynolds stress in compressible flows τ_{ij} , the total heat flux q_j^{total} , comprising the contributions from the molecular transport term q_j^{lam} and the turbulent transport term q_j^{turb} . Further, the turbulent kinetic energy k , a correlation of the fluctuation velocities u_i'' is defined. The heat flux contribution from the molecular transport term is related to the Favre-averaged temperature by the Fourier's law. Finally, the mean pressure \bar{p} is computed from Equation (3.19).

$$\tau_{ij} = -\rho u_i'' u_j'' \quad (3.16)$$

$$q_j^{\text{lam}} = -c_p \frac{\mu}{Pr} \frac{\partial \tilde{T}}{\partial x_j} \quad (3.17)$$

$$q_j^{\text{turb}} = c_p \rho u_j'' T \quad (3.18)$$

$$\bar{p} = (\gamma - 1) \bar{\rho} \left(\tilde{E} - \frac{\tilde{U}_k \tilde{U}_k}{2} - k \right) \quad (3.19)$$

$$k = \frac{\tilde{u}_k \tilde{u}_k}{2} \quad (3.20)$$

3.3.6. Boussinesq's Hypothesis

The Favre-averaged equations have introduced more variables than the available number of equations. This is referred to as the turbulence closure problem. In order to close the system of equations, the additional introduced correlation terms are modeled, based on certain hypothesis. Boussinesq in 1877 had proposed that turbulent transport of momentum be modeled the same way as the molecular transport. Along these lines, the Reynolds stress terms are represented in terms of the strain rate tensor, analogous to the viscous stress tensor.

$$-\rho \bar{u}_i \bar{u}_j = \mu_T (2 S_{ij} - \frac{2}{3} S_{kk} \delta_{ij}) \quad (3.21)$$

In Equation (3.21), the scalar μ_T represents the turbulent eddy viscosity. Such a representation of the Reynolds stress represents a huge reduction in the size of the model since the 6 components of the stress tensor are now represented by a single scalar. The eddy viscosity is in turn a scalar proportional to the product of the local velocity scales \bar{u} and local length scales Λ of the large energy containing eddies.

$$\mu_T \sim \Lambda \bar{u} \quad (3.22)$$

The eddy viscosity and the molecular viscosity are added and represented together as μ_{eff} .

3.3.7. Eddy viscosity models

The aim of performing the Reynolds decomposition for the flow field is so that the Navier-Stokes equations are used only to resolve the effects of the turbulent fluctuation scales on the mean fields. All the turbulent fluctuation scales are modeled instead. Eddy viscosity models (EVM) are based on the Boussinesq hypothesis, and are first moment closure models. Thus, the mean flow is resolved by these models, while the second statistical moment of the flow quantities are modeled. Johansson and Walin (2014) [19] provide a review of various types of eddy viscosity models. The present work is based on the solution to the 2-equation model to compute the eddy viscosity throughout the flow domain. Here, one solves two transport equations for 2 quantities in order to determine the local velocity and length scales of the large energy containing eddies. Further, the local eddy viscosity is computed from Equation (3.22). The two quantities could either be the Turbulent kinetic energy k and the turbulence dissipation rate ϵ or k and the turbulence frequency ω .

3.3.8. The $k-\omega$ SST model

Of the eddy-viscosity models in literature, the $k-\omega$ SST model represents the best compromise between capturing the positions of the regions of separation close to the wall and maintaining a relative insensitivity in the inviscid free-stream field to the boundary conditions [19]. The compromise is achieved by switching and blending between the $k-\epsilon$ and $k-\omega$ turbulence models based on the distance from the wall. The transport equations, wall functions and model coefficients of the Menter SST turbulence model in *foam-extend* are described by Menter et al. (2003) [25].

3.4. The solver

dbnsTurbFoam is a transient, coupled density based solver in the framework of *foam-extend*. The solver computes the time accurate flow field, which is necessary for simulating the highly unsteady problems of shock-wave boundary layer interactions and flows within turbo-machinery passages. The high Reynolds numbers in transonic flows implies a turbulent flow field in the domain, and thus simulating the effects of turbulence on the mean fields is required. An explicit, low-storage, four-stage Runge Kutta time stepping scheme is incorporated with a choice of

Godunov type schemes to discretize the advective term. The advective scheme evaluates the inviscid flux at each cell face directly from the states left and right to the cell face[33]. The viscous fluxes are discretized by a standard set of schemes present in *foam-extend*.

3.5. The finite volume method of *foam-extend*

The 3-D Navier-Stokes equations are a system of non-linear partial differential equations . Analytical solutions for any arbitrary flow domain imposed with arbitrary initial and boundary conditions do not exist. Therefore it becomes necessary to use numerical methods on a discretized computational domain in order to obtain approximate solutions. Several numerical approaches exist for discretizing and handling the system of non-linear PDE's. The finite volume method (FVM) is widely used because the property of conservative discretization is implicitly respected, through the direct discretization of the integral form of the governing equations [13]. Therefore, several CFD solvers are based on the finite volume method, including *foam-extend*. The approximation process of the finite volume method involves substitution of the PDE's with a corresponding system of algebraic equations for obtaining the flow field at discrete locations in space and at discrete time intervals, in the case of transient problems [18]. *foam-extend* is based on the cell-centred finite volume method, enforces the evaluation of these algebraic equations at the discrete cell centers of each of the discretized volumes.

According to Jasak (1996), the finite volume method in *foam-extend* is characterized by the following features:

- All equations are solved in a fixed cartesian coordinate system which does not change in time.
- The control volumes can be of an arbitrary polyhedral shape, with a variable number of neighboring cells, thus representing a general unstructured mesh. In the thesis though, all flow calculations are carried out on a block-structured meshes.
- The flow variables are stored at the cell-centres of the polyhedral cells, generating a co-located mesh arrangement in the flow domain.
- In most of the solvers, the equations are solved in a segregated manner, with the inter-equation coupling being treated separately. The block-coupled approach used in the *dbns* solvers is a first in the *foam-extend* platform.
- Non-linear differential equations are linearized before the discretization.

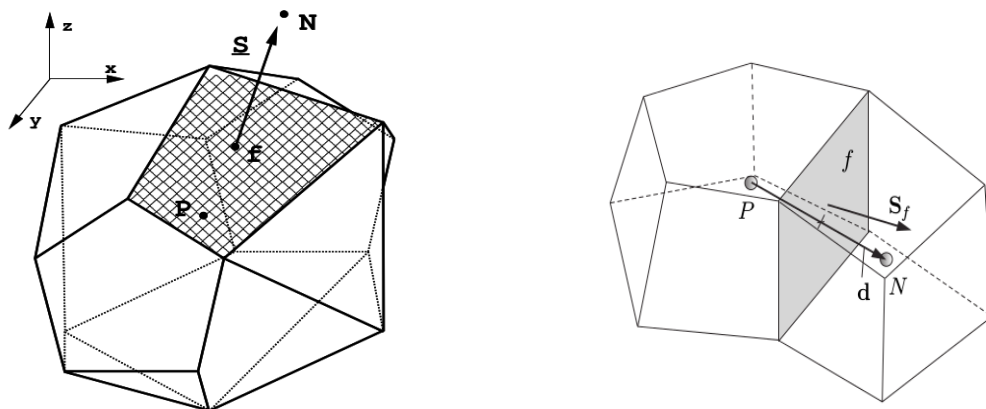


Figure 3.2 Generic polyhedral cell in *foam-extend* (left) and representation of 2 polyhedral cells in the mesh (right)

Source: OpenFOAM programmer's guide

The figures 3.2.1 and 3.2.2 represent typical polyhedral cells in a finite volume discretization in *foam-extend*. Figure 3.2 will be referenced for discussing the discretization procedures in the

section 3.10. In the Figure 3.2, S_f represents the face area vector, d represents the displacement vector between the 2 cell centers, while P and N represent the cell centers of the adjacent finite volumes.

3.6. Features of *dbnsTurbFoam*

dbnsTurbFoam is an explicit time marching solver which solves the approximate Riemann problem for reconstructing the advective flux at each cell face from the flow field states on each of the cell-centers.

In order to understand the discretization procedures described in later sections, the matrix representation of the governing equations in the conservative form are considered.

$$\frac{\partial \mathbf{U}}{\partial t} + \nabla \cdot \mathbf{F} - \nabla \cdot \mathbf{V} = 0 \quad (3.23)$$

$$\mathbf{U} = \begin{bmatrix} \rho \\ \rho \vec{U} \\ \rho E \end{bmatrix} \quad (3.24)$$

$$\mathbf{F} = \begin{bmatrix} \rho \vec{U} \\ \rho \vec{U} \vec{U} + p \mathbf{I} \\ \rho(E+p) \end{bmatrix} \quad (3.25)$$

$$\mathbf{V} = \begin{bmatrix} 0 \\ \sigma \\ \sigma \cdot \vec{U} - \vec{q} \end{bmatrix} \quad (3.26)$$

$$\mathbf{I} = \delta_{ij} \quad (3.27)$$

The solvers split the total convective flux at a cell face into the corresponding advective flux \mathbf{F} and viscous flux \mathbf{V} . \mathbf{I} in Equation (3.25) represents the identity matrix, as presented in Equation (3.27). All the other quantities have been defined in Chapter 2.

As mentioned, the advective flux at a cell face is obtained by solving an approximate Riemann problem. A choice of upwind and central advective schemes are at the user's disposal [33]. The viscous fluxes at the cell face are constructed by standard OpenFOAM discretization procedures in the *foam-extend* turbulence solver.

The solution algorithm is based on the time step restriction imposed by the CFL condition. The CFL condition is a necessary criterion for the stability of a simulation based on explicit time integration. For compressible flows, the CFL condition imposes a maximum restriction on the time step that can be chosen for the temporal advancement of the solution, based on the size of the computational cell and the maximum speed of a acoustic wave at the location. The formulation for the same in 1-D reads as given in Equation (3.28).

$$(Co = (U + c) \frac{\Delta t}{\Delta x}) \leq 1 \quad (3.28)$$

In Equation 3.28, Co represents the Courant number, U represents the fluid particle advection speed while c represents the local speed of sound. Therefore the courant number enforces the condition that information cannot propagate faster than the speed of the acoustic wave at each time iteration.

foam-extend computes the courant number based on the volumetric flux φ across the cell and the cell volume, instead of wave velocities and cell sizes, as given in Equation (3.29).

$$(Co = \frac{1}{2} \frac{\varphi}{V_{cell}}) \leq 1 \quad (3.29)$$

The courant number calculator built into *foam-extend* computes the time step dynamically, based

on the maximum allowable courant number in the flow domain, which is user defined. The formulation used does not seem to incorporate the local speed of sound in the courant number definition, which is an important aspect for future investigation.

3.7. Code architecture and flow chart

In Figure 3.3, the code architecture is presented in the form of a flow chart:

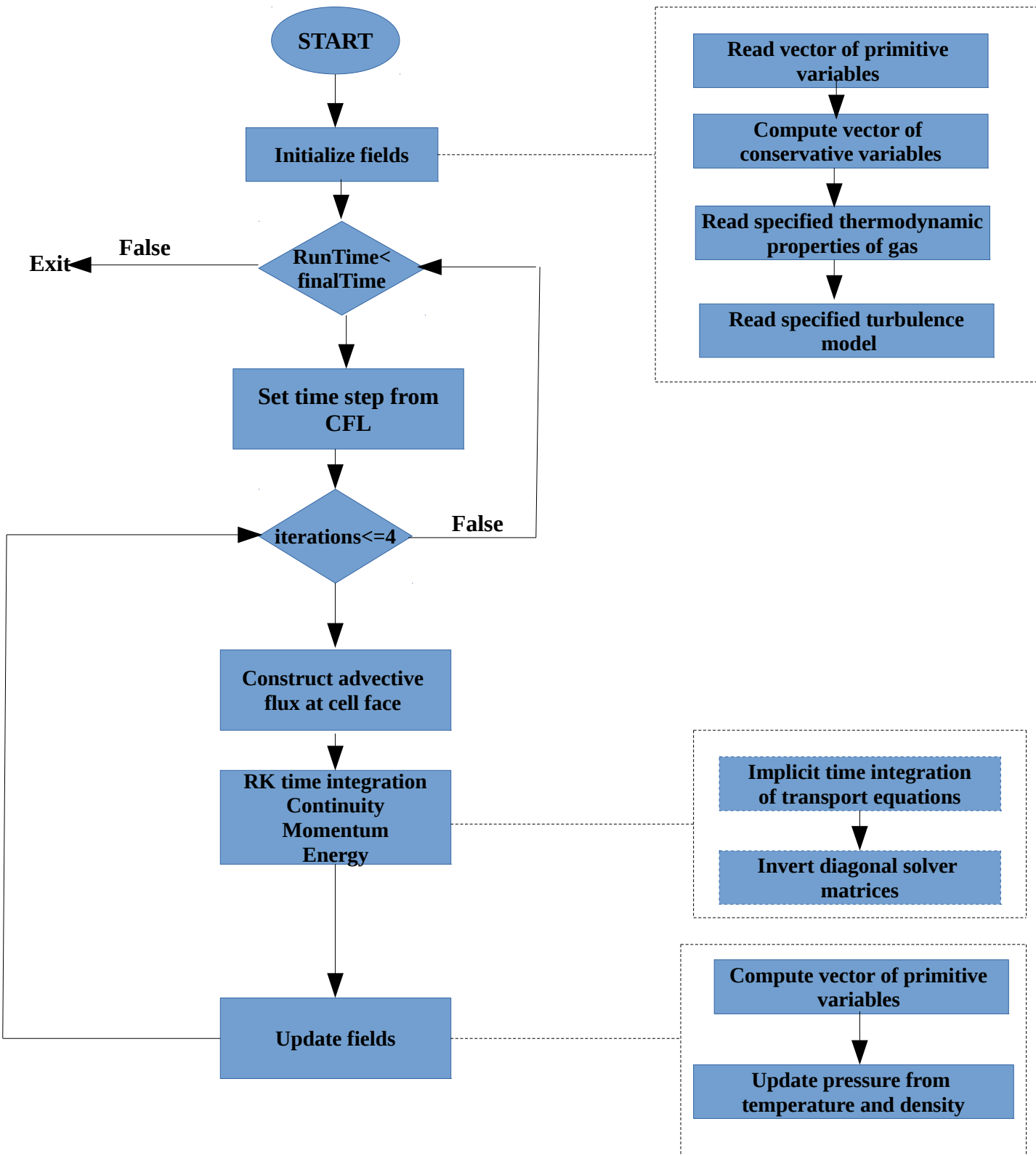


Figure 3.3 Solver flow chart described in the solver C++ file

The solver begins with an initialization of fields, which is a 4 step process, presented below, in the *createFields.H* header file:

- The vector of primitive flow variables as prescribed by the initial and boundary conditions is read by the solver.
- The vector of flow variables in the conservative form, represented as \mathbf{U} is computed.
- The specified thermodynamic properties of the medium are read by the solver.
- The specified turbulence model is read by the solver.

Following the initialization of fields in the domain, the subsequent computation of the flow field begins. The time step for the current time is chosen, based on the CFL condition. Following the selection of the time step, the solver algorithm commences with the construction of the advective fluxes at the cell faces, by the *rusanovFlux.H* header. Moreover, the viscous fluxes are computed by the *turbulence* function file. The linearized algebraic equations obtained due to the explicit time advancement of the NS equations over the stage, are represented as given in Equation 3.30. In Equation (3.30) A is a coefficient matrix, x is a vector of flow field values to be solved for and b is a vector of source terms.

$$[A][x]=[b] \quad (3.30)$$

The direct inversion of the governing equations is achieved by the diagonal solver in *foam-extend*. Meanwhile, the transport equations of turbulent quantities such as the turbulent kinetic energy and the turbulence frequency are advanced temporally via the Euler implicit time integration. Upon discretization of the terms of the transport equations, the algebraic equations are solved using iterative techniques.

The final steps at the end of a time step involves updating the vector of primitive variables in the domain. The pressure at the end of the time step is then updated from the density ρ and temperature T from the equation of state.

3.8. Equation representation in foam-extend-3.2

The finite volume discretization of each of the terms of the governing equations is carried out by integrating them over a cell volume V . All the spatial derivative terms are then converted from volume integrals to surface integrals as described by the Gauss's theorem.

$$\int_V \nabla * \varphi dV = \int_S \mathbf{dS} * \varphi \quad (3.31)$$

Here the '*' represents any kind of tensor product, namely inner, outer and cross products. Volume and surface integrals are then linearized using appropriate schemes corresponding to each of the tensor products. There are 2 types of discretizations, namely implicit discretization and explicit discretization. The *foam-extend* solver has two classes to represent the different discretizations. The functions of class *fvm* calculate the implicit derivatives of a term and return a coefficient matrix [12]. On the other hand, the functions of class *fvc* compute the explicit derivatives of a term from current cell values and return field values. The governing equations as represented in the solver are given in Appendix A. The schemes discretizing the different terms including the advective term, divergence terms and laplacian terms are discussed further in section 3.9.

3.9. Spatial Discretization

3.9.1. Advective term discretization-Rusanov Flux

The Rusanov flux scheme, also known as the Local Lax-Friedrichs scheme is a central scheme used for the discretization of the advective term of the NS equations. The scheme was chosen due to its higher order of accuracy as compared to the first order upwind schemes implemented in the solver. Moreover, central schemes are suitable for conducting aeroacoustic simulations since no specific direction for the propagation of information is assumed while discretizing the advective term.

In approximate Riemann solvers, constructing the advective flux is a local procedure at the interface between two cells, with a different value specified at the cell-centers on either side. In

order to construct the flux from the hyperbolic governing equations, the equations are to be solved with a step function across the cell face specifying the initial conditions.

Equation (3.32), is considered for further discussion on the advective scheme. It is to be noted that the equation is in quasi-linear form, for the sake of simplicity.

$$\frac{\partial \mathbf{U}}{\partial t} + A \frac{\partial \mathbf{U}}{\partial x} = 0 \quad (3.32)$$

$$\mathbf{U}(0, x) = \begin{cases} U_L, & x < 0 \\ U_R, & x \geq 0 \end{cases} \quad (3.33)$$

It can be demonstrated that the 1-D solution to the Riemann problem with constant coefficients reduces to the upwind flux. Therefore, solving the Riemann problem for hyperbolic systems dominated by shocks and other flow discontinuities is in theory the most stable method. The method has its disadvantages though, as it can be computationally expensive to solve the Riemann problem for non-linear equations.

The Rusanov flux, also called the Local Lax-Friedrichs flux aims at combining the higher order of accuracy of the central schemes with the stability of the generalized upwind flux. The idea is to consider a centered flux with the addition of an appropriate amount of numerical diffusion locally. The expression presented below for the flux $F_{i+\frac{1}{2}}$ will be considered for further

discussion:

$$F_{i+\frac{1}{2}} = \frac{1}{2} [A(\mathbf{U}_i + \mathbf{U}_{i+1}) - \alpha_{i+\frac{1}{2}} (\mathbf{U}_{i+1} - \mathbf{U}_i)] \quad (3.34)$$

$$\alpha_{i+\frac{1}{2}} = \max(|(\lambda_A)|) \quad (3.35)$$

In the Equation (3.35), λ_A are the eigen values of matrix A. Choosing the viscosity parameter as the largest eigen value, and hence the largest local wave speed $\alpha_{i+\frac{1}{2}}$ ensures stability. A

major advantage over the highly dissipative Lax-Friedrichs scheme corresponds to choosing the largest local wave speeds. Thus, at locations in the domain with small gradients, low numerical viscosity is introduced.

3.9.2. Flux limiter- The Barth-Jespersen's limiter

The reconstruction process in the finite-volume method involves the projection of the updated flow values at a cell-center onto a polynomial function across the entire computational cell. The reconstruction process is used in order to improve the representation of a flow value within the computational cell. The use of higher order interpolating polynomial functions introduce jumps in state variables across the shared cell face of adjacent cell faces, compromising the monotonicity of the property values [6]. This further results in the introduction of spurious numerical oscillations in the solution, possibly compromising the stability of the computations.

Slope limiters are used to limit the slope of the interpolating functions near flow discontinuities, to computationally realizable values. This ensures the monotonicity of the property values across cell faces. The present thesis employs the use of the basic Barth-Jespersen limiter, which was developed for a generic unstructured mesh. Literature [6] reports the limiter maintains monotonicity, but results in delayed convergence to steady state. In this context, the Venkatakrishnan limiter [24] could be explored in the future when performing steady state simulations.

The Equations (3.36)-(3.41) describe the formulation representing the Barth-Jespersen limiter. The variable $u(r, t)$ represents an arbitrary primitive variable anywhere within the cell.

Equation (3.36) represents the computation of the reconstructed primitive variable across the computational domain. Φ represents the limiter value, which is a constant in the computational cell along with the gradient within the cell. The term $u(r_c, t)$ is the value of the primitive variable at the cell-center.

$$u(r, t) = u(r_c, t) + \Phi \nabla u(r_c, t) \cdot (\vec{r} - \vec{r}_c) \quad (3.36)$$

$$0 \leq \Phi \leq 1 \quad (3.41)$$

Φ of a certain computational cell in the Barth-Jespersen is computed based on equation described by Bayyuk (2008) [6].

$$\Phi(c_i) = \min_j (\tilde{\Phi}(c_i, c_j)) \quad (3.37)$$

The c_j is used to represent set of cells neighboring the concerned cell c_i that are utilized in order to compute the value of the limiter within c_i .

$$\tilde{\Phi}(c_i, c_j) = \begin{cases} \frac{\Delta u_{c_i}^{\max}}{\Delta u_r}, & \text{if } \Delta u_r > \Delta u_{c_i}^{\max} \\ \frac{\Delta u_{c_i}^{\min}}{\Delta u_r}, & \text{if } \Delta u_r < \Delta u_{c_i}^{\min} \\ 1, & \text{if } \Delta u_{c_i}^{\min} < \Delta u_r < \Delta u_{c_i}^{\max} \end{cases} \quad (3.38)$$

$$\Delta u_{c_i}^{\max} = \max_j (u_{c_j} - u_{c_i}) \quad (3.39)$$

$$\Delta u_{c_i}^{\min} = \min_j (u_{c_j} - u_{c_i}) \quad (3.40)$$

$$\Delta u_r = \nabla u_{c_i} \cdot (\vec{r}_{f_j} - \vec{r}_{c_i}) \quad (3.41)$$

Δu_r refers to the difference in values of the reconstructed primitive variable at the shared face between cells i and j . The formulation ensures that the reconstructed value at the cell face is between the bounds of the cell-center values of the set of neighboring cells subscripted 'j'.

3.9.3. Viscous terms

- **Divergence schemes**

All the divergence terms φ of the solver are integrated over the control volume of Figure 3.2 and converted to a surface integral based on Gauss's theorem.

$$\int_V \nabla \cdot (\varphi) dV = \int_{\bar{S}} d\vec{S} \cdot \varphi \quad (3.42)$$

$$\int_{\bar{S}} d\vec{S} \cdot \varphi = \sum_f \vec{S}_f \cdot (\varphi_f) \quad (3.43)$$

A second order, central differencing scheme has been chosen to construct the face flux φ_f from the state values at the cell-centers.

$$\varphi_f = f_x \varphi_P + (1-f_x) \varphi_N \quad (3.44)$$

$$f_x = \frac{\bar{fN}}{\bar{PN}} \quad (3.45)$$

Here, \bar{fN} and \bar{PN} denote the distance from the shared face to the cell-center N and the distance between the cell-centers respectively.

- **Laplacian schemes**

A similar central scheme is applied to discretize the laplacian terms φ , upon conversion to a surface integral, based on the Gauss's theorem.

$$\int_V \nabla \cdot (\Gamma \nabla \varphi) dV = \int_{\bar{S}} d\vec{S} \cdot (\Gamma \nabla \varphi) \quad (3.46)$$

$$\int_{\bar{S}} d\vec{S} \cdot (\Gamma \nabla \varphi) = \sum_f \Gamma_f \vec{S}_f \cdot (\nabla \varphi_f) \quad (3.47)$$

$$\vec{S}_f \cdot (\nabla \varphi_f) = |\vec{S}_f| \frac{\varphi_N - \varphi_P}{|\vec{d}|} \quad (3.48)$$

The gradient term is discretized by the central scheme when the length vector \vec{d} is perpendicular to the face \vec{S}_f . This is exactly true for orthogonal meshes. Otherwise a fix is implemented for small non-orthogonalities [12]. It is therefore recommended to avoid large non-orthogonalities in the computational mesh.

3.10. Temporal Discretization

A low storage, Runge-Kutta 4-stage method is employed for the temporal discretization. The discretization is of second order accuracy in time and is optimized for first and second order upwind spatial discretizations. In the future, it would be interesting to look for discretization schemes optimized for central spatial discretizations.

Considering the Equations (3.49)-(3.56), a discussion of the temporal discretization is advanced. Equation (3.49), a set of coupled ordinary differential equations are obtained with the application of the method of lines to the governing differential equations [5].

$$\frac{d}{dt}(\Omega_I \mathbf{I} \mathbf{U}) = -\vec{R} \quad (3.49)$$

\vec{R} represents the residual vector, which represents the discretized spatial term, a non-linear function of the conservative state variables \mathbf{U} . *dbnsTurbFoam* employs the class of explicit multi-stage schemes employed first by Jameson, for the temporal discretization of Equation (3.49) [5].

Equations (3.50)-(3.55) describe the algorithm between the n^{th} and $(n+1)^{th}$ time iterations.

$$\mathbf{U}^{(0)} = \mathbf{U}^n \quad (3.50)$$

$$\mathbf{U}^{(1)} = \mathbf{U}^{(0)} - \beta_1 \frac{\Delta t}{\Omega_I} \vec{R}_I^{(0)} \quad (3.51)$$

$$\mathbf{U}^{(2)} = \mathbf{U}^{(0)} - \beta_2 \frac{\Delta t}{\Omega_I} \vec{R}_I^{(1)} \quad (3.52)$$

$$\mathbf{U}^{(3)} = \mathbf{U}^{(0)} - \beta_3 \frac{\Delta t}{\Omega_I} \vec{R}_I^{(2)} \quad (3.53)$$

$$\mathbf{U}^{(4)} = \mathbf{U}^{(0)} - \beta_4 \frac{\Delta t}{\Omega_I} \vec{R}_I^{(3)} \quad (3.54)$$

$$\mathbf{U}^{(n+1)} = \mathbf{U}^{(4)} \quad (3.55)$$

The scheme only requires the storage of the zeroth solution and the most recent update of the residual. Therefore there is considerable reduction in memory requirements over the standard RK-4 discretization. The vector of scalar coefficients are provided in Equation (3.56).

$$\boldsymbol{\beta} = \begin{bmatrix} 0.11 \\ 0.2766 \\ 0.5 \\ 1 \end{bmatrix} \quad (3.56)$$

4 RESULTS AND DISCUSSIONS

The chapter aims at compiling the sequential, step by step validation of the *dbnsTurbFoam* solver. The validation aims at demonstrating the suitability of the solver for simulating the transonic flow within the HPT-NGV cascade introduced in Chapter 2.

4.1. Sod's shock tube

As described in an earlier chapter, the computational domain is discretized into 800 cells for a domain extending along $0 \leq x \leq 1$. The time step is chosen as $\Delta t = 0.25 \Delta x$. The conditions for pressure, density and velocity at a time right after the diaphragm is removed are presented in Figure 4.1.

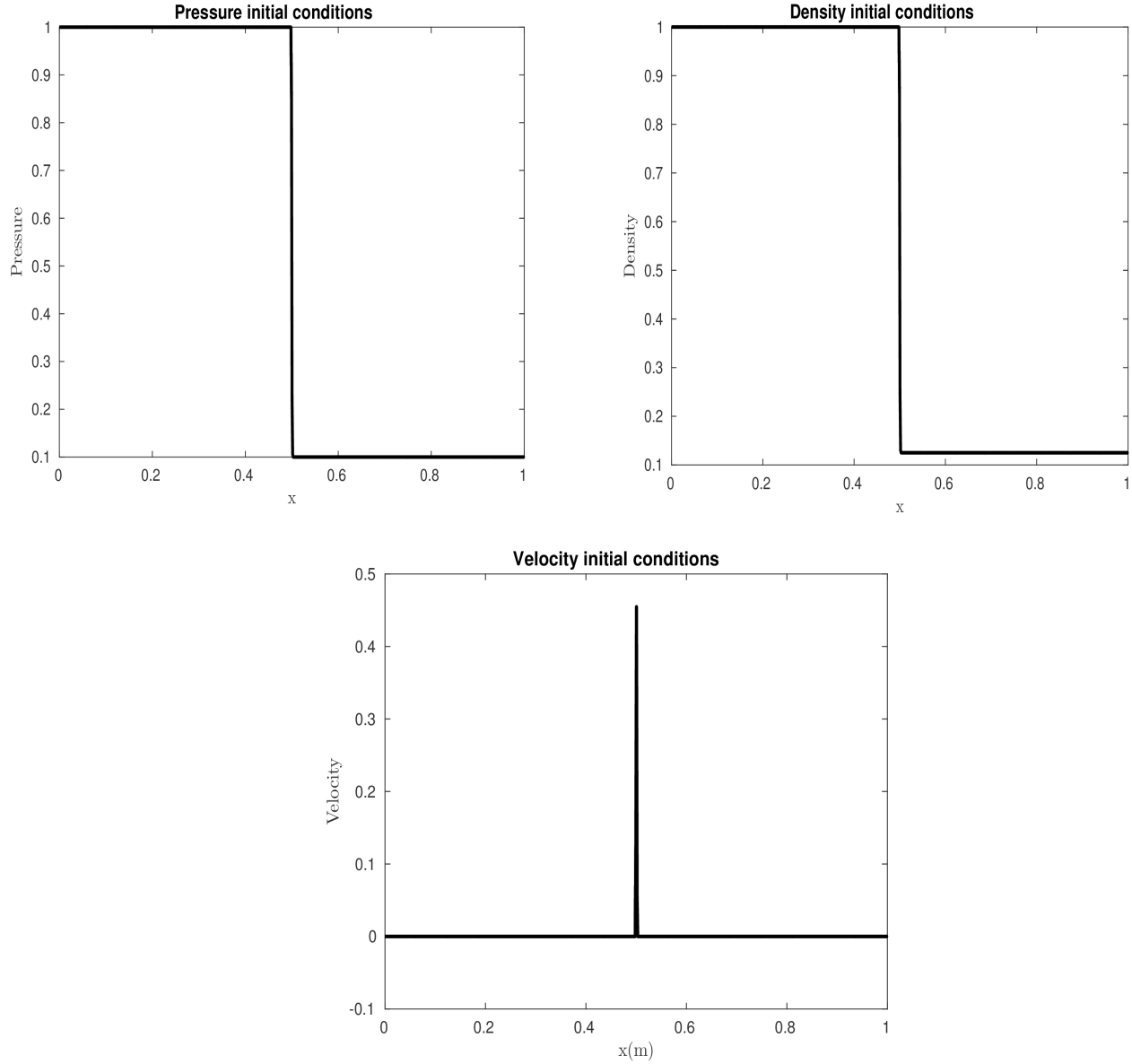


Figure 4.1. Conditions for (a) Pressure (b) Density (c) Velocity in the domain just after the diaphragm is removed

Figures 4.2 and 4.3 represent the simulation results for times 0.1 and 0.2 respectively, plotted against the analytical results. The plot of density against the non-dimensionalized distance captures the 3 distinct traveling wave motions, corresponding to:

- The coalesced compression wave (shock wave) moving towards the right, into the driven gas compartment.
- The family of rarefaction waves moving towards the left, the family of waves spreading as they propagate.
- The contact discontinuity moving towards the right, is a surface dividing the driver and driven gases respectively.

Since the contact discontinuity is a slip surface, it is impossible to observe in plots of pressure and particle velocity, and one must instead look at the plots for density, where it can be discerned.

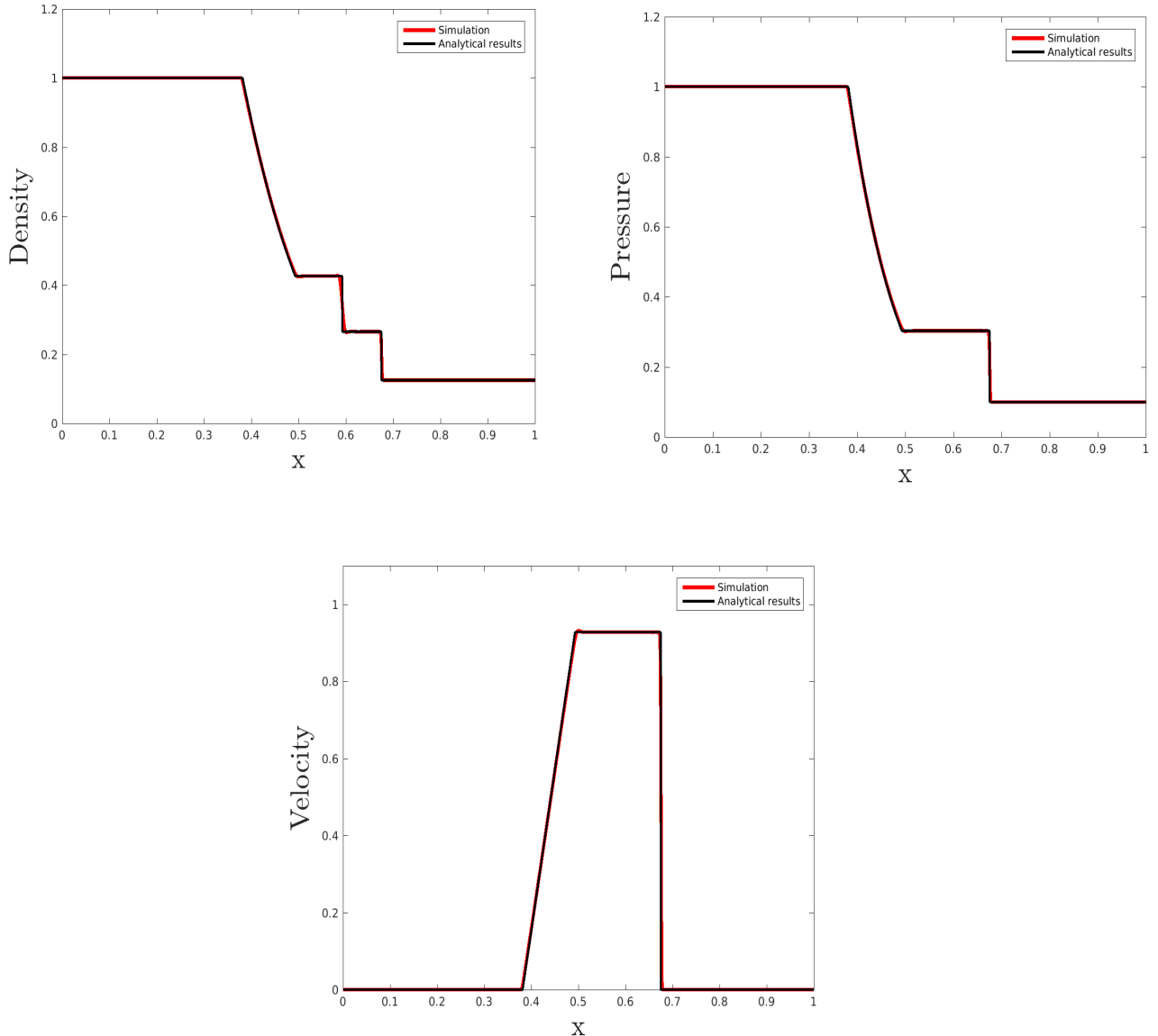


Figure 4.2. Plots for Density, pressure & particle velocity at time $t=0.10$

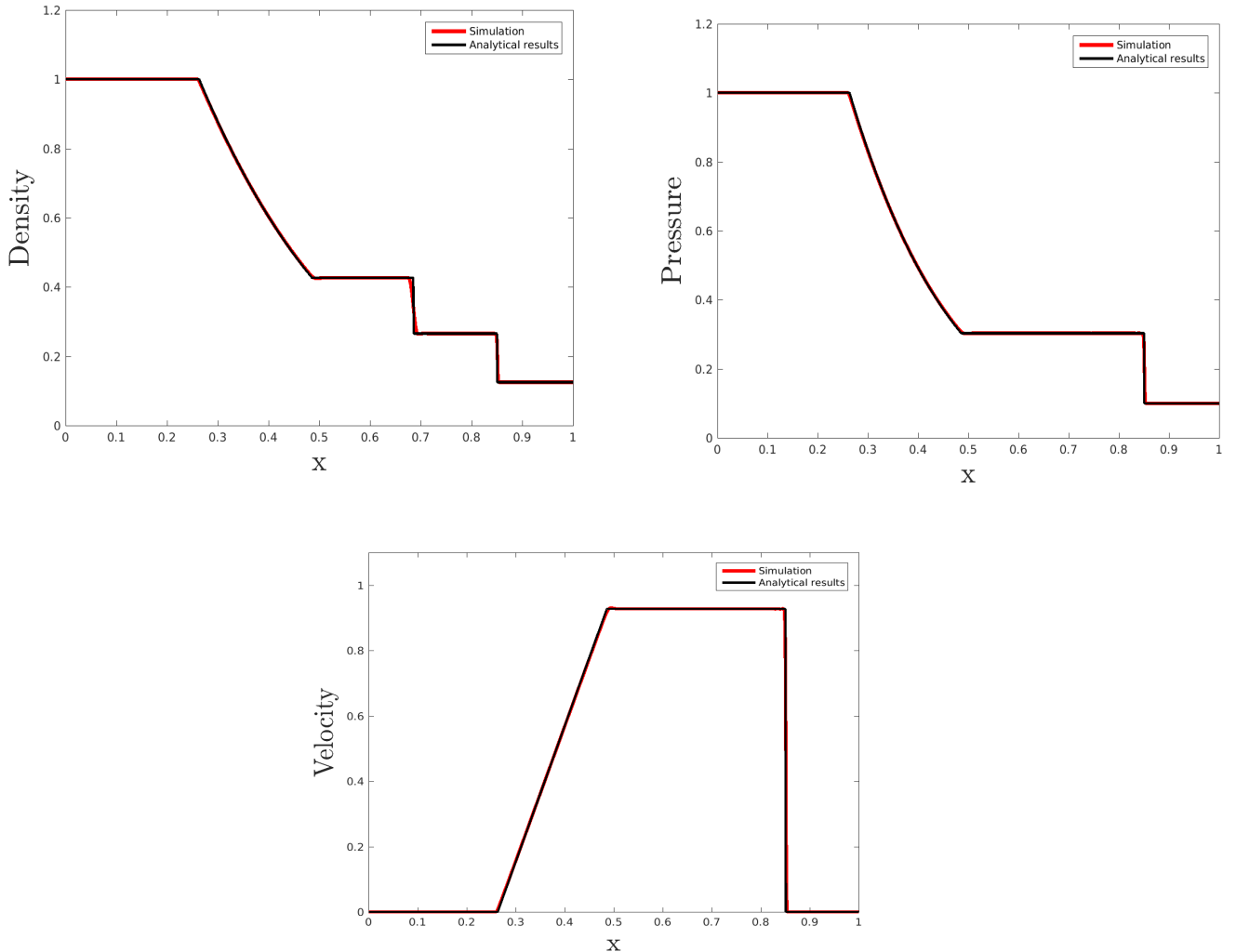


Figure 4.3. Plots for Density, pressure & particle velocity at time $t=0.20$

Figures 4.1-4.3 represent the plots for flow variables for different time snapshots. The flow in the shock tube is simulated upto a non-dimensional time $t=0.22$, roughly corresponding to the time taken for the traveling shock to reach the right wall of the tube.

As evidenced from the Figures 4.1-4.3, the simulated results are in close agreement with the analytical results with respect to:

- Traveling wave speeds.
- Negligible/non-existent Gibbs oscillations.
- Low numerical diffusion, resulting in a good resolution of the shock.

The contact discontinuity is more damped, and not as sharply resolved compared to the shock wave.

4.2. ONERA S8 Transonic channel

4.2.1. Inviscid flow results

2-D inviscid flow computations were performed in the *dbnsFoam* solver. These simulations were performed in order to tune the outlet pressure to for placing the shock-wave in approximately the same location as in experiment. Besides, first insights into the validity of the solvers were provided by applying the Rankine-Hugoniot jump conditions across the normal shock. The Rankine-Hugoniot jump condition describes a relation that must be respected across a discontinuous/abrupt change in a conserved quantity of the flow. The jump condition across the normal shock is expressed in Equation 4.1. The flow quantities with the subscript 2 indicate

stations downstream to the shock, while the flow quantities with subscript 1 indicate stations upstream to the shock. The relation is expressed as a ratio of flow speeds upstream and downstream to the normal shock wave. M_1 represents the upstream Mach number, while γ represents the ratio of specific heats of the gas.

$$\frac{u_2}{u_1} = \frac{(\gamma - 1)M_1^2 + 2}{(\gamma + 1)M_1^2} \Rightarrow u_2 = u_1 \left(\frac{(\gamma - 1)M_1^2 + 2}{(\gamma + 1)M_1^2} \right) \quad (4.1)$$

The inviscid flow simulation was performed with the time step specified by a maximum allowable courant number of 0.5 set in the flow domain. The simulation was carried out till a stationary normal shock placed downstream to the throat of the wind tunnel was obtained. Figure 4.4 illustrates a surface plot for Mach number upon the solver convergence with a pressure of 0.60 Bar set at the outlet of the computational domain.

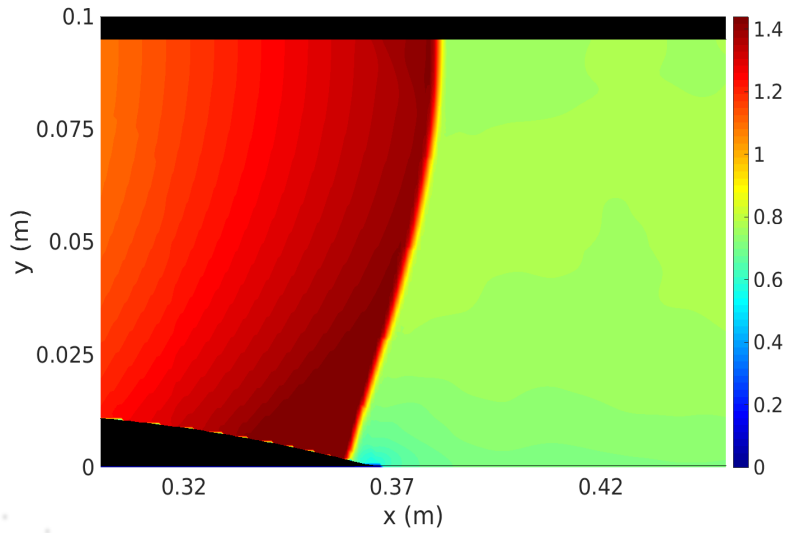


Figure 4.4 Surface plot for Mach number at the last time step

An application of the jump condition along a line across the normal shock yields a downstream velocity within 5% of the value obtained from simulation. Due to the absence of the boundary layer in the inviscid flow computations, the characteristic splitting of the normal shock to the lambda pattern was not observed. A viscous flow computation was therefore required to simulate the lambda shock.

4.2.2. Unsteady RANS results for the viscous case

The use of the explicit multi-stage Runge Kutta scheme for time integration resolves some of the low frequency unsteadiness associated with the shock wave-turbulent boundary layer interaction. Therefore, the results of the URANS simulations allow for the study of the mean fields and provides first insights into the dynamics of the interaction process. A standard process for verification and validation is applied to the simulation results as is the case with several Computational Fluid Dynamics studies. The verification and validation of the results involve proving the spatial convergence of the results.

Mean fields

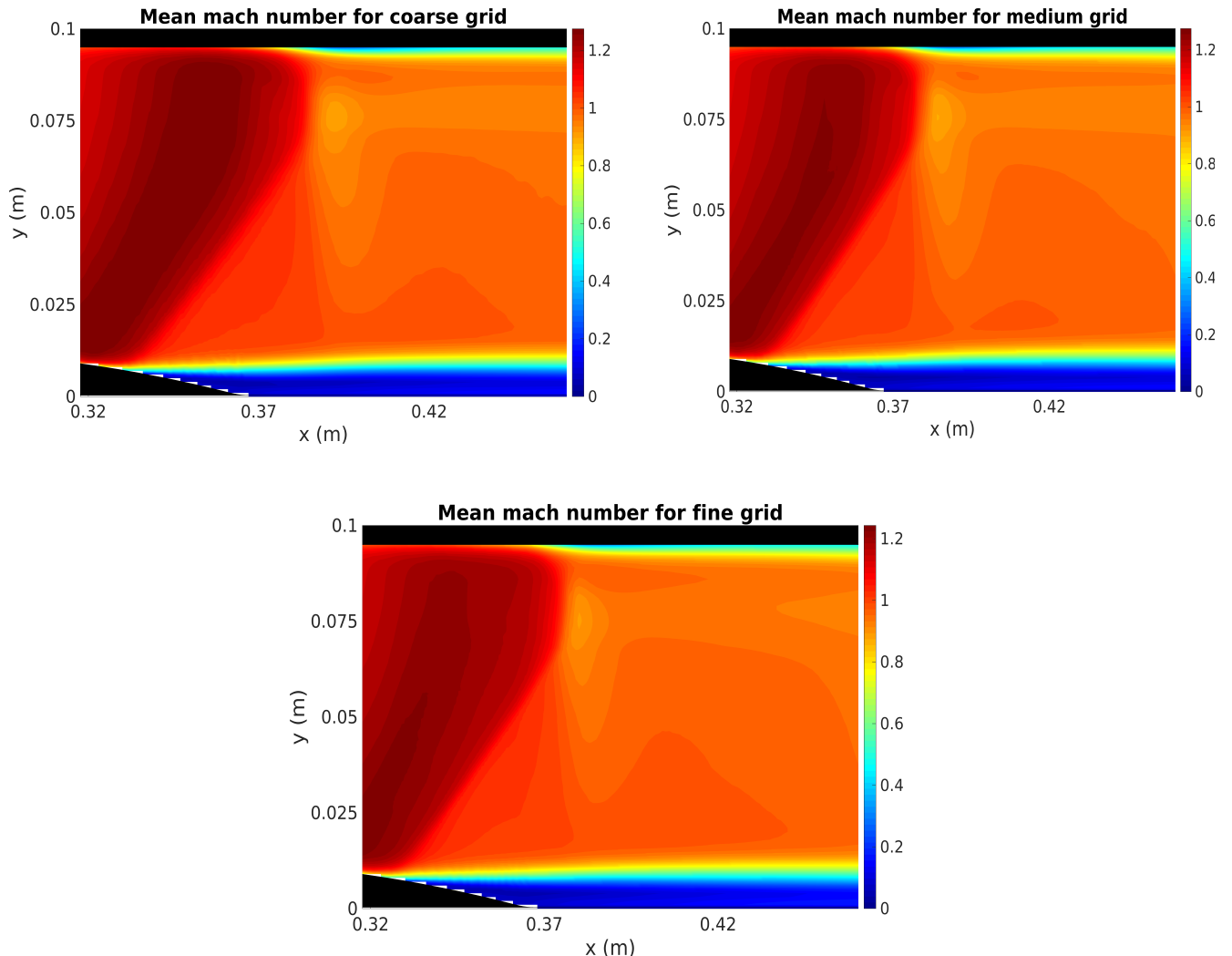


Figure 4.5. Surface plots for the time-averaged mach number for the 3 different grids

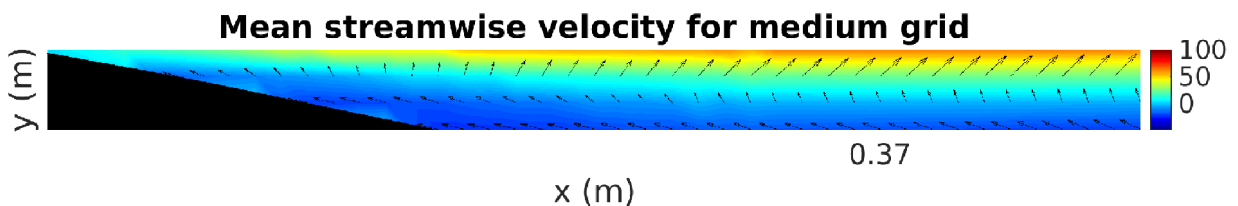


Figure 4.6. The extended layer of separation induced by the shock

The lambda shock pattern characteristic of the shock induced separation was obtained downstream to the throat of the channel. An extended region of separation downstream to the oblique leg C_1 (refer to figure 2.2) was obtained as shown in Figure 4.6.

The mean fields presented in Figure 4.5 have been computed by time averaging the fluid fields over a million iterations, or 20 normal shock oscillations. The flow fields were sampled over an interval of 10^{-4} seconds, discretizing the computed shock oscillation frequency of 134 Hz. The Equation 4.2 was used to compute the mean fields, with the integral being replaced by a summation over the discrete time intervals.

$$\bar{U}(\mathbf{x}) = \lim_{T \rightarrow \infty} \frac{1}{T} \int_{t_0}^{t_0+T} U(\mathbf{x}, t') dt' \quad (4.2)$$

The Rankine-Hugoniot jump conditions applied to the normal leg C_3 of the lambda shock are respected within 5 %.

Grid convergence and comparison with experiment

The ONERA report [8] contains experimental data obtained in the inviscid region and in the viscous layer of the channel. Experimental data correspond to interferometry and velocimetry measurements [8]. The present work compares the simulation results on three different grids along with the experimental data in the inviscid layer. Following this, the simulation results for the medium mesh are compared against the experimental data in the viscous layer.

Inviscid layer

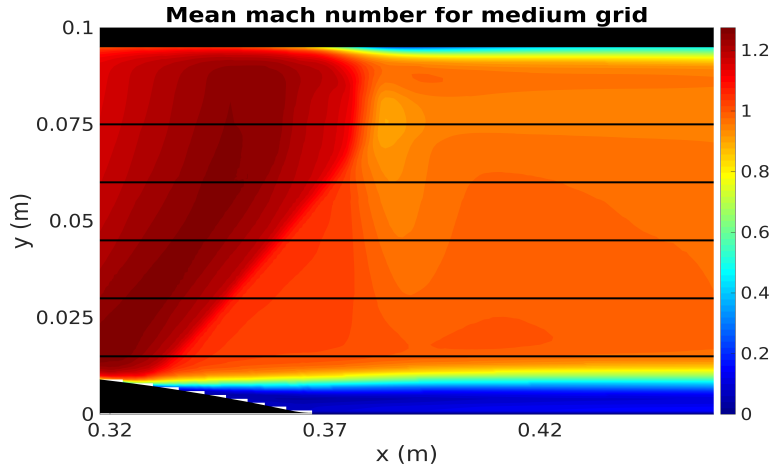


Figure 4.7. Lines for comparison with experiment

Five different lines cutting across the inviscid layer were chosen for the grid convergence study and comparison against experimental results as shown in Figure 4.7.

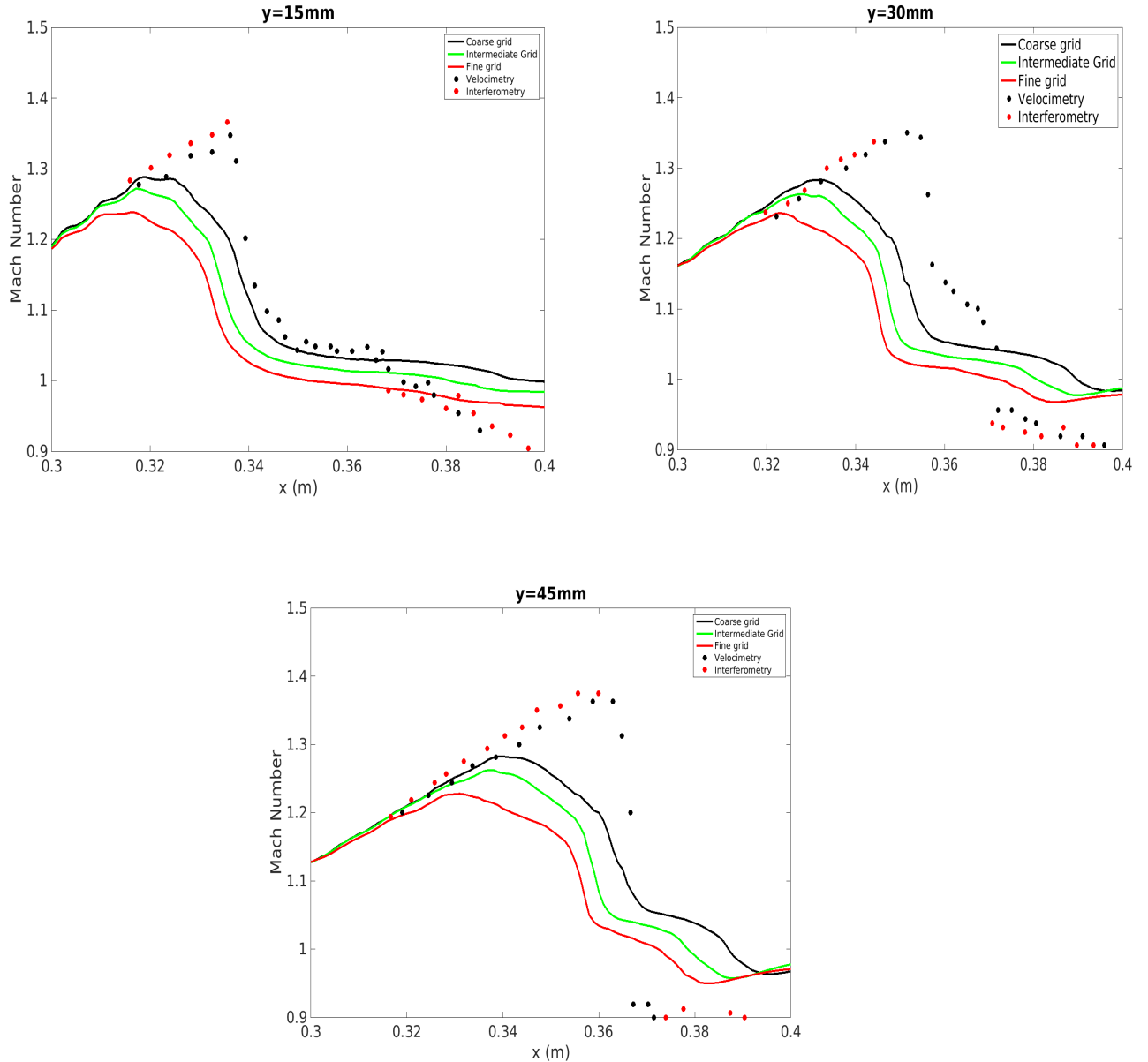


Figure 4.8. Mach number plotted across the oblique legs for three different grids and compared against experimental data

In Figure 4.8, the plots correspond to the mach number variation across the oblique legs C_1 and C_2 of the simulated lambda shock. This can be seen from the two distinct dips in the mach number variation. On the other hand, the first two plots correspond to the mach number variation across the oblique legs of the experimental lambda shock. The experimental position of the triple point (point where the oblique legs meet) is at a position of 45 mm from the bottom wall, while the position predicted by simulation is approximately 60 mm from the bottom wall.

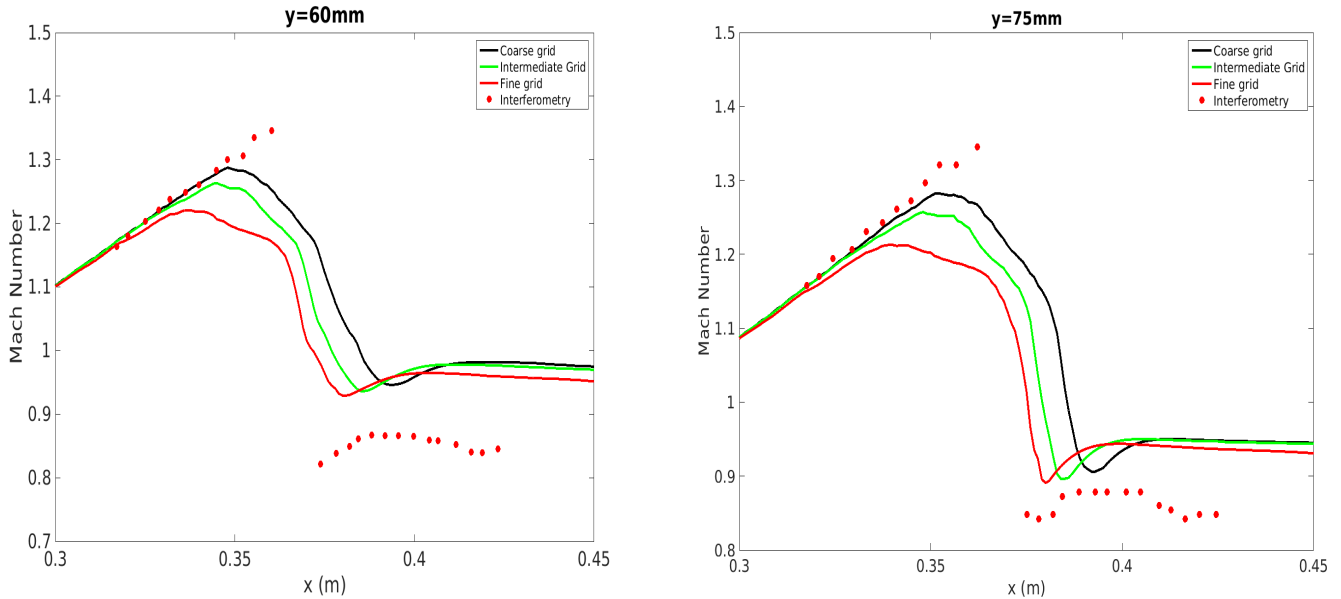


Figure 4.9. Mach number plotted across the normal leg for three different grids and compared against experimental data

A single steep drop in the Figures 4.9 for the experimental stream-wise mach number distribution represents the mach number variation across the normal leg C_3 of the lambda shock. On the other hand, Figure 4.9 (b) represents the mach number variation across the normal leg as predicted by the simulation.

The grid convergence study was inconclusive in the inviscid layer for the following reasons:

- **The time averaging of the field data has resulted in significantly smearing the three legs of the lambda shock.** This can be seen in the smooth stream-wise variation of the mach number across the normal shock in Figure 4.9. As remarked earlier, the transonic flow in the channel near the shock is quasi-periodic. This is apparent in the low frequency motion of the lambda shock structure.

In order to characterize the dominant frequency of oscillation of the lambda shock, the pressure at a point near the normal leg is recorded. The Power Spectral Density (PSD) of the pressure signal $p(t)$ is computed and plotted against the spectra of frequencies. The PSD is used to determine the energy content distribution of a signal in the frequency domain. In Figure 4.10, the amplitude of the power spectral density is plotted against the non-dimensional frequency, the Strouhal number. The mathematical definition of the Strouhal number is given by Equation (4.3).

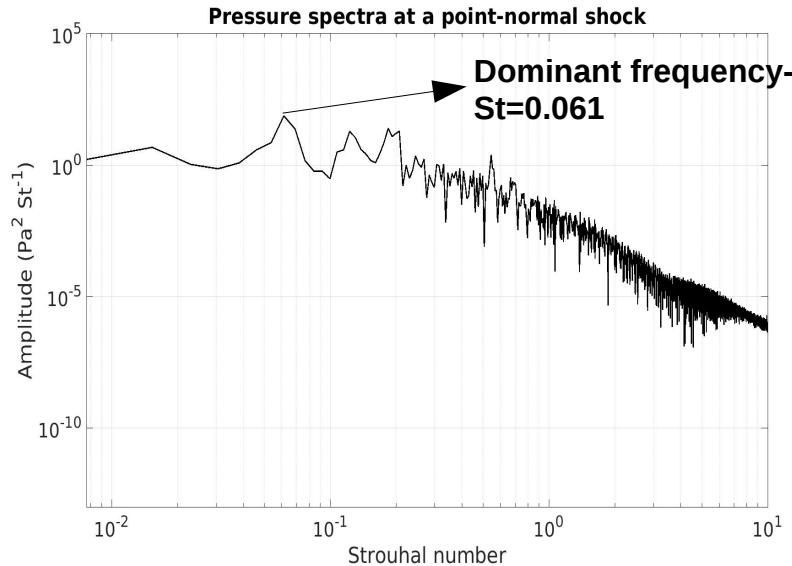


Figure 4.10. Pressure spectra for the fine mesh at a point near the mean position of the normal leg

$$St = \frac{fL}{U} \quad (4.3)$$

The Strouhal number is useful in characterizing oscillating flow mechanisms such as vortex shedding. In Equation (4.3), f is the characteristic frequency of the flow, L is the characteristic length scale of the flow and U is the free-stream flow speed. Physically, the Strouhal number is the ratio of the convective time scale to the time scale associated with the flow oscillation. From Figure 4.10, the dominant frequency containing the highest power content in the signal can be identified at a Strouhal number of 0.061. Thus, the lambda shock oscillates mainly at a frequency of $St=0.061$. It is therefore recommended to conduct a phase averaging of the flow field, instead of time averaging as described in Chapter 5.

- **The lambda shock structure predicted in simulation by all three grids is located upstream as compared to the experimental position.** A further reduction in the channel outlet pressure places the lambda shock far too downstream.
- **The locations of the triple point predicted by the simulation and experiment are different.**
- **Grid convergence has not been attained,** and this could be because of the use of wall functions. An accurate resolution of the viscous sub-layer might be necessary for future work, as the position of the lambda shock is sensitive to the point and extent of flow separation [9].

Comparison in viscous layer with experimental data

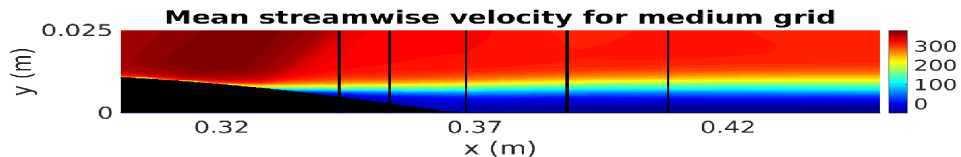
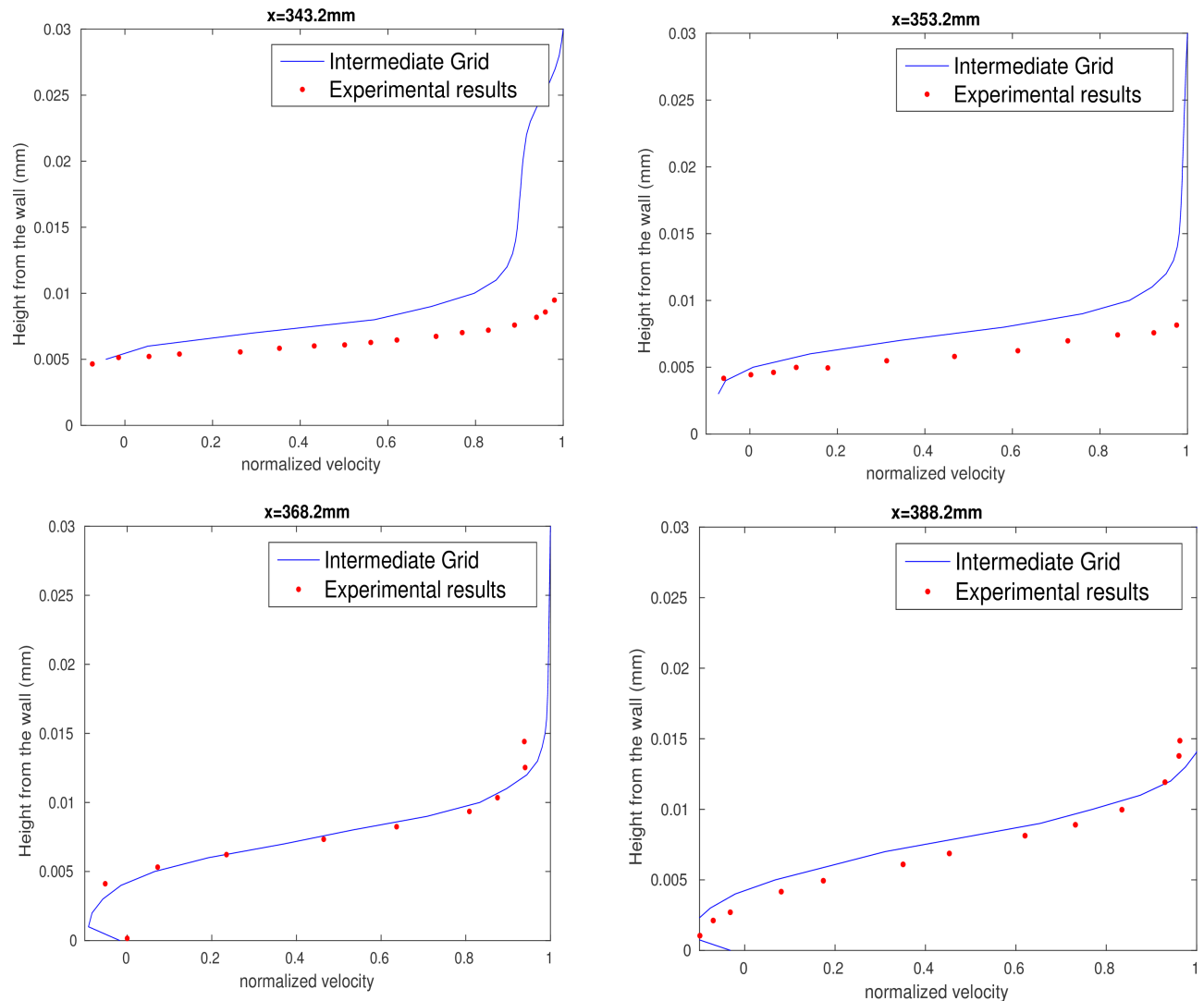


Figure 4.11. Experimental lines for data comparison



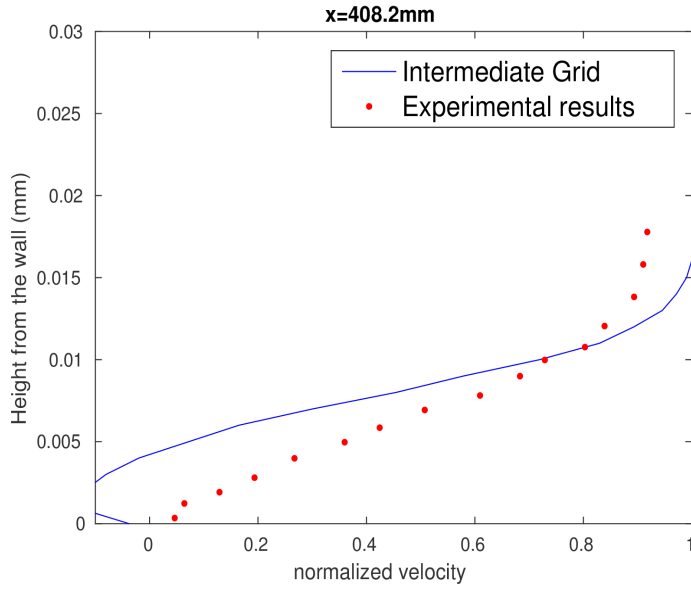


Figure 4.12. Comparison with experimental results in the dissipative layer

The plots shown in the Figure 4.12 correspond to the stream-wise velocity distribution plotted against the wall-normal distance. The velocity distribution has been normalized against the stream-wise velocity at the edge of the boundary layer, in order to show the wall normal extent of the dissipative layer in either case. Since grid convergence has not been attained, it is difficult to draw any conclusions regarding the comparison with experiments in the viscous layer. In general, a poor agreement between the results was noted at the point of flow separation, with experiments predicting a higher gradient of the stream-wise velocity in the wall-normal direction. Moreover, the stream-wise extent of the separated bubble is much higher in simulation than in experiment. A more in-depth analysis of the results are interesting for future work.

4.3. Linear cascade of Nozzle Guide Vanes

Compressible URANS simulations were performed for simulating the flow field within the cascade of nozzle guide vanes. The simulation has a low maximum allowable courant number setting of 0.1, based on stability restrictions. Statistical convergence was obtained after running the simulation for a million iterations. From figure 4.13 (b), it can be observed that the periodicity of the flow is well respected. This is evident in the trailing edge vane wakes of the upper vanes that are captured. Far downstream to the cascade, the vane wakes are less resolved due to numerical diffusion introduced from grid stretching. The simulation required 61440 core-hours to reach convergence. The high computational cost of performing the simulation has been attributed to the *cyclicGgi* boundary condition introduced in Chapter 2. The Figures 4.13-4.14 illustrate the flow field at a particular time snapshot once statistical convergence is attained.

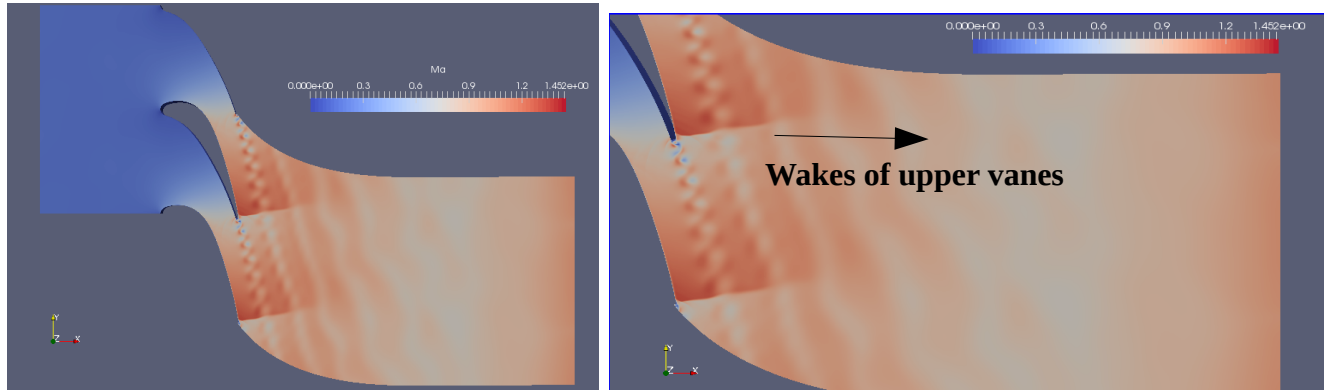


Figure 4.13. Transient results at $t=0.00625$ seconds (1 million iterations)

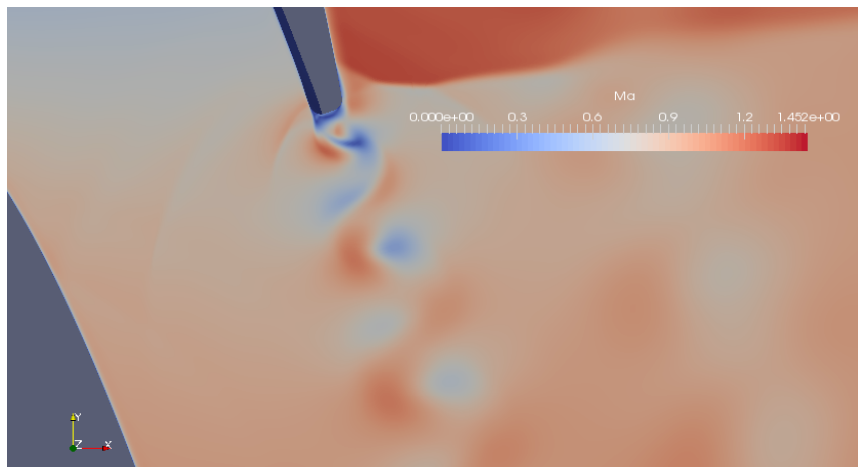


Figure 4.14. Close-up of the vortex shedding at the trailing edge of the central vane

The passages of the linear cascade behave like a converging-diverging nozzle, accelerating the incoming subsonic air to supersonic speeds beyond the throat of the passage. A weak trailing edge shock appears at approximately 90% of C_{ax} due to the imposed static pressure at the exit of the cascade. The shock was observed to oscillate on the vane surface due to its interaction with the trailing edge wake of the upper vane. A strong reduction of the vorticity in the wake coupled to a reduction in shock intensity was observed to occur across the shock-wake interaction region. The physical mechanism for the shock-wake interactions are interesting for future study. Figure 4.14 shows a close up of the trailing edge of the central vane, capturing the vortex shedding that is occurring.

4.3.1 Mean Fields

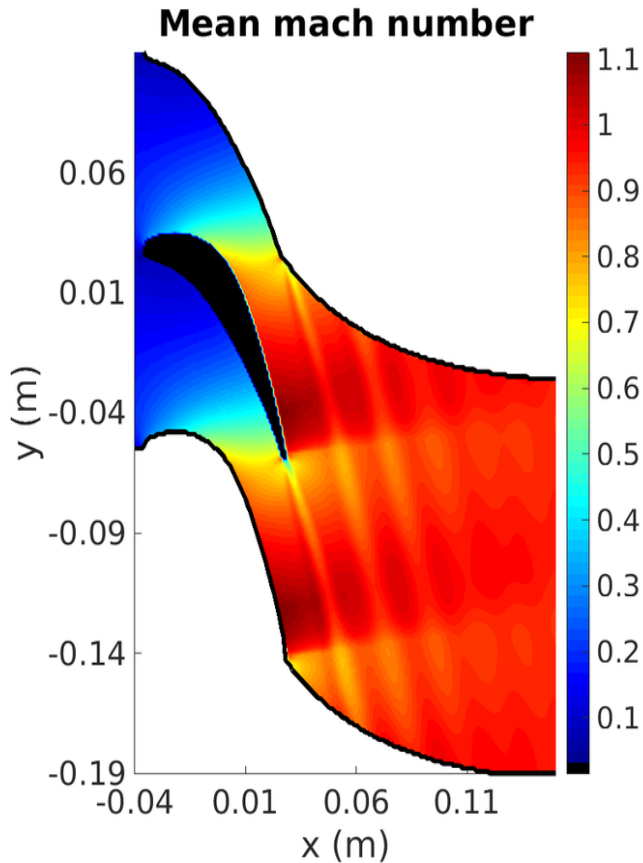


Figure 4.15. Mean fields for Mach number

The time averaged fields were computed over 100 trailing edge vortex shedding cycles. The flow fields were sampled every 10^{-7} seconds, in order to discretize the vortex shedding time scale of 10^{-5} seconds. Figure 4.15 shows a surface plot of the mean mach number. A smooth and continuous subsonic acceleration is noticed upto the throat of the passage, following which Prandtl-Meyer expansion waves [1] accelerate the supersonic flow to Mach 1.1 upto the trailing edge of the vane. A weak shock close to the trailing edge (90 % C_{ax}) decelerates the flow to a Mach number of 0.95.

Validation with experimental results

(a) NGV Vane surface loading

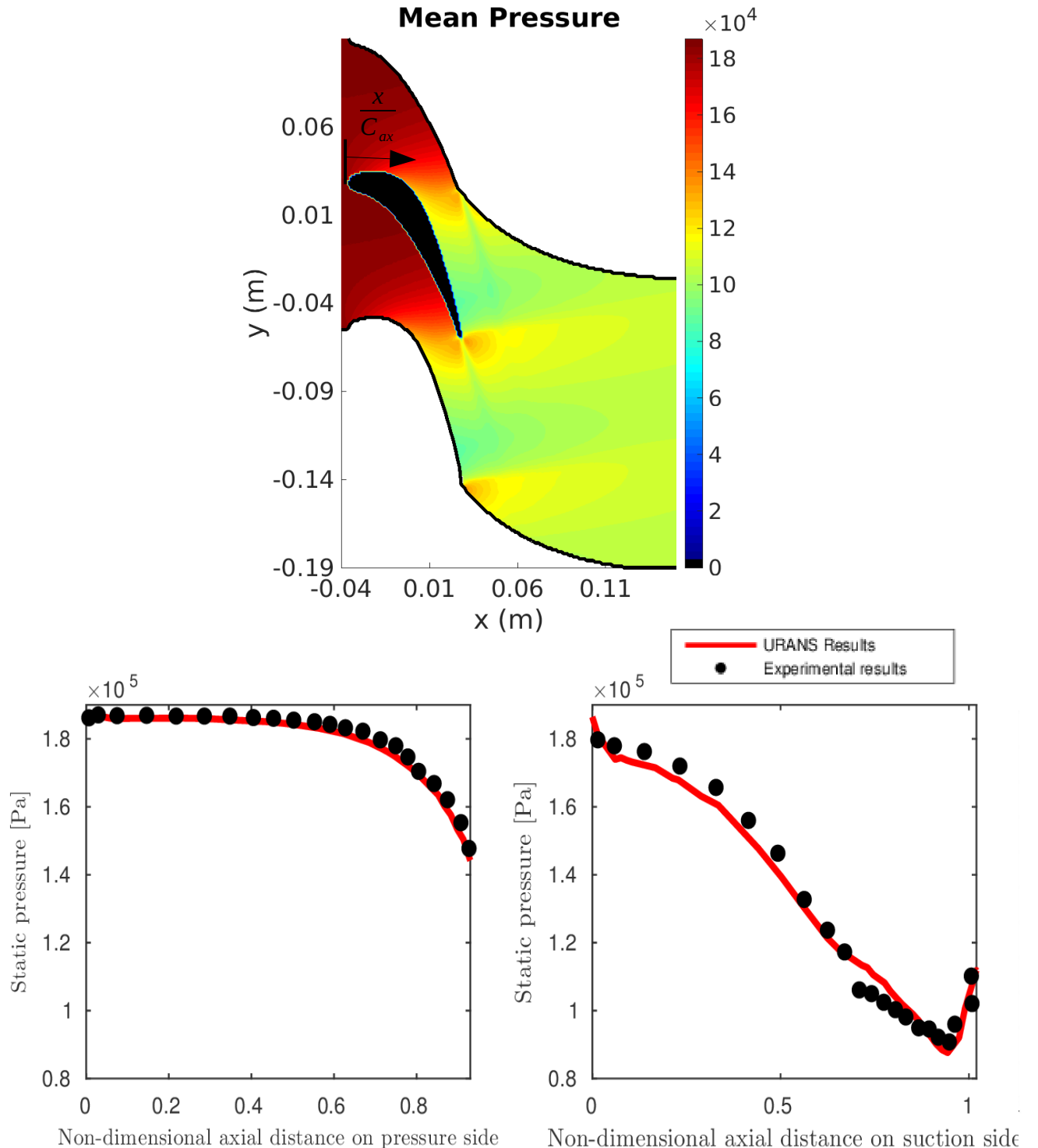
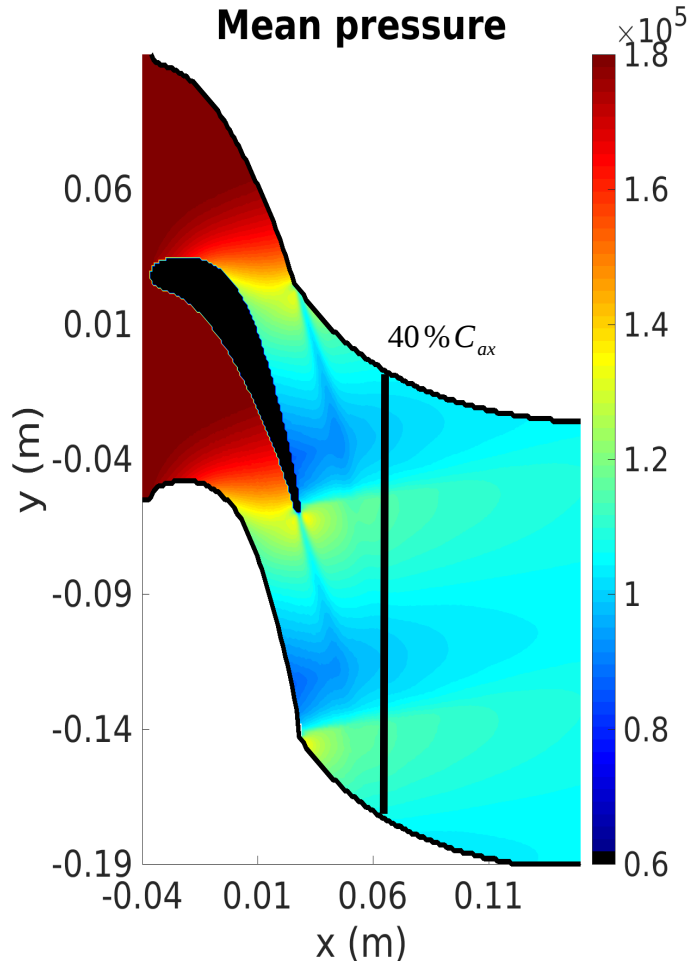


Figure 4.16. Static pressure plotted across the (a) pressure and (b) suction sides of the NGV

In Figure 4.16, the static pressure along the central vane surfaces is plotted against the normalized axial distance. Experimentally, the flow is observed to continuously accelerate upto an axial position of 70% C_{ax} , which is reported to be the location of the throat of the guide vane surface. The URANS simulations indicate the location of the throat at 68% C_{ax} , which is in good agreement with experimental results. Beyond the throat, both the simulation and

experiment predict a further decrease in Mach number, which can be attributed to Prandtl-Meyer expansion. At 93% C_{ax} , a normal shock is predicted experimentally, while the position predicted by the simulation is at 90% C_{ax} . On the pressure side, the pressure is seen to monotonically decrease along the surface of the vane, with the simulation results following the experimental results closely right upto the outlet of the passage. Overall, the simulation results follow the experimental results closely.

(b) Circumferential static pressure distribution at a distance of 40 % C_{ax} downstream to the hub of the cascade



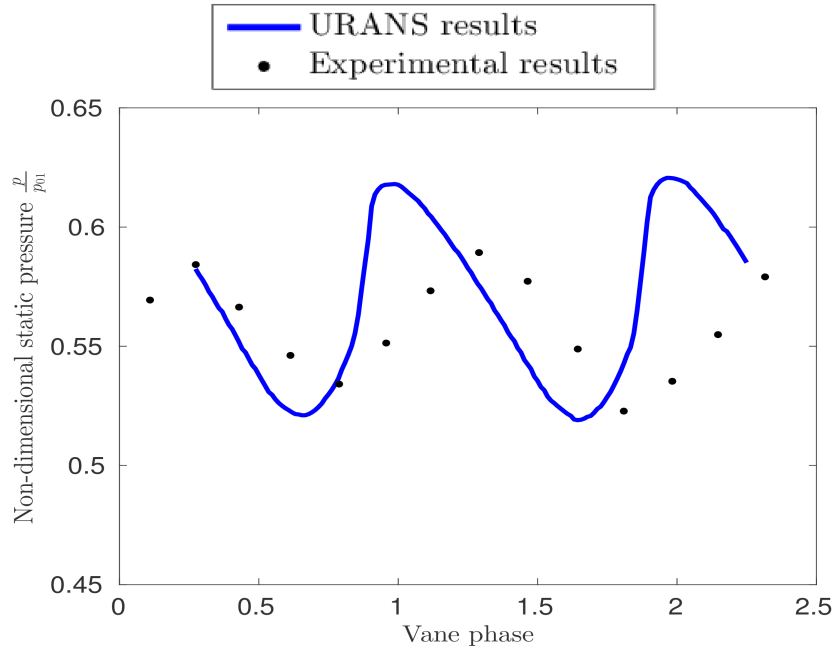
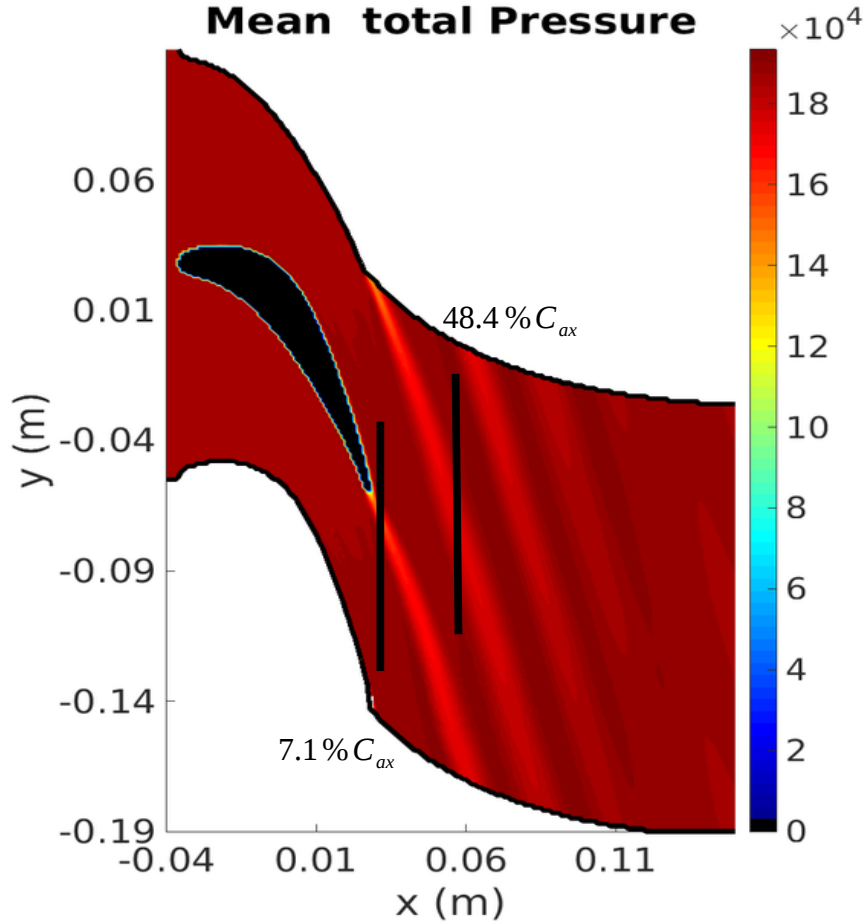


Figure 4.17. Non-dimensional static pressure plotted against the vane phase at 40% C_{ax}

The experimental results for the pitchwise pressure variation at the hub indicate agree well with the results predicted by the simulations. In general, periodicity is well respected. The simulation results are slightly skewed, perhaps because of the 2-D representation of the 3-D annular sector cascade.

(c) Non-dimensional total pressure at different axial planes



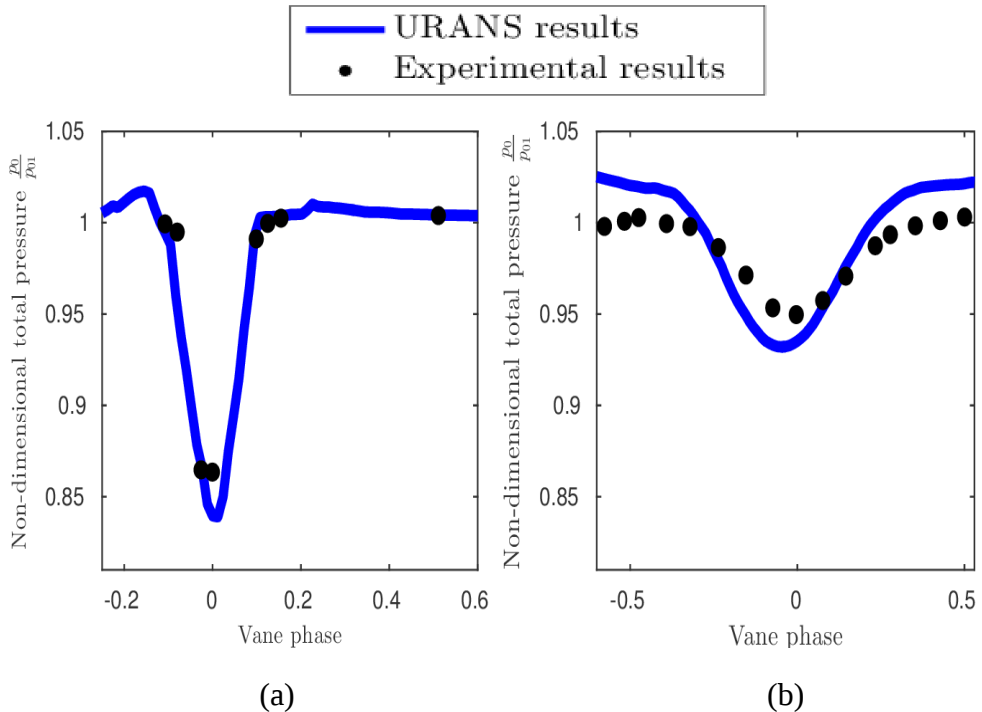


Figure 4.18. Non-dimensional stagnation pressure at 2 downstream axial planes (a) 7.2 % C_{ax} and (b) 48.4% C_{ax}

It was interesting to look at the total pressure losses predicted by the simulation at 2 downstream planes of 7.2 % C_{ax} and 48.4% C_{ax} , and compare the results with experiments. As indicated in the plots in Figure (4.18), the wake is increasing in its extent further downstream to the vane trailing edge. Further, due to extensive mixing at the wake shear layers, the total pressure losses are greatly reduced downstream to the trailing edge of the vane. In general, a good agreement with experimental results is observed.

(d) Vortex shedding frequency

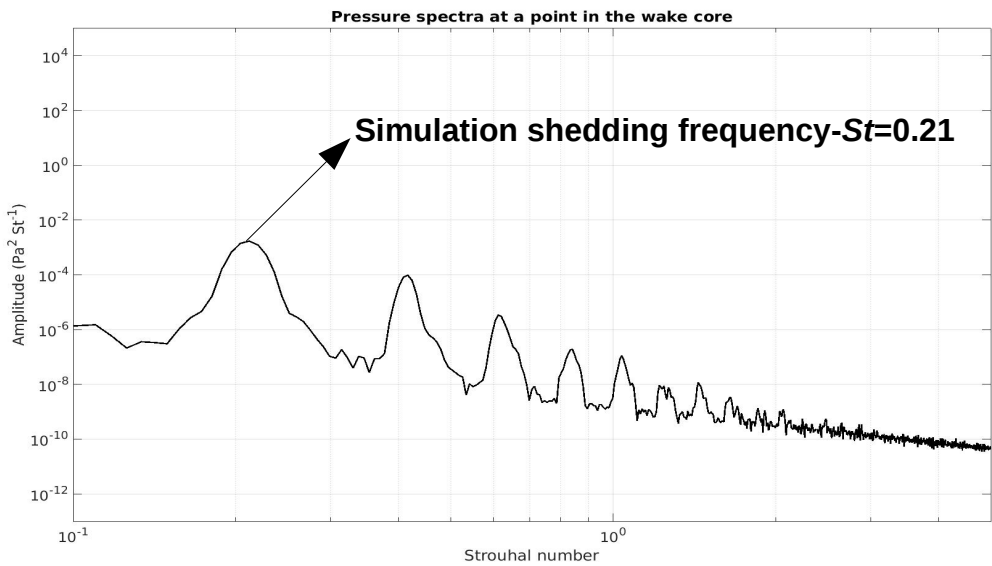


Figure 4.19. Power spectral density of pressure at a point in the core of a vane wake

In order to characterize the vortex shedding frequency, the pressure signal at a point in the core of the vane wake was recorded at every time step. The point was situated at a plane 23.2% C_{ax} downstream to the trailing edge of the vane. The power spectral density of the signal reveals a dominant frequency at $St=0.21$, wherein the length scale for the Strouhal number is based on 26 % maximum vane thickness [27]. The velocity scale for computing the Strouhal number was chosen based on the exit mach number of 0.95.

The experimentally predicted vortex shedding frequency was at $St=0.2$, thus revealing a good agreement between experimental and simulation results.

5 CONCLUSIONS AND RECOMMENDATIONS FOR FUTURE WORK

5.1. CONCLUSIONS

The *dbnsTurbFoam* solver was successfully attested against the 1-D Sod's shock tube. The predicted traveling wave speeds were in good agreement with analytical results. Moreover, low numerical viscosity was introduced in the flow solution and Gibb's oscillations were non-existent. Following this the transonic flow within the ONERA S8 channel was simulated. URANS simulations were able to predict the occurrence of the lambda shock structure and give first insights into the shock-boundary layer interaction dynamics. A thorough validation of the mean fields resulted in several problems, as discussed in Chapter 4. It is important to address these problems in the future and successfully validate the solver on the case. Finally, the solver was tested to simulate the flow within the passages of the High Pressure Turbine Nozzle Guide Vane (HPT-NGV). The mean fields obtained from the URANS simulations agreed well with experiments. In order to extend the solver to perform aero-acoustic computations, cutting edge Large eddy simulations (LES) of the flow within the cascade are to be performed. This lead to coupling the solver with the LES module to simulate the flow through the HPT-NGV cascade. Based on the preliminary LES results obtained, it is proposed to extend the validated module to perform aero-acoustics computations characterizing indirect combustion noise.

5.2. ONERA S8 CHANNEL

The author describes interesting work for the future that could be performed for the ONERA S8 channel test case.

(a) Obtaining the phase averaged fields

The time averaged results for the lambda shock resulted in smearing the shock structure considerably as described in Chapter 4. This was attributed to the large scale motions of the lambda shock structure. Therefore, a phase average of the various time-snapshots is instead recommended as given by Equation 5.1.

$$\left\{ \begin{array}{l} \bar{U}(x, t_{ref}) = \lim_{N \rightarrow \infty} \frac{1}{N} \sum_{i=1}^N U(x, t_{ref} + i \Delta t_0) \\ t_0 = \frac{1}{f_0} \end{array} \right. \quad (5.1)$$

Here, f_0 is the dominant frequency of oscillation of the normal shock and t_{ref} is the reference time from which the phase averaging is started. Reynolds and Hussain (1972) [32] have demonstrated that by averaging quasi-periodic flow fields at a particular phase, the random fluctuations in the flow field are decoupled and averaged. A phase averaging over 6 different phases of the normal shock motion is proposed for future work.

(b) Resolving the wall

Another aspect for future investigation is to perform simulations resolving the viscous sub-layer. Grid convergence of the mean fields has not been achieved, and moreover, the lambda shock was placed slightly upstream to the experimental position. The author thinks that a complete resolution of the boundary layer at the region of separation is required for placing the lambda shock at the right position.

(c) Perform steady state simulations to obtain the mean fields

As an alternative to performing transient simulations, steady state simulations based on the concept of Local time stepping (LTS) could be performed to obtain the time averaged mean

fields. In LTS, convergence to steady state is accelerated for an explicit time integration scheme via the selection of a time step varying across the domain.

(d) Shock wave Hysteresis

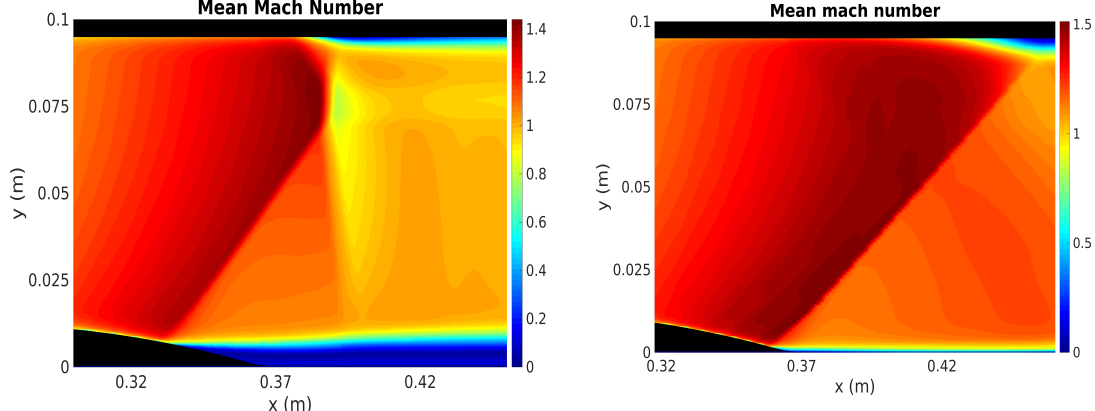


Figure 5.1 Two stable solutions for a particular outlet pressure (a) Lambda shock (b) Oblique shock

The phenomenon of Shock wave Hysteresis has been reported by Moroianu et al. (2005) [26], besides the global flow unsteadiness for a single flow configuration in the flow domain within the channel. The phenomenon of shock wave hysteresis refers to the existence of two stable shock configurations within the flow domain for a single outlet pressure. The author presents the results for the Mean fields at an imposed outlet pressure of 0.60 Bar. A lambda shock configuration was obtained after a million iterations. In Figure 5.1 (a), the mean field for the lambda shock is presented. Continuing the simulation, an oblique shock configuration was obtained, as shown in Figure 5.1 (b). The mechanism for the phenomenon of hysteresis has not been investigated, and is interesting for future work.

5.3. Compressible LES module in *foam-extend*

The simulation results presented in the master thesis correspond to relatively rapid 2-D URANS which are useful for performing parameter studies. In order to perform a detailed study of the flow field, 3-D compressible LES is more suitable. The LES module in *foam-extend* has a number of sub-grid scale models to choose from, some of which are listed below:

- **Smagorinsky model:** An algebraic equation is used to model the sub-grid scales. The assumption in the equation is that the sub-grid scale eddies dissipate all the energy received from the resolved scales instantaneously and entirely [11]. The model is reported to introduce large dissipation at regions with high shear. A fix for this is implemented by including the Van-driest damping function that reduces the sub-grid scale eddy viscosity with increasing wall normal distance.
- **One-equation eddy viscosity model:** The model was chosen to begin LES on the HPT-NGV geometry, as it achieves a reasonable compromise between accuracy and computational cost. A one equation transport equation for the sub-grid scale turbulent kinetic energy is used to compute the sub-grid scale eddy viscosity. Eugene (2007) reports an improved performance of the one equation transport equation over algebraic sub-grid scale models in flows where history effects need to be taken into account. Moreover, no global correction fixes are required to limit the sub-grid scale eddy viscosity.
- **Differential stress sub-grid scale model:** On abandoning the assumptions of isotropy inherent to eddy viscosity models, a transport equation for the sub-grid scale stress tensor can be utilized. A solution to this equation would require computing all 6 components of the stress tensor, increasing the computational time significantly.

5.4. LES results obtained for the HPT-NGV case

The LES module in *foam-extend* was coupled to the One-equation eddy viscosity model to perform simulations for the HPT-NGV case. For this purpose, the 2-D mesh constructed in ICEM-CFD was extruded in the transverse direction across 30 planes. The distance between each transverse plane was maintained below the taylor micro-scale. Periodic boundary conditions were applied at the extruded faces to model a channel of infinite width. A snapshot of the LES results showing a detailed view of the complex interaction processes in the flow field is presented in Figure 5.2. In Figure 5.2, the gray-scale represents the contours of the velocity divergence, indicating regions with compressibility effects, while the color-scale represents the superimposed contours of the vorticity. A first step for future work would include validation of the mean fields with experimental results, before studying some of the unsteady processes occurring in the flow field, such as the vortex shedding and the interaction processes between the normal shock and the trailing edge wakes.

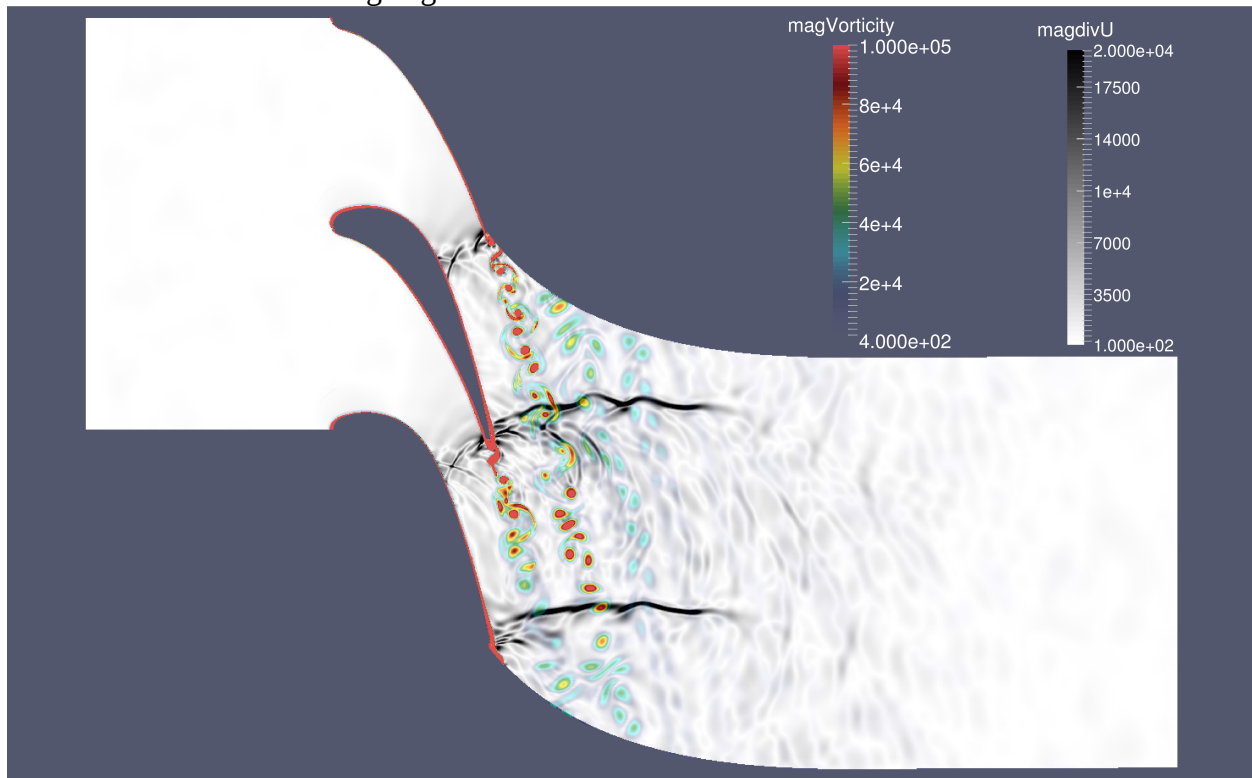


Figure 5.2 Snapshot of the flow field with the contours of vorticity in colour-scale superimposed and the contours of velocity divergence in grey-scale

5.5. Aeroacoustic simulations to characterize indirect combustion noise

Aero-acoustics studies focus on the identification of noise generation mechanisms and reduction of noise from fluid flow or fluid flow interacting with aerodynamic surfaces. The field arose in response to curbing aircraft noise in the mid-twentieth century with analytical methods introduced by Lighthill. The resolution of acoustic noise via analytical methods is possible for a few specialized cases, and therefore the field of Computational aero-acoustics (CAA) assumed importance in the late twentieth century. Computational aero-acoustics provides a framework for a reasonably good resolution of the acoustic noise over a wide range of problems. The field has a particularly high relevance for aircraft noise reduction.

The aircraft is a source of acoustic noise to humans in the aircraft cabin and in the vicinity of airports. The different sources of aircraft noise are frame noise, fan noise, engine combustion

noise, turbine noise and jet noise [34]. Based on the different stages of flight, such as take-off and taxi, cruise and landing, each of the noise sources attains a relative importance. Aircraft noise at take-off, taxi, landing and approach phases have the greatest physiological impact on humans. The introduction of high by-pass ratio turbofan engines coupled with advances in innovative fan blade design have resulted in significant reduction of the jet noise and fan noise, respectively. An increased attention has therefore been paid to combustion noise. With the introduction of lean pre-mixed combustion in modern gas turbine engines, a significant reduction in NOx emissions has been achieved [35]. On the other hand, lean combustion is also responsible for large heat release rate fluctuations produced at the turbulent flame. The unsteady heat release generates low frequency entropy perturbations/spots that advect with the mean flow velocity downstream to the combustion chamber. These entropy perturbations have an associated density fluctuation at the flame, that propagates through the rest of the engine as acoustic waves [10]. This is the direct noise generation mechanism. On the other hand, the advection of the entropy waves in a region of mean velocity gradients results in the generation of acoustic waves. This is the indirect noise generation mechanism. In their paper Marble and Candel (1977) [22] have shown via the linearised Euler equations how the entropy waves act as an acoustic source under the influence of a strong velocity gradient. Under choked flow conditions at high mach numbers ($M>0.8$), it has been reported that indirect combustion noise is an order of magnitude higher than direct combustion noise [20]. Instead of simulating the realistic turbulent flame dynamics, a first approximation would involve introducing a low frequency sinusoidal entropy packet at the inlet to study indirect combustion noise. Such simulations have been conducted by Papadogiannis et al. (2014) [29]. A complete characterization of entropy noise and its relative importance in the HPT-NGV cascade remains an important aspect of future work.

6 REFERENCES

- [1] ANDERSON J.D., *Modern compressible flow: with historical perspective*. Vol. 12. New York: McGraw-Hill, 2004.
- [2] ANDERSON J.D., *Computational fluid dynamics*. Vol. 206. New York: McGraw-Hill, 1995.
- [3] BAILLY C., *Turbulence*, Springer International publishing Switzerland, 2015.
- [4] BAKE, KINGS & FISCHER, *Experimental Investigation of the entropy noise mechanism in aero-engines*, Noise notes, Vol.8, No.4, pages 57--70, Multi Science Publishing, 2009.
- [5] BLAZEK J., *Computational Fluid Dynamics: Principles and Applications*, Butterworth-Heinemann, 2008.
- [6] BAYYUK S.A., *Computation of inviscid compressible flows about arbitrary geometries and moving boundaries*, ProQuest, 2008.
- [7] BEAUDOIN M. & JASAK H., *Development of a Generalized Grid Interface for turbo-machinery simulations with OpenFOAM*, Open source CFD International conference, Vol.2, 2008
- [8] DELERY J., *Analyse du décollement résultant d'une interaction choc/couche limite turbulente en transsonique*, La Recherche Aérospatiale 6, 1978
- [9] DELERY J., *Experimental Investigation of Turbulence properties in Transonic Shock/Boundary layer interactions*, Vol.21, No.2, pages 180--185, AIAA journal, 1983
- [10] DURAN I., POINSOT T., NICOUD F., LIVEBARDON T. & BOUTY E., *Combustion noise in modern aero-engines*, Vol.7, pages--1, AerospaceLab, 2014
- [11] DE VILLIERS E., *The potential of large eddy simulation for the modelling of wall bounded flows*, University of London, 2007
- [12] GREENSHIELDS C.J., *The OpenFOAM programmer's guide*, <http://foam.sourceforge.net/docs/Guides-a4/ProgrammersGuide.pdf>, 2011
- [13] HIRSCH C., *Numerical computation of internal &external flows*, Butterworth-Heinemann, 2007
- [14] ATASSI H.M., *Interaction of acoustic and vortical disturbances within an annular cascade in a swirling flow*, Unsteady Aerodynamics, Aeroacoustics and Aeroelasticity of Turbomachines, pages 247--259, Springer, 2006
- [15] HOLGER, BABINSKY & HARVEY J.K., *Shock wave boundary layer interactions*, Vol.32, Cambridge University press, 2014
- [16] HOWE M.S., *Indirect combustion noise*, Vol.659, pages 267--288, Journal of Fluid Mechanics, Cambridge University press, 2010
- [17] HUMBLE R.A., SCARANO F., & VAN OUDHEUSDEN, *Unsteady Flow Organization of a Shock Wave/Turbulent Boundary Layer Interactions*, IUTAM Symposium on Unsteady Separated Flows and their Control, pages 319--330, Springer, 2009
- [18] JASAK H., (1996), *Error Analysis and Estimation for the Finite Volume Method with Applications to Fluid Flows*, University of London Imperial College, 1996

- [19] JOHANSSON A.V. & WALLIN S., *An introduction to turbulence*, KTH lecture notes, 2014
- [20] LEYKO M., NICOUD F., MOREAU S. & POINSOT T. *Numerical and analytical investigation of the indirect noise in a nozzle*, Center for Turbulence Research, Proceedings of Stanford summer program, 2008
- [21] MALASEKARA & VERSTEEG.H., *An introduction to Computational Fluid Dynamics*, Pearson education, 2007
- [22] MARBLE & CANDEL, *Acoustic disturbance from gas non-uniformities convected through a nozzle*, Journal of Sound and Vibration, Vol.55, No.2, pages 225--243, Elsevier, 1977
- [23] MATHIEU J. & SCOTT J., *An Introduction to Turbulent Flow*, Cambridge University press, 2000
- [24] MEJIN G-J., *Physical modeling of cavitation using an enthalpy based model*, Delft University of technology, M.Sc. Thesis, 2015
- [25] MENTER F., FERREIRA J., CARREGAL E., THOMAS K., BRAD & GERMANY, AC, *The SST Turbulence Model with Improved Wall Treatment for Heat Transfer Predictions in Gas Turbines*, Proceedings of the international gas turbine congress, pages 2--7, 2003
- [26] MOROIANU D., CARAENI D. & FUCHS, L., *Large eddy simulation of a shock boundary layer interaction in a transonic internal flow*, 43rd AIAA Aerospace Sciences Meeting and Exhibit, pages 6533--6542, 2005
- [28] MUELLER T.J. *Aeroacoustic measurements*, Springer Science & Business Media, 2013
- [29] PAPADOGIANNIS D., WANG G., MOREAU S., NICOUD F., DUCHAINE F. & NICHOLS J.W., *Boundary Interaction in a Transonic Internal Flow Assessment of the indirect combustion noise generated in a transonic high-pressure turbine stage*, Center for Turbulence Research, Proceedings of Stanford summer program, 2014
- [30] PIROZZOLI S., *Analysis of unsteady effects in shock/boundary layer interactions*, Center for Turbulence Research, Proceedings of Stanford summer program, 2010
- [31] POPE S.B., *Turbulent Flows*, IOP Publishing, 2000
- [32] REYNOLDS & HUSAIN, *The mechanics of an organized wave in turbulent shear flow. Part 3. Theoretical models and comparisons with experiments*, Journal of Fluid Mechanics, Vol.54, No.02, pages 263--288, Cambridge University press, 1972
- [33] RUSCHE H., JASAK H. & SUNJO K. (2014), *Coupled Density-Based Solver for High-Speed Compressible Flows*,
[http://download2.polytechnic.edu.na/pub4/sourceforge/o/op/openfoam-extend/OpenFOAM_Workshops\[OFW9_2014_Zagreb/Presentations/Karlo_Sunjo_OFW09_P_0_123.pdf](http://download2.polytechnic.edu.na/pub4/sourceforge/o/op/openfoam-extend/OpenFOAM_Workshops[OFW9_2014_Zagreb/Presentations/Karlo_Sunjo_OFW09_P_0_123.pdf), 2014
- [34] SAHA R., *Aerodynamic investigations of Leading Edge Contouring and External Cooling on a Transonic Turbine Vane*, KTH Royal Institute of Technology, 2014
- [35] SCHILMALDER K.U, HOFFMANN A. , SELLE L., KOCH R., SCHULZ C. , BAUER H.J., POINSOT T. KREBS W. & PRADE, B., *Unsteady flame and flow field interaction of a premixed model gas turbine burner*, Proceedings of the combustion institute, Vol.31, No.2, pages 3197--3205, Elsevier, 2007

- [36] SEMLITSCH B., *Large Eddy Simulation of Turbulent Compressible Jets*, KTH Royal Institute of Technology, 2014
- [37] SOD G.A., *A survey of several finite difference methods for systems of nonlinear hyperbolic conservation laws*, Journal of computational physics, Vol.27, No.1, pages 1--31, Elsevier, 1978
- [38] TOLGA Y., FRIDH J., PANIAGUA G. & VOGT D., (2014), *Performance of a nozzle guide vane in subsonic and transonic regimes tested in an annular sector*, Proceedings of ASME Turbo Expo 2010: Power for Land, Sea and Air GT2010, pages 1457--1467, Americal Society of Mechanical Engineers, 2010
- [39] WALIN S., (2015), *Applied CFD Lecture notes*, KTH

APPENDIX A

Governing equation representation in *dbnsTurbFoam*

The governing equations in the solver are represented as given below:

$$\left(-\frac{1}{\beta} \right) * fvm::(\frac{\partial \bar{\rho}}{\partial t}) + fvc::(\frac{\partial}{\partial x_j}(\bar{\rho} \tilde{U}_j)) = 0 \quad (\text{A.1.1})$$

$$\left(-\frac{1}{\beta} \right) * fvm::(\frac{\partial \bar{\rho} \tilde{U}_i}{\partial t}) + fvc::(\frac{\partial}{\partial x_j}(\bar{\rho} \tilde{U}_i \tilde{U}_j)) + fvc::(\frac{-\partial}{\partial x_j}(\tau_{ij}^{eff})) = 0 \quad (\text{A.1.2})$$

$$\begin{aligned} \left(-\frac{1}{\beta} \right) fvm::(\frac{\partial(\bar{\rho} \tilde{E})}{\partial t}) + fvc::(\frac{\partial}{\partial x_j}(\bar{\rho} \tilde{U} \bar{E})) + fvc::(\frac{\partial}{\partial x_j}(-\tau_{ji}^{eff} \tilde{U}_i)) \\ - fvc::(\frac{\partial}{\partial x_i}(\alpha_{eff} \frac{\partial}{\partial x_i}(h))) = 0 \end{aligned} \quad (\text{A.1.3})$$

$$\tau_{eff} = \mu_{eff} \frac{\partial}{\partial x_j}(\tilde{U}_i) + \mu_{eff} \frac{\partial}{\partial x_i}(\tilde{U}_j) - \frac{2}{3} \mu_{eff} \left(\frac{\partial U_j}{\partial x_j} \right) \mathbf{I} \quad (\text{A.1.4})$$

In Equation (A.1.3) α_{eff} represents the local effective thermal conductivity, taking into account the contributions from the molecular transport term and the turbulent transport term. Also, β represents the set of Runge-Kutta integration coefficients that have been presented in Chapter 3.

The concepts of *fvc* and *fvm* classes have also been discussed in Chapter 3.

APPENDIX B

Instructions for installing foam-extend on the local work-stations

The instructions for installation on various Linux based systems are compiled in the link below:

<https://openfoamwiki.net/index.php/Installation/Linux/foam-extend-3.2>

Instructions for installing foam-extend on Beskow

These instructions have been compiled by Jing Gong, at PDC, and they are presented here for reference.

All instructions are assuming that *foam-extend-3.2* installed in

/cfs/klemming/nobackup/s/satcha/foam-extend-3.2

- **Add all the required modules to run *foam-extend* on Beskow**

```
module sw PrgEnv-cray PrgEnv-gnu
export CRAYPE_LINK_TYPE=dynamic
module add cmake/2.8.12.2
export CC=cc
export CXX=CC
```
- **Edit the bashrc file "foam-extend-3.2/etc/bashrc"**

```
foamInstall=/cfs/klemming/nobackup/s/satcha
: ${WM_MPLIB:=MPICH}; export WM_MPLIB
```

Edit the setting.sh file "foam-extend-3.2/etc/setting.sh"

```
WM_CC='cc'
WM_CXX='CC'
export MPI_HOME=/opt/cray/mpt/7.0.4/gni/mpich2-gnu/49
export MPI_ARCH_PATH=/opt/cray/mpt/7.0.4/gni/mpich2-gnu/49
export MPICH_ROOT=$MPI_ARCH_PATH
```
- **Edit the following file "ThirdParty/Allwmake.stage2" by uncommenting- # OpenMPI**
- **Edit the following file-ThirdParty/rpmBuild/SPECS/scotch-6.0.0.spec**

```
# ln -s Make.inc/Makefile.inc.i686_pc_linux2.shlib Makefile.inc
ln -s Make.inc/Makefile.inc.x86-64_pc_linux2.shlib Makefile.inc
```
- **Edit the following file-ThirdParty/rpmBuild/SPECS/parmetis-4.0.3.spec**

```
make config cc=cc CXX=CC
```
- **Run the AllMake utility of the ThirdParty packages**

```
salloc -N 1
  etc/bashrc
    cd ThirdParty
      aprun -b -n 1 ./AllMake
```
- **Run the Allwmake utility of *foam-extend-3.2***

```
./Allwmake.firstInstall
./Allwmake
```